Adaptive Insertion of Cohesive Elements for Simulation of Delamination in Laminated Composite Materials

by

Ofir Shor

B.Sc., Ben-Gurion University of the Negev, 2001
M.E, Technion, Israel Institute of Technology, 2006

A THESIS SUBMITTED IN PARTIAL FULFILLMENT OF
THE REQUIREMENTS FOR THE DEGREE OF

DOCTOR OF PHILOSOPHY

in

The Faculty of Graduate and Postdoctoral Studies

(Civil Engineering)

THE UNIVERSITY OF BRITISH COLUMBIA

(Vancouver)

September 2016

Abstract

Composite materials are increasingly being used in advanced structural applications. Debonding of adjacent laminate layers, also known as delamination, is considered to be one of the most dominant damage mechanisms affecting the behavior of composite laminates. Various numerical methods for simulating delamination in composite materials do exist, but they are generally limited to small-scale structures due to their complexity and high numerical cost.

In this thesis, a novel technique aimed to allow efficient simulation of delamination in large-scale laminated composite structures is presented. During the transient analysis, continuum elements within regions where delamination has the potential to initiate are adaptively split through their thickness into two shell elements sandwiching a cohesive element. By eliminating the a priori requirement to implant cohesive elements at all possible spatial locations, the computational efforts are reduced, thus lending the method suitable for treatment of practical size structures. The methodology, called the local cohesive zone method (LCZ), is verified here through its application to Mode-I, Mode-II and Mixed-Mode loading conditions, and is validated using a dynamic tube-crushing loading case and plate impact events. Good agreement between the numerical results and the available experimental data is obtained. The results obtained using the LCZ method are compared favourably with the numerical results obtained using the conventional cohesive zone method (CZM).

The numerical performance of the method and its efficiency is investigated. The efficiency of the method was found to be superior compared to that of the conventional CZM, and was found to increase with increasing model size. The LCZ method is shown to have a lower effect on reducing the structural stiffness of the structure, compared to the conventional CZM.

The results obtained from the application of the LCZ method to the various cases tested are encouraging, and prove that the local and adaptive insertion of cohesive zones into a finite element mesh can effectively capture the delamination crack propagation in laminated composite structures. It is expected that further improvements in speed and accuracy will be attained

once the algorithm is embedded within commercial finite element solvers as a built-in feature.

Preface

This thesis entitled "Adaptive Insertion of Cohesive Elements for Simulation of Delamination in Laminated Composite Materials" presents the research performed by Ofir Shor. The research was supervised by Dr. Reza Vaziri at the University of British Columbia.

A version of the contents of Chapter 2, Chapter 3, and Chapter 4, was published in Shor and Vaziri [118], "Adaptive insertion of cohesive elements for simulation of delamination in laminated composite materials", Engineering Fracture Mechanics. These sections, include the original verification work of the LCZ algorithm developed during the research.

Figure 5.6.a, Figure 5.7.b, Figure 5.8.b, and Figure 5.9.b are courtesy of Dr. Stephen Hallett from the University of Bristol. The results from tensile experiments performed by Dr. Hallett are shown in these figures, in order to validate the failure patterns in a double-notched test coupon, which was also predicted by the algorithm developed by the thesis' author.

Table of Contents

List of Tables

List of Figures

List of Computer Programs

List of Symbols

A element-set used by the LCZ algorithm during the element splitting process

a length of initial crack

A_{TSLC} area under the normalized traction-separation law, used as an input to the cohesive material model.

C^0 structural stiffness of the undamaged material

C^d structural stiffness of the damaged material

d damage parameter

E_{11} Young's modulus, axial direction

E_{22} Young's modulus, transverse direction

E_{33} Young's modulus, normal direction

E_{xx} longitudinal elastic modulus

E_{yy} transverse elastic modulus

E_{zz} out-of-plane elastic modulus

G_{12} shear modulus, 12 direction

G_{23} shear modulus, 23 direction

G_{31} shear modulus, 31 direction

G_{Ic} critical strain-energy release rate, mode I

G_{IIc} critical strain-energy release rate, mode II

h thickness of beam

i first element to reach the critical value of the element-splitting criteria

K_I stress intensity factor for mode-I crack opening

K_II stress intensity factor for mode-II crack opening

l length of beam

L length of beam

P reaction force monitored during the transient analysis

Q element satisfying the radial search criterion,

r radial distance from a crack tip

R geometrical radius used by the radial-search algorithm

R_1 geometrical radius used by the radial-search algorithm

R_2 geometrical radius used by the radial-search algorithm

S parameter used for the element splitting criterion

S_c parameter used for the critical value of the element-splitting criterion

t thickness of beam

$\bar{t}$ normalized traction-stress

XMU failure parameter used in the cohesive material law

α user-defined interaction term for cohesive damage growth

β mode-mixity of the cohesive load

δ_I crack-opening in the normal direction

δ_{II} crack-opening in the shear direction

Δ applied displacement

ε_f intralaminar damage saturation strain

$\left[\varepsilon_y^i\right]_t$ initiation strain for damage under tension in the transverse direction

$\left[\varepsilon_y^i\right]_c$ initiation strain for damage under compression in the transverse direction

$\left[\varepsilon_y^s\right]_t$ saturation strain for damage under tension in the transverse direction

$\left[\varepsilon_y^s\right]_c$ saturation strain for damage under compression in the transverse direction

$\left[\varepsilon_x^i\right]_t$ initiation strain for damage under tension in the axial direction

$\left[\varepsilon_x^i\right]_c$ initiation strain for damage under compression in the axial direction

$\left[\varepsilon_x^s\right]_t$ saturation strain for damage under tension in the axial direction

$\left[\varepsilon_x^s\right]_c$ saturation strain for damage under compression in the axial direction

ϕ angle in a radial coordinate system, relative to the crack interface

λ normalized crack opening

ν_{12} major Poisson's ratio, (in-plane)

ν_{13} major Poisson's ratio, (out-of-plane)

ν_{23} Poisson's ratio, (transverse plane)

σ_{13} out-of-plane shear stress in the 13 local material's coordinate system direction

σ_{23} out-of-plane shear stress in the 23 local material's coordinate system direction

σ_{33} out-of-plane normal stress in the local material's coordinate system direction

σ_{max} maximum normal stress in the cohesive interface, before softening begins

σ_{zz} stress in the global zz direction

σ_{zz}^c critical value of the stress in the global zz direction, at which element splitting takes place, in the numerical DCB verification case.

τ_{xz} shear stress in the global zx plane

τ_{max} maximum shear stress in the cohesive interface, before softening begins

Acknowledgements

Dedication

To my parents, Etta and Menachem, who always gave me the best education they could.

Chapter 1

Introduction

The use of composite materials in advanced engineering applications is growing rapidly due to their excellent specific strength, durability, fatigue and corrosion resistance. While originally used in limited number of military and aerospace applications due to their high manufacturing cost and the lack of scientific knowledge related to their processing and mechanical behavior, the need to develop lighter and yet stronger structures, together with the accumulated knowledge related to their processing and mechanical behavior, allowed composites to become widely used in numerous industrial applications requiring peak performance and superior reliability.

Composite materials can now be found in a wide range of commercial products, ranging from sports equipment such as bikes and skis, to load bearing structures in the automotive, aerospace and ship-building industries. The use of composites as the main structural material in the fuselage of the Boeing 787 commercial jet airliner, demonstrates the huge leap in the development of composites during the last decades.

Despite their benefits, composites pose great engineering challenges, both from the manufacturing standpoint as well as their mechanical behavior. As their physical architecture consists of thin layers (plies) of relatively high-strength anisotropic material stacked to the required thickness using relatively weak bonding materials (matrix), their structural performance often derives not only from the behavior of a single ply, but also from the interaction and mechanical behavior of the ply-bonding interface. Failure of the interface between the composite plies, often known as delamination, can lead to premature strength reduction and reduced load carrying capacity of the structure, hence the need to develop reliable methods to predict its initiation and growth within these materials.

Despite the vast amount of research, a unified damage theory that can capture all of the complex damage mechanisms in composites and describe their behavior up to final failure is still beyond reach. Yet, various damage theories are constantly being developed, and the rapid growth in computational power allows more sophisticated theories and computational methods to be applied, increasing the predictive capability of their behavior.

The UBC Composites Group, part of the Composite Research Network, a consortium founded and supported by the government of Canada, serves as a fertile growing ground for composites research. The Group's vision has always been development of physically based and numerically robust numerical tools, that would give engineers practical tools to develop their composite products with greater reliability, higher performance, and lower cost.

Recognizing the importance of modelling delamination in a discrete manner, yet aiming toward the development of a numerically efficient modelling methodology, the author's contribution of the present work is in the development of a new method which allows simulating the initiation and growth of delamination damage in an adaptive manner. Using this method, the structure can be modelled with only one layer of elements through the thickness. During the transient analysis, the continuum elements are locally and adaptively split through their thickness, and cohesive elements are introduced in regions where delamination has the potential to initiate and grow. Delamination can thus propagate in the structure as the simulation progresses. Reducing the number of cohesive elements present in a model contributes to the reduction of the computational cost, as well as alleviating the unwanted artificial stiffness reduction caused when cohesive-elements are embedded in large regions of the model. The method can be combined with the other numerical models developed within the UBC Composites Group for intralaminar (in-plane) damage behavior, and thus serves as a continuation of the work.

The details of the method are presented in Chapter 3, followed by verification of the method for Mode-I, Mode-II, and Mixed-Mode loading conditions (Chapter 4). In Chapter 5, the method is applied to various engineering applications including dynamic loading of composite structures. The results obtained using the current methodology are compared to experimental results, as well as to results obtained using other numerical techniques. The numerical advantages of the method are described in Chapter 6. Chapter 7 presents the conclusions drawn from the research and suggest topics for future work. Appendix A presents a flowchart of the LCZ algorithm developed during the research. Detailed instructions for setting and executing the LCZ algorithm is outlined in Appendix B. A general description of composite tube crushing process is provided in Appendix B. Appendix D provides the important keywords used during the simulations described within this thesis. A brief description of the CODAM2 material model, which is used in Chapter 5 for simulating a dynamic tube crushing event, is given in Appendix E. Description of the process used in order to cali-

brate the CODAM2 material parameters for the tube crushing simulations is presented in Appendix F.

Chapter 2

Numerical Simulation of Delamination in Composites

Composite materials are increasingly being used in advanced structural applications. Failure of these materials involves evolution of various damage mechanisms, such as fibre breakage and matrix cracks (Zobeiry, Vaziri, and Poursartip [137], Green et al. [44]), where the debonding of adjacent laminate layers, also known as delamination, is considered to be one of the most dominant damage mechanisms affecting the behavior of composite laminates. Delamination will usually lead to a reduction in structural stiffness and load carrying capability, and can also lead to instability and premature structural failure under compressive loading (Bolotin [11]). This raises the necessity to predict its initiation and propagation.

Early methods aimed at simulating delamination in composites were based on stress-based criteria, where the inter-laminar and out-of-plane stresses ($\sigma_{13}, \sigma_{23}, \sigma_{33}$, with x_1 and x_2 as in-plane coordinates and x_3 being the out-of-plane coordinate) were used to predict the initiation and growth of delamination damage in the material ([61]). These models were proven to be effective in capturing the initiation of delamination, but could not capture the scale-effects as in a fracture-based model (Davies and Zhang [21]). Since the delamination damage mode is discrete in nature, it is widely accepted in the scientific community that fracture mechanics principles should be implemented in order to accurately predict delamination initiation and growth.

The Virtual Crack Closure Technique (VCCT), originally developed by Rybicki et al. [113],[112], is based on fracture-mechanics principles. Using this method, the strain energy release rate G is calculated numerically, and is compared to some critical value G_c in order to determine whether or not the delamination crack propagates in a given timestep. VCCT was proven to be capable of predicting the evolution of delamination damage under various loading conditions (Rybicki et al. [113], Raju et al. [108], Zheng and Sun [136]). Complex delamination patterns were also predicted by the VCCT method, where the strain-energy release rate was used to predict delami-

nation induced damage during a low velocity impact event ([72], [73]). An overview of the VCCT method and its numerical implementation into finite element codes can be found in [69], [70]. An evaluation of the capabilities of two commercial finite element solvers - ABAQUS and MARC, to predict delamination growth and the strain-energy release rate in ENF and DCB loading cases, appears in Ori [1]. A major drawback of the VCCT method is that it requires the presence of an initial crack in the finite element mesh prior to the analysis, which makes the method useful for cases where the exact location of the delamination crack is explicitly known. For cases involving large structures where delamination crack location is unknown, the method becomes less favourable. In addition, since VCCT is based on linear elastic fracture mechanics (LEFM), it is limited to cases where the size of the fracture process zone is negligibly small compared to the other structural dimensions. This assumption is not valid for many quasi-brittle materials [10]. In such cases, the fracture process zone, as well as the embedded cohesive tractions have to be modelled explicitly. Cohesive zone models have been developed over the past decades to address the above issues.

2.1 The Cohesive-Zone Method

The cohesive zone method (CZM) is based on a concept originally proposed by Dugdale [27] and Barenblatt [8], which stated that unlike perfectly elastic material behavior which predicts infinite stress values at the crack tip, there is a region of material ahead of the crack tip within which the material behavior is not linear elastic, thus yielding a state of stress with finite values. This region of damaged material is often referred to as the Cohesive Damage Zone (CDZ), or the Cohesive Zone (CZ), (Figure 2.1.a). This idea was used by Dugdale [27] to determine plastic zone sizes in steel panels containing slits. In fiber reinforced plastic composite materials (FRPs) this "damage zone" consists of matrix cracking, fibre breakage, interface separation and fibre pullout. In a cohesive crack approach, a relationship between traction and displacement is defined along a potential crack surface, ahead of an actual crack or notch tip.

When implementing the cohesive-zone method in a finite element solver, the cohesive zone is embedded into the model using a cohesive interface (Figure 2.1.b), where the need to calculate the non-physical singular stress field at the crack tip is eliminated by using a force-displacement relation between the nodes in the finite element mesh (traction-separation law) [28]. This law is the basis for computing the delamination crack initiation, prop-
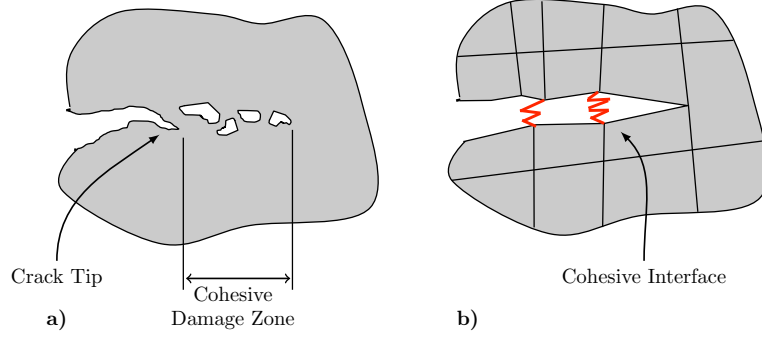
Figure 2.1: A schematic diagram demonstrating a typical cohesive zone in a continuum material. **a)** A volume of damaged material which extends beyond the crack tip, is referred to as the "Cohesive Damage Zone". **b)** In a finite element model, the cohesive zone is modelled using a cohesive interface realized using a cohesive law, via discrete (Hallett and Wisnom [46]) or solid cohesive elements (Hu et al. [56],[122],), a cohesive contact formulation (Borg et al. [12], Borg et al. [13]), or cohesive properties directly embedded into the element formulations [60]. As the crack opens, traction forces are applied across the interface, defined using a traction vs. separation law.

agation, and opening. A typical bilinear traction-separation law is shown in Figure 2.2. The stress at the interface, σ, is plotted against the interface opening, λ. The interface is linear elastic up to a maximum stress, σ_{max}, at a displacement λ_0. As the interface is further loaded, the interface stress linearly decreases until a critical displacement λ_0 is reached, at which the interface stress reaches 0 and the crack interface is traction-free.

CZMs incorporates fracture mechanics principles, as the area under the traction-separation curve is equal to the critical strain-energy release rate of the material G_c (Figure 2.2). By defining multiple traction-separation laws, the cohesive behavior of the material can be described under mode-I and mode-II loading directions. In this case, a separate traction-separation law is defined for each mode of loading, together with a mode-mixity relation, between the two modes (Mi et al. [91] Alfano and Crisfield [5] ,[52]).

The relation between the state of stress in a crack under mode-I loading condition and the crack opening displacement is shown in Figure 2.3. In this figure, a schematic side view of a crack under mode-I loading condition is presented, together with a traction-separation law, representing the state
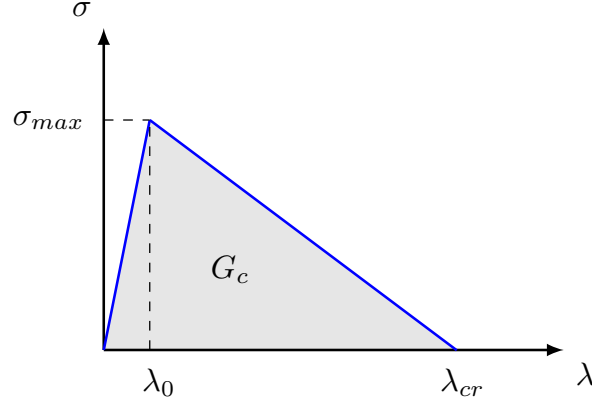
Figure 2.2: A typical bilinear traction-separation law used in a cohesive interface model. The stress at the interface, σ, is plotted against the interface opening, λ.

of traction stress along the crack interface. The loaded geometry is divided into three distinct regions or zones - A region of homogeneous material, the cohesive zone, and a region consisting of the crack's free surfaces. The homogeneous material consists of material at an unloaded state, or material at a loaded state having a traction level lower than σ_{max}. The geometrical location where the traction level reaches σ_{max} and the cohesive zone begins, is termed the mathematical crack front. At this location, the traction stresses decrease with an increased crack opening. The cohesive zone spans along the positive x direction, from the mathematical crack front, to the point where the traction stresses reach a value of 0, often termed the physical crack front. The physical crack front is the location where a traction free region begins, consisting of the crack's free surfaces.

For mode-II loading condition, the schematic stress distribution is similar to the one shown in Figure 2.3, with the maximum traction stress equal to τ_{max}, and the critical fracture energy equal to G_{IIc}.
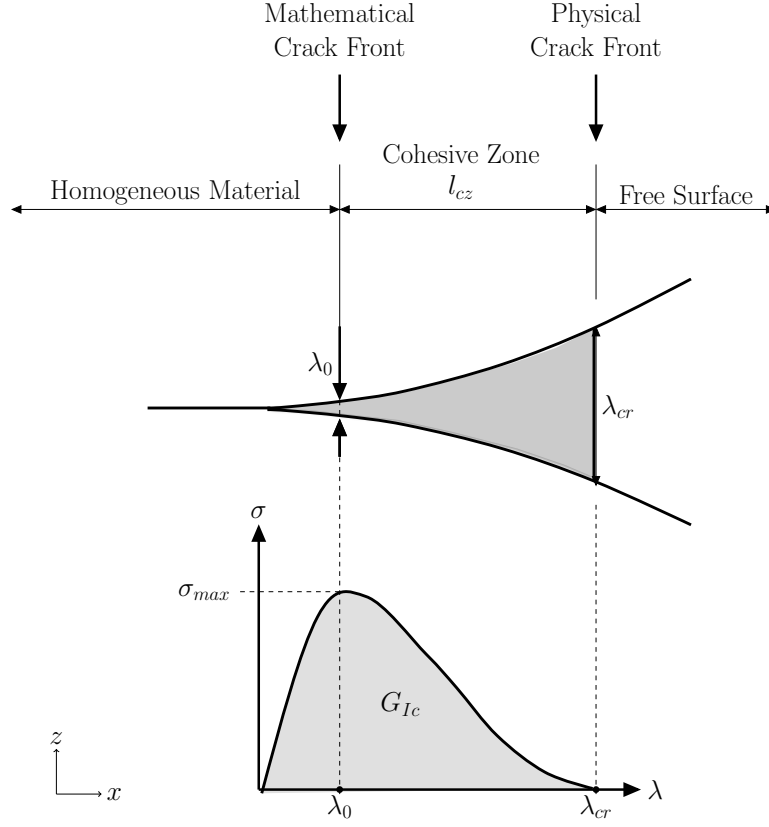
Figure 2.3: A schematic side view of a crack under mode-I loading condition. A traction-separation law is plotted below the crack, representing the state of traction stress within the material. Three distinct regions span across the crack interface - A region of homogeneous material, the cohesive zone, and the crack interface where free surfaces have been created. The cohesive zone spans from the point of maximum stress (σ_{max}) to the location where the free-surfaces of the crack begin and the stress level has reached a value of 0. The geometrical location where the traction level reaches σ_{max} and the cohesive zone begins, is termed the mathematical crack front. The physical crack front is the location where a traction free region begins (λ_{cr}, $\sigma = 0$), consisting of the crack's free surfaces.

2.2   Estimating the Cohesive Zone Length

Diferent models have been proposed in the literature to estimate the length of the cohesive zone. Irwin [59] presented a simplified model for the determination of the plastic zone ahead of a crack tip, for an elastic, perfectly plastic material. Based on his approach, crack growth can be predicted using linear-elastic fracture-mechanics principles. Figure 2.4 presents an infinite geometry, having an initial crack of length $2a$ uniformly loaded with an applied stress σ.
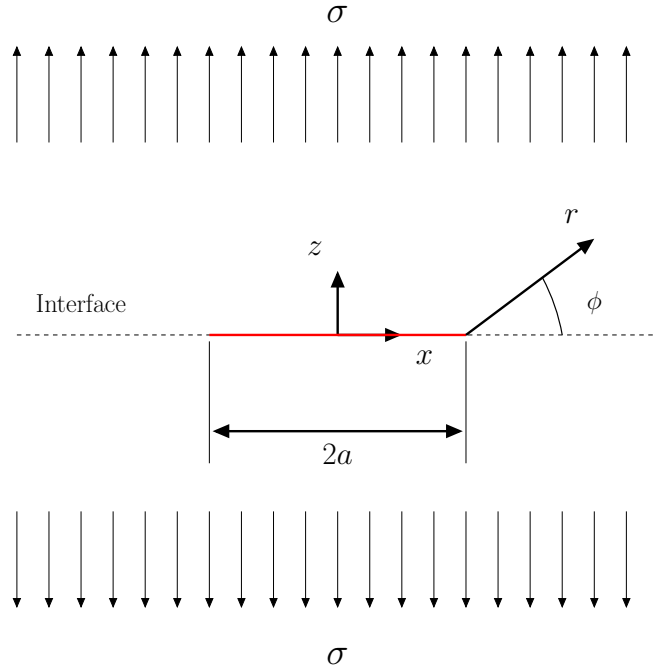
Figure 2.4: Uniformly mode I loaded infinite geometry with an linear crack of an initial length $2a$ in the interface.

The stress components around the crack tip are given by [128]:

$$\sigma_{xx} = \frac{K_I}{\sqrt{2\pi r}} \left[cos(\frac{1}{2}\phi) \left(1 - sin(\frac{1}{2}\phi) sin(\frac{3}{2}\phi) \right) \right] \tag{2.1}$$

9

$$\sigma_{zz} = \frac{K_I}{\sqrt{2\pi r}} \left[cos(\frac{1}{2}\phi) \left(1 + sin(\frac{1}{2}\phi)sin(\frac{3}{2}\phi) \right) \right] \tag{2.2}$$

$$\sigma_{xz} = \frac{K_I}{\sqrt{2\pi r}} \left[cos(\frac{1}{2}\phi)sin(\frac{1}{2}\phi)cos(\frac{3}{2}\phi) \right] \tag{2.3}$$

$$\sigma_{yy} = \nu \left(\sigma_{xx} + \sigma_{zz} \right) \tag{2.4}$$

where K_I is the stress intensity factor for mode-I crack propagation, r is the radial distance from the crack tip, and ϕ is the angle relative to the crack interface (x axis).

It can be inferred from Equation 2.2, that in the vicinity of the crack tip ($r = 0$), σ_{zz} reaches a value of ∞ along the crack propagation direction ($\phi = 0$), (Figure 2.5(a). Irwin [59] stated that since yielding or further crack propagation will occur prior for the stress levels reaching infinite values, the stress values are limited by a maximum limiting value (σ_{max}, Figure 2.5(b)). Thus, under this assumption, using Equation 2.2 to evaluate σ_{zz} at $\phi = 0$ yields:

$$\sigma_{zz} = \sigma_{max} = \frac{K_I}{\sqrt{2\pi l_a}} \tag{2.5}$$

where l_a (Figure 2.5(a)) is the length of the geometrical region along the crack propagation direction in which the relation $\sigma_{zz} = \sigma_{max}$ is satisfied.

Equation 2.5 can be re-written to evaluate l_a:

$$l_a = \frac{K_I^2}{2\pi\sigma_{max}^2} \tag{2.6}$$

Using l_a as suggested by Equation 2.6 will not satisfy the global equilibrium. Irwin suggested a correction - defining a new plastic zone size l_{pz}, which will, for a given value of σ_{max}, satisfy the following equation:

$$\sigma_{max}l_{pz} = \frac{K_I}{\sqrt{2\pi}} \int_0^{l_a} r^{-\frac{1}{2}} dr = \frac{2K_I}{\sqrt{2\pi}} \sqrt{l_a} \tag{2.7}$$

The geometrical interpretation of Equation 2.7 is schematically presented in Figure 2.5(c) and Figure 2.5(d), where l_{pz} is obtained by equating the hatched area in Figure 2.5(d) to the hatched area in Figure 2.5(c).

Combining Equation 2.7 and Equation 2.6 yields:

$$l_{pz} = \frac{K_I^2}{\pi\sigma_{max}^2} = 2l_a \tag{2.8}$$

Irwin derived a relation between the stress intensity factor K and the energy release rate G as:

$$K^2 = GE'$$

(2.9)

where in plane stress $E' = E$, and in plane strain $E' = E/(1 - \nu^2)$.

Assuming a mode-I loading condition, l_{pz} can be obtained by rewriting Equation 2.8 as:

$$l_{pz} = \frac{E' G_{Ic}}{\pi \sigma_{max}^2}$$

(2.10)

In case of mode-II loading condition, the stress components around the crack tip are given by [128]:

$$\sigma_{xx} = \frac{K_{II}}{\sqrt{2\pi r}} \left[-sin(\frac{1}{2}\phi) \left(2 + cos(\frac{1}{2}\phi)cos(\frac{3}{2}\phi) \right) \right]$$

(2.11)

$$\sigma_{zz} = \frac{K_{II}}{\sqrt{2\pi r}} \left[sin(\frac{1}{2}\phi)cos(\frac{1}{2}\phi)cos(\frac{3}{2}\phi) \right]$$

(2.12)

$$\sigma_{xz} = \frac{K_{II}}{\sqrt{2\pi r}} \left[cos(\frac{1}{2}\phi) \left(1 - sin(\frac{1}{2}\phi)sin(\frac{3}{2}\phi) \right) \right]$$

(2.13)

$$\sigma_{yy} = \nu \left(\sigma_{xx} + \sigma_{zz} \right)$$

(2.14)

Where K_{II} is the stress intensity factor for mode-II crack propagation.

Evaluating Equation 2.13 using $\phi = 0$ and $r = l_a$, yields:

$$\sigma_{xz} = \frac{K_I I}{\sqrt{2\pi l_a}}$$

(2.15)

Similar to the assumptions made in Irwin's corrections for mode-I crack propagation, Equation 2.7 can be used to obtain the plastic zone size under mode-II loading conditions:

$$l_{pz} = \frac{E' G_{IIc}}{\pi \tau_{max}^2}$$

(2.16)

where G_{IIc} is the critical strain energy release rate under mode-II loading, and τ_{max} is the maximum shear stress within the plastic zone.

Equation 2.8 can be rewritten using a more generalized format:

$$l_{pz} = M \frac{E' G_{Ic}}{\tau_{max}^2} \tag{2.17}$$

where M is a scaling factor, in which according to Irwin is equal to $1/\pi$. Other models predict different values for M, and are listed in Table 2.1. Dugdale [27] estimated the size of the plastic zone ahead of a crack tip by treating the plastic region as a narrow strip that is loaded by the yield traction. Hui [57] estimated the length of the cohesive zone for soft elastic materials, while Rice [109] and Falk et al. [30] estimated the length of the cohesive zone as a function of the crack growth velocity. Barenblatt [9] used assumptions similar to Dugdale [27] for ideally brittle materials.

Table 2.1: Estimated cohesive zone length (l_{pz}) and equivalent value for M in Equation 2.17

Source	l_{pz}	M
Hui [57]	$\frac{2}{3\pi} E \frac{G_{Ic}}{\sigma_{max}^2}$	0.21
Irwin [59]	$\frac{1}{\pi} E \frac{G_{Ic}}{\sigma_{max}^2}$	0.31
Dugdale [27], Barenblatt [9]	$\frac{\pi}{8} E \frac{G_{Ic}}{\sigma_{max}^2}$	0.4
Rice [109], Falk et al. [30]	$\frac{9\pi}{32} E \frac{G_{Ic}}{\sigma_{max}^2}$	0.88
Hillerborg et al. [54]	$E \frac{G_{Ic}}{\sigma_{max}^2}$	1

In order to obtain a reliable numerical solution when using the CZM to predict crack propagation, a minimum number of finite-elements should lie within the cohesive zone along the crack propagation direction [126]. Moes and Belytschko [92] suggested using more than 10 elements along the cohesive zone, while Falk et al. [30] used 2-5 elements in their work.

Turon et al. [126] and Alfano and Crisfield [5] showed that by reducing the maximum interfacial strength (σ_{max} in case of mode-I crack propagation, or τ_{max} in case of mode-II crack propagation), the cohesive zone length is increased, resulting in more elements spanning across the cohesive zone. This allows coarser meshes to be used in the analysis, still yielding reliable results. Alfano and Crisfield [5] showed that since artificially scaling the maximum traction stresses will also alter the stress distribution within the

structure, there is a limitation to the allowable artificial cohesive zone length that will still be acceptable before the solution will no longer reflect the correct mechanical behavior of the structure. This effect is demonstrated in Section 4.1.1, where scaling of the maximum cohesive strength is performed in order to investigate its effect on the solution of a mode-I verification problem.

Describing the complex material behavior using traction-separation laws, allows cohesive zone models to deal with the nonlinear zone ahead of the crack tip without necessitating the use of a refined mesh around the crack-tip region, and without introducing delamination cracks into the model prior to the analysis. CZM was successfully used by Camacho and Ortiz [14] to predict crack propagation during a steel/rock impact. The method was proven to be capable of predicting delamination growth in composite materials under static (Liu et al. [77],Yang and Cox [134]), as well as dynamic loading and impact conditions (Feng and Aymerich [33], Sokolinsky et al. [120], Olsson et al. [97], Gonzalez et al. [42]). Camanho [15] developed a zero-thickness volumetric cohesive element able to capture delamination onset and growth under mixed-mode loading condition. Forghani and Vaziri [36] and Menna et al. [90] used a cohesive contact interface to simulate delamination propagation in plates subjected to transverse impacts. Abisset et al. [3] used solid cohesive elements constrained using a contact algorithm tied to the continuum elements in the model in order to simulate plate indentation experiments. Cohesive elements were used to model both interlaminar as well as intralaminar damage within the material. By using a tied contact algorithm to constrain the cohesive elements nodes to the continuum elements, the need to have adjoining nodes between these different topologies is removed, thus allowing high flexibility from the modelling standpoint. Abisset et al. [3] were able to correctly depict the damage evolution within the specimens, for different material lay-ups.

Some models aim to describe the rate-dependency of the cohesive interface. Musto and Alfano [93] and Makhecha et al. [80] implemented cohesive elements formulations with strain-rate dependency, for mode-I DCB loading scenario. Anvari et al. [6] used rate-sensitive and triaxiality-dependent cohesive elements, to simulate crack growth under quasi-static and dynamic loading conditions.

Since the use of CZM in its standard form requires introduction of large number of cohesive elements in all possible locations where delamination is likely to grow, using this method to predict delamination crack growth in large structures is not practical from the numerical standpoint. Furthermore, using cohesive elements in wide regions of the model will artificially

render the structure more compliant (Kaliske et al. [62]). Increasing the stiffness of the cohesive interface in order to address this can in many cases lead to numerical noise and instability. A method to adaptively reduce the cohesive stiffness in the vicinity of the crack tip, in order to stabilize and reduce the noise in the numerical analysis, was devised by Elmarakbi et al. [29] and Hu et al. [56]. Although this method was capable of reducing the numerical noise, it still required embedding cohesive elements in large regions of the model, where delamination is expected to take place.

One solution to the above problems is to use an adaptive approach, where cohesive elements could be locally and adaptively inserted into the finite element model as the delamination crack propagates. Park et al. [105] used an adaptive technique, where a two-dimensional triangular mesh was adaptively refined and coarsened around the crack tip, and cohesive elements were inserted into the finite element mesh, in order to simulate 2D *in-plane* crack propagation in isotropic materials. Kawashita, Bedos, and Hallett [64] used an approach to simulate *in-plane* matrix crack propagation through adaptive element splitting and insertion of in-plane cohesive zones into the model.

A novel adaptive method, which allows adaptively seeding cohesive elements into the structure and is intended to simulate delamination in an adaptive manner, will be presented in Chapter 3, followed by verification of the method for Mode-I, Mode-II, and Mixed-Mode loading conditions (Chapter 4). In Chapter 5, the method is applied to various engineering applications. The results obtained using the current methodology are compared against available experimental results, as well as to results obtained using other numerical techniques. The numerical advantages of the method are described in Chapter 6.
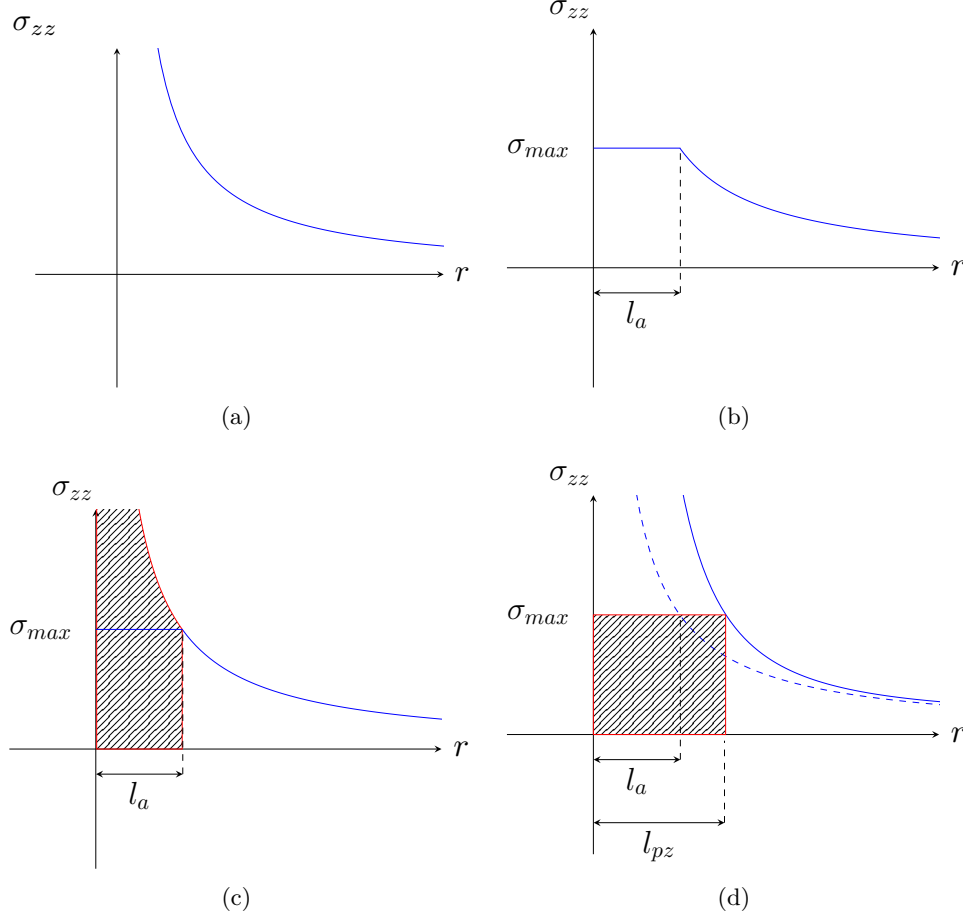
Figure 2.5: Typical σ_{zz} profiles obtained using Equation 2.2 with $\phi = 0$, as a function of the distance from the crack tip, r. **a.)** Stress profile as suggested by [128] (Equation 2.2), predict infinite σ_{zz} values at $r = 0$. **a.)** According to Irwin [59], due to the material's yielding and crack propagation, the stress levels are limited by some limiting value, σ_{max}. **c.)** Irwin introduced the geometrical distance l_a, in which the relation $\sigma_{zz} = \sigma_{max}$ is satisfied. Since the maximum stress levels are limited to σ_{max}, equilibrium is not conserved. c.) Irwin suggested a correction to l_a, which is now increased and termed the plastic zone size (l_{pz}). l_{pz} is determined such that the hatched area under the corrected stress profile (d), will be equal to the hatched area in (c), thus maintaining the global equilibrium (Equation 2.7).

Chapter 3

A Local Cohesive Zone Method for Simulation of Interlaminar Damage in Laminated Composite Materials

3.1 Introduction

The increasing use of composites in advanced engineering applications, together with the improvement of the available computational power and finite element codes, raises the need to develop efficient and reliable numerical tools to predict their behavior under various loading conditions. Numerically predicting failure and damage in these materials, requires correct numerical representation of the various damage mechanisms within which contribute to their behavior. Chapter 1 emphasized the need to simulate delamination, one of the most dominant damage mechanisms in composites. A brief review of the dominant numerical methods aimed at simulating delamination was presented in Chapter 2. It was shown that although various numerical methods to simulate this failure mode do exist, their application to larger numerical models still presents a considerable computational challenge. Amongst the various numerical methods aimed at simulating delamination in composite materials, the cohesive-zone method is becoming the method of choice by researchers and engineers, due to its reliability, its applicability to commercial finite element solvers, and its relative numerical simplicity [4]. Despite its benefits, the high computational cost of the method when an increased number of cohesive interfaces is used, renders the method unfeasible for solving large engineering models. In addition, the method can effect the compliance of the structure, thus introducing unwanted numerical error to the analysis. Some adaptive cohesive approaches were discussed in Chap-

ter 2, in which adaptive introduction of cohesive zones is used in order to alleviate the drawbacks of the method when applied to larger models.

The contribution of the present work is in the development of a new method which allows simulating the initiation and growth of *delamination* damage in an adaptive manner. Using this method, the structure can be modelled with only one layer of elements through the thickness. During the transient analysis, the continuum elements are locally and adaptively split through their thickness, and cohesive elements are introduced in regions where delamination has the potential to initiate and grow. Delamination can thus propagate in the structure as the simulation progresses. Reducing the number of cohesive elements present in a model contributes to the reduction of the computational cost, as well as alleviating the unwanted artificial stiffness reduction caused when cohesive-elements are embedded in large regions of the model.

3.2 Main Principles of the LCZ Method

The adaptive element splitting technique presented here is based on the notion that only a minimal number of cohesive elements need to be be present in a finite element model in order to correctly describe the delamination crack propagation, and cohesive elements should only be introduced where and when needed during the analysis. Using this method, the structure made of the composite material can be modelled using only one layer of structural elements. Delamination cracks and crack-growth paths do not need to be defined in the model prior to the analysis, as they are created adaptively during the course of the transient simulation. . This is demonstrated in Figure 3.1.a and Figure 3.1.b: Figure 3.1.a shows the conventional implementation of the CZM. A cohesive interface is defined apriori of the finite element analysis, along the potential delamination crack interface. As delamination propagates, nodes located along the interface are released and new free surfaces are created (Figure 3.1.b). Simulating delamination using the Local Cohesive Zone method, requires no cohesive interface to be defined apriori of the finite element analysis (Figure 3.1.c). As the finite element analysis progresses, a user-defined element splitting criterion is evaluated within the continuum elements. When this criterion is satisfied, the continuum finite elements are split through their thickness, and cohesive elements are locally seeded along a narrow band ("cohesive band") that is wide enough to capture the delamination crack propagation (Figure 3.1.d). The cohesive band can propagate through the structure as the transient analysis pro-

gresses. This is demonstrated in Figure 3.2, where a DCB problem is solved using the LCZ algorithm. The cohesive-band migrates as the delamination crack propagates along the structure, shown here in three subsequent stages - starting at stage **a)**, propagating to stage (Figure 3.2.a, Figure 3.2.b and Figure 3.2.c).

The method is implemented through the development of a computer code governing the transient finite element analysis, written in Python. The structural problem is solved using the commercial explicit finite element code LS-DYNA [18], while the LCZ algorithm monitors the solution and performs the various operations as the transient analysis progresses, such as element splitting and introduction of new cohesive elements into the model. The following section will give a brief description of the main operations performed by the LCZ algorithm, and the main variables controlling its behavior.

A schematic flow-diagram demonstrating the relation between the LCZ algorithm and the finite element solver is shown in Figure 3.3.

The following sections describe the main execution stages. Two related models were chosen in order to demonstrate the method. Both models describe a similar structural problem - loading of a cantilever beam under a "splitting" type load. The first model is presented in a simple two dimensional view (Figure 3.4). Here, a cantilever beam of length l and thickness h, is subjected to a splitting displacement Δ at its other end. A three-dimensional model, with a larger number of elements, is shown in Figure 3.5, in order to demonstrate other features in the model, not visible in the two dimensional view. A schematic flow chart demonstrating the algorithm behavior is presented in Appendix A.

3.3 LCZ Algorithm Overview

3.3.1 Problem Initialization

During the initialization phase, the LCZ algorithm receives the LS-DYNA input file, which includes the material definitions, as well as the boundary and initial conditions. Once initiated, the algorithm executes independently and controls the transient analysis until the final termination time is reached.

As opposed to the implementation of the conventional CZM, the current methodology does not require explicit modelling of the cohesive interface and cohesive elements prior to the analysis. In most examples described in this thesis, only a single layer of continuum elements was used through the thickness of the composite part, without a priori introduction of cohesive

Figure 3.1: **a).** When simulating delamination using the conventional implementation of the cohesive zone method, the cohesive interface is defined prior to the finite element analysis, along the potential delamination crack interface. **b).** As delamination propagates, interface nodes are released and new free surfaces are created. **c).** When simulating delamination using the Local Cohesive Zone method, no cohesive interface is defined a priori. **d).** When an element splitting criterion is satisfied, the continuum finite elements are split through their thickness and cohesive elements are locally seeded along a narrow band ("cohesive band").

Figure 3.2: Typical cohesive-band created when solving a DCB problem using the LCZ algorithm. The cohesive-band migrates as the delamination crack propagates along the structure, shown here in three subsequent stages - starting at stage **a)**, propagating to stage **b)** and finally **c).**
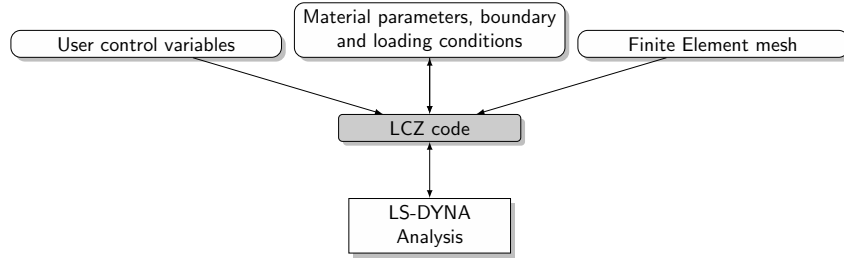
Figure 3.3: A schematic flow diagram demonstrating the relation between the LCZ algorithm and the finite element solver (LS-DYNA).

elements in the model. In this case, the continuum elements chosen for the solution were LS-DYNA's built-in Thick-Shell elements [18], which allow the user to specify a different material angle for each through-thickness integration point. These elements assume a parabolic distribution of the out-of plane shear stresses (τ_{zx}) through the thickness of the element. While this assumption might not be valid for every composite laminate system, for the cases considered here, it did not seem to result in significant errors.
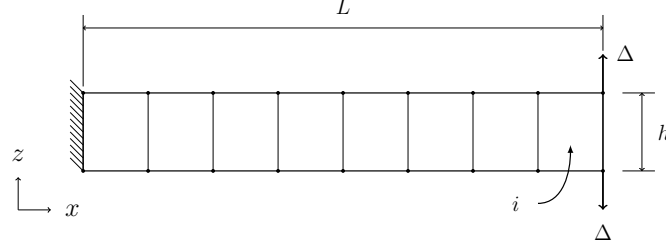
Figure 3.4: A simple numerical model used to demonstrate the LCZ algorithm - a cantilever beam with a length L and thickness h under splitting loading condition. One end of the beam is subjected to two opposing applied displacements, Δ.

3.3.2 Element-Splitting Criteria

Once the transient analysis has been initialized, the continuum elements continue to be monitored in order to determine whether or not cohesive elements should be introduced into the finite element mesh. An *element splitting criterion*, based on a critical value S_c of a quantity S, is defined in order to evaluate the specific location where the cohesive elements should be introduced. Whenever S reaches the value of S_c in a specific element, a *through-thickness* element splitting operation is performed, and cohesive elements are locally introduced at the splitting interface. It is important to note that the value of S_c should not be viewed as a delamination threshold, as the actual delamination and delamination crack propagation will be governed by the cohesive element traction-separation law. Instead, S_c serves as a flag to determine when and where the potential for the delamination growth should be seeded into the model, by introducing the cohesive elements into the finite element mesh. For simplicity, let us now consider this criterion to be a normal out-of-plane stress value in the global z direction (3.1), where z denotes the direction normal to the surface of the composite part, and σ_{zz}^c denotes the critical σ_{zz} value. Splitting takes place whenever S is equal to or exceeds S_c (Equation 3.2).

$$S_c = \sigma_{zz}^c \tag{3.1}$$

$$S \geq S_c \tag{3.2}$$
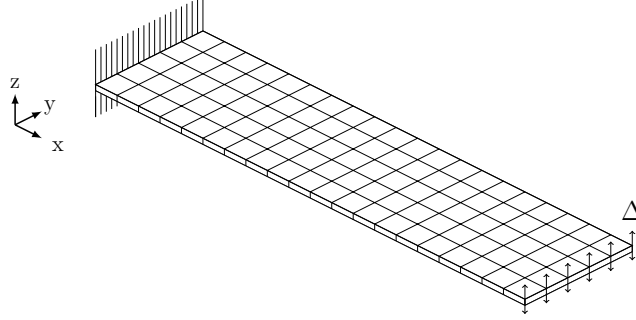
Figure 3.5: Isometric view of the detailed cantilever beam model used for demonstrating the LCZ algorithm - supported cantilever beam under splitting loading condition. One end of the beam is subjected to two opposite displacement constraints Δ.

As the applied displacement, Δ, is increased, at some instance in time, S reaches a user-defined critical value of S_c within the thick-shell element i in Figure 3.6. Thick shell element i is now flagged as a *parent-element* flagged for splitting, and the algorithm now proceeds to the next phase, which is described in the following section.

3.3.3   Radial Neighbour Search

In order for CZMs to correctly capture the mechanical crack propagation, a number of cohesive elements should be included across the active cohesive zone (Mi et al. [91], Harper et al. [52]). In order to increase the number of thick-shell elements which will be split by the code, a radial geometrical search is now performed for all neighbouring thick-shell elements with centroids that lie within a user-defined distance R_1 from the centroid of the element i (Figure 3.6.a). All of the thick-shell elements satisfying this geometrical search, including element i, are added into an initially empty set of elements, A, which will include all thick-shell elements flagged for splitting, and are shaded in Figure 3.6.a using a green color. Since the value of R_1 used in this example is small, thick-shell elements j and k are not depicted by the radial search, and are therefore not added to the element set A. This is an undesirable outcome - assuming that the load Δ is evenly

distributed along the edge of the beam, the value of S in these elements approaches S_c, and it is mechanically feasible that these elements will be split as well. Increasing the value of R from R_1 to R_2 (Figure 3.6.b) will now result in a larger region of thick-shell elements to be included within element set A (Shaded in red and green in Figure 3.6.b). Element set A will now include thick-shell element i, as well as thick-shell elements j and k. However, the boundaries of the geometrical region bounding element set A (and is marked by line $\bar{ab}$ in Figure 3.6.b), do not cross the beam along its width perpendicular to the beam's main axis. It is expected that given the evenly distributed load Δ, the element set A will be bounded by a straight line (similar to line $\bar{ac}$ in Figure 3.6.b). A second search operation which is described in the following section, is now performed in order to improve the results.

3.3.4 Threshold Neighbour Search

Ir order to improve the mechanical feasibility of the results obtained by the radial search, a threshold filter is now added to the search (Figure 3.7): Once S reaches a value of S_c within a thick-shell element i, all thick-shell elements which satisfy the following equation are flagged for splitting and are included in element set A:

$$S \geq threshold \times S_c \qquad (3.3)$$

where *threshold* is a user-defined scalar, having a value which is higher than 0 and lower than 1.

Adding the threshold filter, and choosing an appropriate value for the *threshold* parameter, will result in all thick-shell elements located along the edge of the beam where Δ is applied, to be included in element set A (Figure 3.7.a). The geometrical search is now performed separately, for *each* element included in element set A. The thick-shell element in set A for which the search is performed is termed the *parent element*. Each thick-shell element who has its centroid lie within a distance R of the parent element, will be added to element set A. this will result in a mechanically feasible region of elements which will flagged for splitting, shown in Figure 3.7.b. This region consists of thick-shell element i, which was the first thick-shell element to reach a value of $S = S_c$, a row of thick-shell elements shaded in green, which satisfied the threshold search (Equation B.4), and a region of thick-shell elements shaded in red, which satisfied the radial search.

(a)

(b)
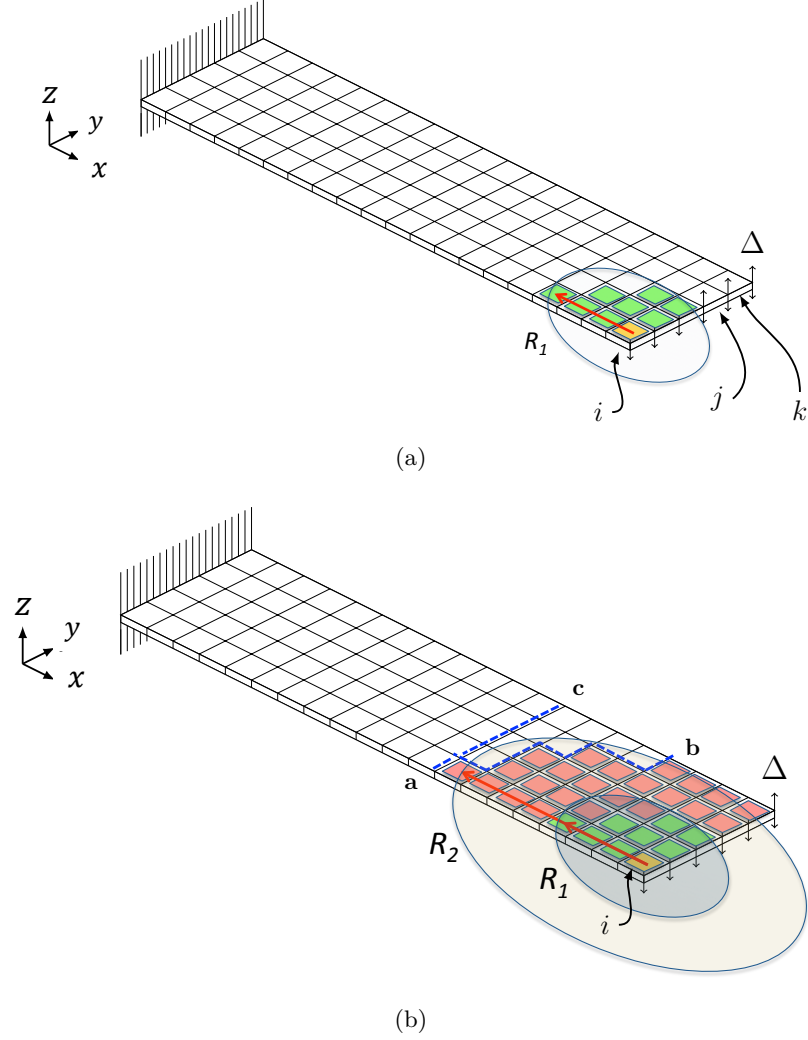
Figure 3.6: **a).** Isometric view of a double cantilever beam (DCB) subjected subjected to an evenly distributed splitting displacement Δ. Delamination propagation through the beam is modelled using the LCZ method. A radial search is performed to find all neighbouring elements which lie within a radius R_1 of element i satisfaying the element splitting criterion. **b).** The boundaries of the geometrical region found using this search process do not cross the beam along its width, which would be more feasible given the evenly distributed splitting displacement.

(a)

(b)
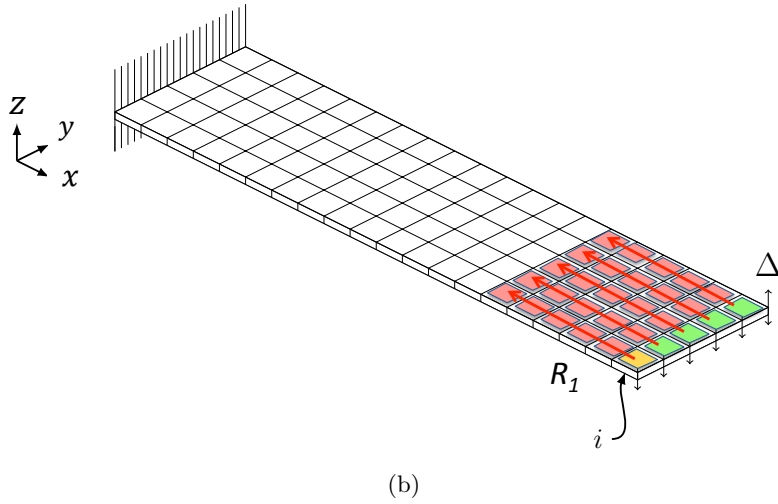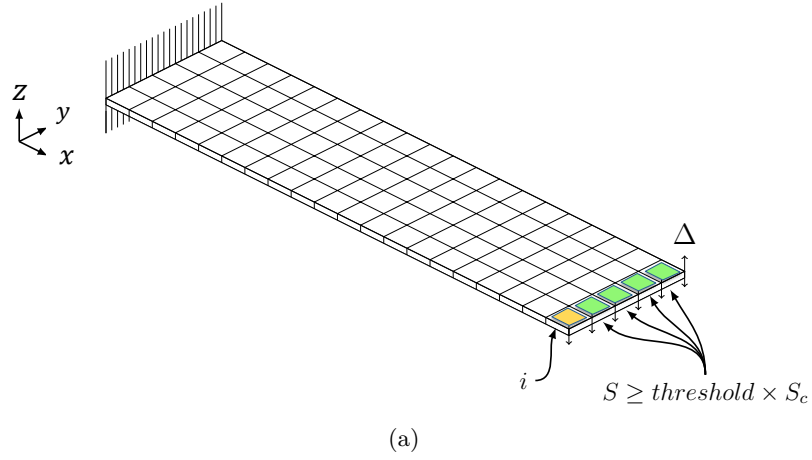
Figure 3.7: **a).** A threshold value is applied to the element splitting crite-rion. **b).** Applying the threshold results in a physically feasible region of thick-shell elements to be flagged for splitting.

3.3.5 Through-Thickness Element Splitting and Local Insertion of Cohesive Elements

Once element-set A is obtained, through-thickness element splitting and local insertion of cohesive elements are performed. A side view of a schematic element splitting process is shown in Figure 3.8. Here, LS-DYNA's thick-shell element is being split into two offset shell elements (Figure 3.8.**a**). Offset-shell elements have their nodes lie on the virtual element-surface, and not on the mid-plane of the shell. The element formulation takes this offset into account when computing the stresses and strains in the elements. The offset shell elements are sharing the same nodes as the parent thick-shell element, i.e, no nodes are deleted or added during the process. During the splitting operation, all history variables belonging to the integration points of the parent thick-shell element (i.e stresses, damage variables, etc.), are mapped to the integration points of the new offset-shell elements created during the splitting process (Figure 3.8.**b**). Once splitting is performed, a solid cohesive element connecting the two offset shell elements is created (Figure 3.8.**c**). The solid cohesive element behaves as a system of springs which transmits traction forces across the cohesive interface, based on the traction-separation law defined within the cohesive material model, and the relative displacement of the nodes belonging to the offset shell elements (Figure 3.8.**d**). A contact algorithm, schematically represented here using orange marks, is defined between the new offset shell elements, in order to account for contact between the offset shell elements in case delamination will develop (Figure 3.8.**e**).

Connecting meshes having different element topologies, i.e offset shell elements and thick-shell elements, poses some numerical difficulties. This is demonstrated in Figure 3.9. LS-DYNA's thick-shell elements have translational DOF and no rotational DOF, whereas LS-DYNA's offset shell elements have translational, as well as rotational DOF (Figure 3.9.**a**). Due to the lack of rotational DOF in the thick-shell elements, moments can not be transmitted at locations where offset shell elements are connected to a thick-shell element. This is demonstrated at Figure 3.9.**b**, where load P will cause rotation of offset shell element i, as thick-shell element j can not resist its rotation, and node w acts as a pivot point. By adding offset shell elements k and l which overlap thick-shell element j (Figure 3.9.**c**), moments could be transferred between the two different mesh topologies, resisting the rotational movement of offset shell element i due to the load P. Adding the offset shell elements on top of the thick-shell elements results in an unrealistic numerical representation of the material. However, since the overlapped
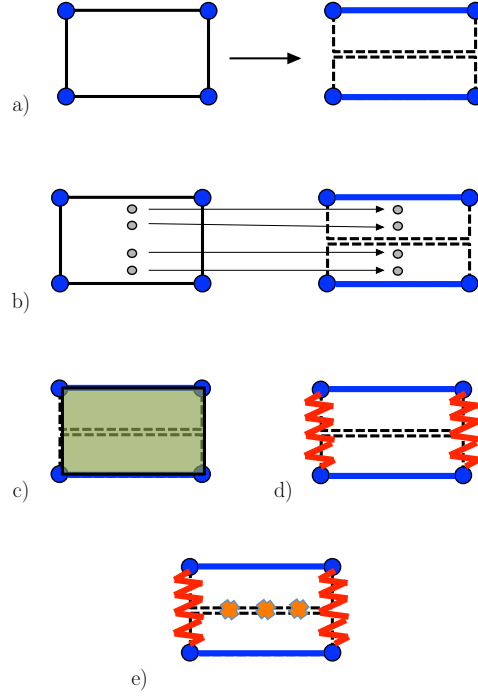
Figure 3.8: A side view of a schematic element splitting process. **a.)** LS-DYNA's thick-shell element is being split into two offset shell elements. The two offset shell elements created during the splitting process, are defined using the nodes of the parent thick-shell element. **b.)** During the splitting operation, all history variables belonging to the integration points of the parent thick-shell element, are mapped to the integration points of the new offset-shell elements created during the splitting process. **c.)** A solid cohesive element connecting the two offset shell elements is created, and is defined such that it shares all of its nodes with the offset shell elements. **d.)** The solid cohesive element behaves as a system of springs which transmits traction forces across the cohesive interface, based on the traction-separation law defined within the cohesive material model, and the relative displacement of the nodes belonging to the offset shell elements. **e.).** A contact algorithm, schematically represented here using orange marks, is defined between the new offset shell elements, in order to account for contact between the offset shell elements in case delamination will develop.

region is created over a very narrow band in the model, only at the shared boundaries connecting the two mesh topologies, it is expected that the error introduced due to this unrealistic numerical representation will be localized and minimal. For the cases being investigated within this work, it was found to have a negligible effect on the final results obtained from the analysis.
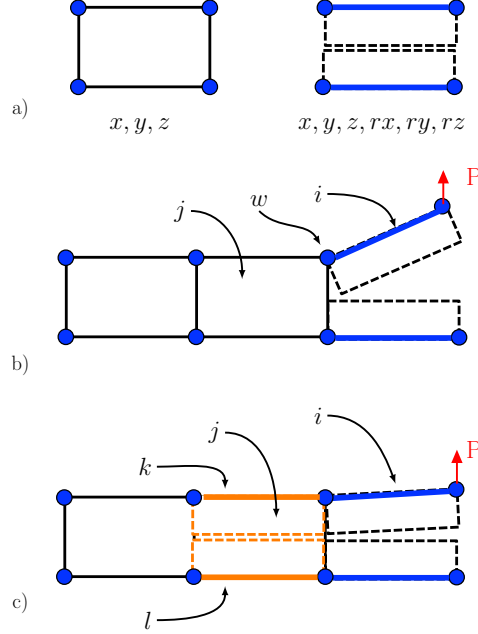
Figure 3.9: A schematic side view demonstrating some numerical limitations of connecting LS-DYNA's thick-shell elements with LS-DYNA's offset shell elements. **a.)** LS-DYNA's thick-shell elements have translational DOF and no rotational DOF, whereas LS-DYNA's offset shell elements have translational, as well as rotational DOF. **b.)** Due to the lack of rotational DOF in the thick-shell elements, moments can not be transmitted at locations where offset shell elements are connected to a thick-shell element. This is demonstrated here, where load P will cause the rotation of offset shell element i, as thick-shell element j can not resist its rotation. **c.)** Adding offset shell elements k and l which overlap thick-shell element j, will allow moments to be transferred between the two different mesh topologies, resisting the rotational movement of offset shell element i due to the load P.

Figure 3.10.a shows a schematic beam topology, modeled using a single through-thickness layer of thick-shell elements. The beam is constrained at

one of it ends, and is loaded via a splitting load Δ along its free end. Figure 3.10.b shows the beam immediately after a splitting operation has been performed. During the element splitting process, the continuum elements flagged for splitting (Thick-shell elements in set *A*) are split into two layers of offset-shell elements, and solid cohesive elements to which LS-DYNA's *MAT COHESIVE GENERAL is assigned, are implanted along the newly created interface. A mapping operation is performed in order to transmit all history variables from the thick-shell elements to the offset shell elements replacing the thick-shell elements during the element splitting process. Overlapping offset-shell elements are created on top of the thick-shell elements, but only for the thick-shell elements that share a boundary with the split region (Figure 3.10.b). The overlapping offset-shell elements, generated by the LCZ algorithm, share the same nodes as the parent thick-shell element, thus occupying the same volume.

The splitting process performed during this stage is not the actual delamination in the material. It is merely a means to locally "seed" the delamination potential in the structure. The delamination growth will be governed by the cohesive laws related to the cohesive-elements seeded into the structure.

Once splitting and insertion of cohesive elements is performed, the transient analysis is resumed using the new element topology, and the continuum thick-shell elements are again monitored for further splitting.

3.3.6 Propagation of the Local Cohesive Zones

Once the splitting process is completed and the dynamic analysis continues, cohesive zones can further propagate into the structure. A schematic example of the cohesive zone propagation is shown in Figure 3.11. A side view of the cantilever beam at the beginning of the analysis can be seen in Figure 3.11.a. The beam is subjected to a displacement splitting constraint Δ applied to end of the beam. Figure 3.11.b shows the beam right after the first splitting cycle. To the left of the beam are 3 thick-shell elements (labeled D) which were not split during the splitting step. Next to them lies a single thick-shell element (labeled E) overlapped by two offset-shell elements. The rest of the beam consists of two layers of offset-shell elements, and solid cohesive elements that connect these two layers.

Figure 3.11.c shows the states of the cohesive zones in each cohesive element, during the initial stages of the loading process right after splitting has occurred. Each cohesive element is marked with a number. Cohesive elements 8 to 5 do not undergo any normal peeling tension, and therefore
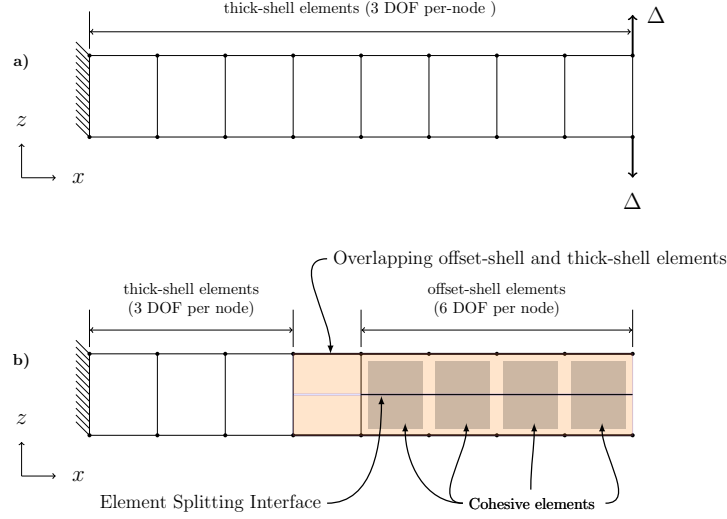
Figure 3.10: Schematic side view of a DCB subjected to a splitting load modelled using the LCZ method. **a.)** The beam is modelled using a single through-thickness layer of LS-DYNA's thick shell elements, with 3 DOF per node. A splitting displacement Δ is applied to the end of the beam. **b.)** Once splitting takes place, thick-shell elements are replaced by offset-shell elements, connected using solid cohesive elements. In order to correctly transmit the bending-moment from the offset shell elements to the thick-shell elements, the resulting topology includes a single thick-shell element overlapped by two offset-shell elements. A contact algorithm is defined between the newly created surfaces to account for contact between the crack surfaces.

remain at a 0 cohesive state and exert no cohesive force on the structure. Cohesive element 4 just begins the loading phase, and cohesive elements 3 and 2 have already been strained by the loads applied to them. Cohesive element 1, located at the end of the beam, has the largest crack-opening displacement, therefore the force transmited by its cohesive state is about to diminish. When the force transmited by this element reaches a value of 0, the element will be deleted.

The first cohesive element deletion is shown in Figure 3.11.d. The cohe-

sive elements 1 and 2 have gone through their complete softening path in the traction-separation law, and have therefore been deleted. The cohesive elements 3 and 4 have partially softened while cohesive elements 5 and 6 are still in their elastic loading state, and continue to absorb energy as the crack propagates. At this stage, the cohesive elements 7 and 8 are not loaded. At some point in time, as the applied loading increases, cohesive elements 7 and 8 will be loaded, and the critical element splitting criterion (Equation 3.2) will be satisfied in thick-shell element E. At this moment, the next splitting phase will take place, as can be seen in Figure 3.11.e, and more cohesive elements are seeded along the length of the beam (elements 10 to 12). As cohesive elements 3 and 4 are deleted, the crack opening increases further. The cohesive elements 5 to 8 each undergo a different state of loading along the traction-separation curve.

Typical results from a three-dimensional beam splitting simulation are shown in Figure 3.12. Here, the resulting cohesive band is identified with darker shade. The figure shows the manner in which the local cohesive band migrates and propagates into the structure as the crack opens. Cohesive elements are locally and adaptively introduced in the model, and only at specific locations where delamination is about to take place, thus reducing the computational costs.

3.4 Multi-Delamination Capability

In order to simulate multiple through-thickness delamination cracks using the conventional CZM, cohesive interfaces should be defined along all potential delamination crack paths prior to the analysis (Figure 3.13.a). Recent developments of the LCZ algorithm allow multiple through-thickness delamination cracks to propagate through the laminate. Using the LCZ method, no a priori cohesive elements should be present in the model (Figure 3.13.b). Multiple delamination cracks can simultaneously and independently propagate through the thickness of the structure (Figure 3.13.c).

In order to allow multiple delamination cracks to be simulated using the LCZ method, the number of through-thickness thick-shell elements should be equal to the number of potential delamination interfaces in the structure. Independent cohesive properties can be defined for each interface and for each mode of loading. In this case, the behavior of the LCZ algorithm is similar to the case where a single delamination crack is present in the model, except for the geometrical search performed on all thick-shell elements satisfying the threshold search. This is demonstrated in Figure 3.15,

where a schematic of the LCZ search algorithm performance is presented for a case of multi-delamination analysis. Figure 3.15.a shows a side view of a beam modelled using 3 through-thickness layers of thick-shell elements. The beam is subjected to a displacement Δ, applied at various locations along the beam. As Δ is increased, thick-shell element i is the first element in which S reaches S_c. This element is added to an initially empty set of thick-shell elements A. A threshold search is now performed, for all thick-shell elements which satisfy Equation B.4 (Figure 3.15.b). Suppose thick-shell element j satisfies Equation B.4, and is thus added to element set A. A geometrical radial search is now performed (Figure 3.15.c), for all thick-shell elements which are included in element set A (thick-shell element i and thick-shell element j). For each element in set A, a radial search is performed using a user-specified geometrical radius R. The thick-shell element in set A for which the search is performed is termed the *parent element.* Each thick-element found in the search, whos its centroid fall within a radial distance R of the centroid of the parent element, is added to element set A, *only* if it shares the same thick-shell element ply with the parent element. In this example, thick shell elements i_1, i_2, i_3 and i_4 all satisfy the radial search with respect to the parent thick-shell element i, as well as share the same thick-shell layer as element i, and are therefore added to element set A. The centroid of thick-shell element m is within a distance R from the centroid of thick-shell element i, but since it does not belong to the original thick-shell element layer of element i, it is not added to element set A. Similarly, thick-shell elements j_1 and j_2 satisfy the radial search with respect to parent thick-shell element j, as well as share the same thick-shell layer as element j, and are therefore added to the element set A. Similar to above, since element n does not belong to the original thick-shell element layer of element j, it is not added to the element set A even though its centroid falls within the radial distance R of element j's centroid.

Once the element set A is populated, the algorithmic details follow a similar process to that involving a single delamination interface, i.e, mapping and element splitting are performed, together with the insertion of cohesive elements. The transient analysis is resumed using the new element topology, and the continuum thick-shell elements are monitored again for further splitting.
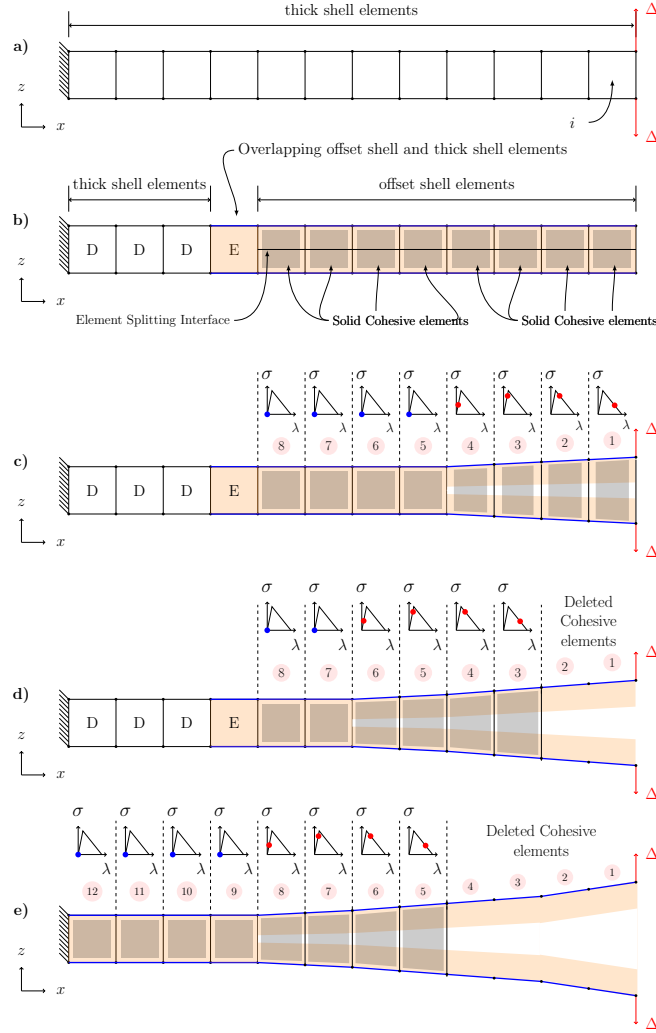
Figure 3.11: Schematic progression of the cohesive zones using the LCZ algorithm, for a cantilever beam-splitting example. **a).** Before splitting, the model consists of a single layer of thick-shell elements. A splitting displacement constraint, Δ, is applied at the end of the beam. **b).** First splitting step. **c).** Solid cohesive elements are being loaded as the crack is opened. Schematic representation of the cohesive state for each cohesive element can be seen above the beam. **d).** Cohesive elements are deleted as the crack propagates along the beam. **e).** Second splitting step is performed and the crack propagates further into the beam.
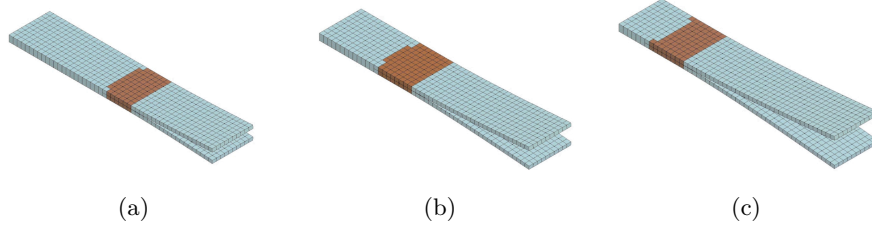
Figure 3.12: Typical cohesive-band created when solving a DCB problem using the LCZ algorithm. The cohesive-band migrates as the delamination crack propagates along the structure, shown here in three subsequent stages -starting at stage **a)**, propagating to stage **b)** and finally **c).**
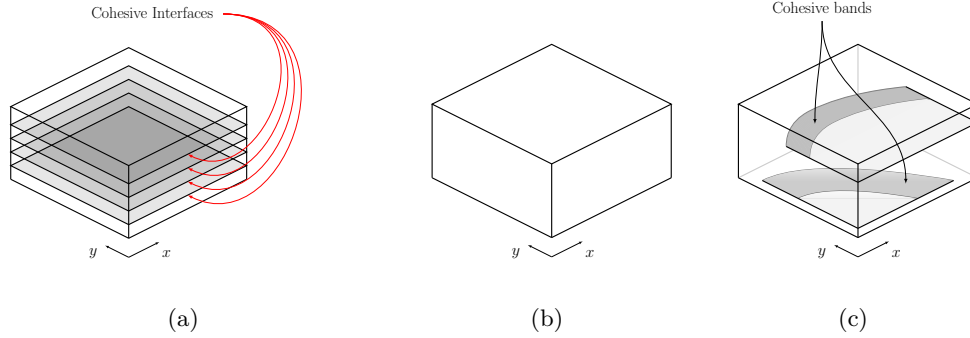
Figure 3.13: Simulating a structure having multiple delamination interfaces: **a).**Using conventional CZM, cohesive interfaces should be defined along all potential delamination crack paths prior of the analysis. **b).** Using the LCZ method, no cohesive elements should be present in the model prior of the analysis. **c).** Using the LCZ method, Multiple delamination cracks can simultaneously and independently propagate through the thickness of the structure.
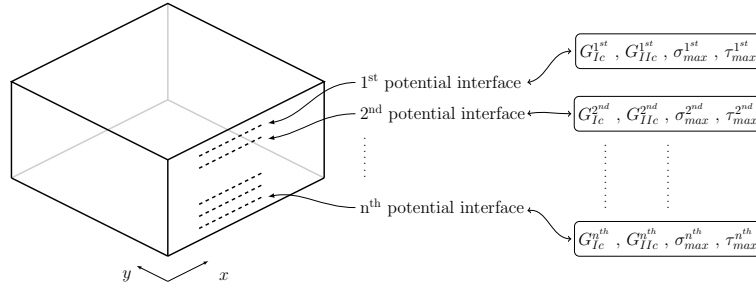
Figure 3.14: Using the LCZ method, multiple delamination cracks can be treated simultaneously, by defining independent fracture properties for each potential delamination interface.
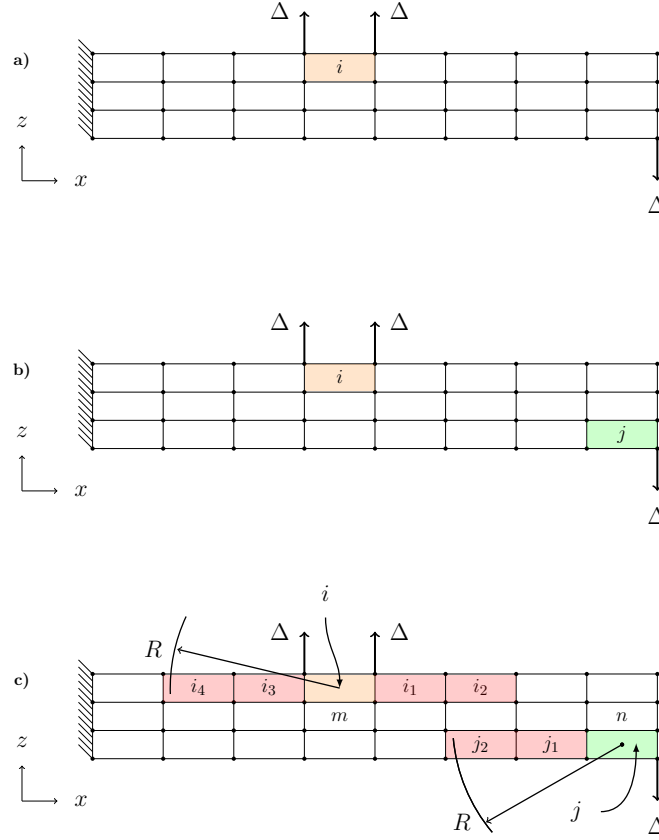
Figure 3.15: Schematic performance of the LCZ search algorithm. **a).** Side view of a beam modelled using 3 through-thickness layers of thick-shell elements. The beam is subjected to a displacement Δ, applied at various locations along the beam. As Δ is increased, thick-shell element i is the first element in which S reaches S_c. **b).** A threshold search is now performed, for all thick-shell elements which satisfy Equation B.4. Thick-shell element j satisfies the threshold criterion (Equation B.4), and is thus added to element set A. **c).** A geometrical radial search is now performed, for all thick-shell elements which are included in element set A. Thick shell elements i_1, i_2, i_3 and i_4 all satisfy the radial search with respect to the parent thick-shell element i, as well as share the same thick-shell layer as element i, and are therefore added to element set A. Similarly, thick-shell elements j_1 and j_2 satisfy the radial search with respect to parent thick-shell element j, as well as share the same thick-shell layer as element j, and are therefore added to the element set A. Thick-shell elements m and n are not added to the element set A, since they do not share the same thick-shell layer as the parent elements i or j.

Chapter 4

Verification

The correct numerical implementation of the LCZ algorithm was verified using its application to simple numerical problems, involving pure delamination crack propagation, i.e, not involving any intralaminar damage. This chapter focuses on the solution of these simple problems, where in Chapter 5, the algorithm is validated against engineering applications involving more complicated loading scenarios, as well as intralaminar damage.

The following sections describe the solution of pure Mode-I, Mode-II, and Mixed-Mode loading conditions, used as a benchmark verification problems. In all configurations tested, LS-DYNA's built-in material model (*MAT CO-HESIVE GENERAL) was chosen as the material law for the solid cohesive elements. This material model allows modelling cohesive materials using arbitrary traction-separation laws. The critical strain-energy release rates for Mode-I (G_{Ic}) and II (G_{IIc}), are specified for each loading case, together with the maximum normal (σ_{max}) and shear (τ_{max}) stresses at the cohesive elements. A normalized traction-separation curve is used (Figure 4.1), in which the normalized traction in the cohesive interface is plotted against the normalized crack opening.

The following relation was chosen as the maximum displacement at failure of the cohesive elements [18]:

$$\delta^f = \frac{1 + \beta^2}{A_{TSLC}} \left[\left(\frac{\sigma_{max}}{G_{Ic}} \right)^{XMU} + \left(\frac{\tau_{max} \, \beta^2}{G_{IIc}} \right)^{XMU} \right]^{-\frac{1}{XMU}} \tag{4.1}$$

where β is the "mode mixity", and is defined as δ_{II}/δ_I, δ_I and δ_{II} are the crack-opening in the normal and shear directions, respectively, A_{TSLC} is the area under the normalized traction-separation curve, and XMU is a failure parameter, which has a default value of 1.0 in LS-DYNA. This default value was used for both the Mode-I and Mode-II loading cases. However, for the mixed-mode loading scenario, XMU was set equal to 1.5 in order to obtain meaningful results.
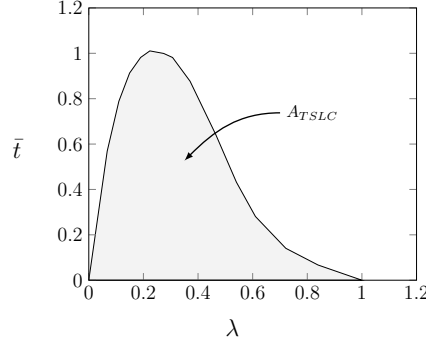
Figure 4.1: Normalized traction-separation law used in the cohesive material model. The normalized crack opening, λ, is defined as: $\lambda = \frac{\delta}{\delta^f}$, where δ is the crack opening, and δ^f is the crack opening to failure. The normalized traction, $\bar{t}$, is defined as t/t_{max}, where t is the traction, and t_{max} is the maximum traction stress, taken as σ_{max} or τ_{max} from Table 4.1, depending on the opening mode. A_{TSLC} is the area under the normalized traction-separation curve.

4.1 Mode-I delamination

A Double Cantilever-Beam example (DCB), described in detail in [5], was simulated using the LCZ algorithm (Figure 4.2). The example consists of a beam of length $L = 100$mm, thickness $h = 3$mm, and width of 20mm. A crack of an initial length $a = 30$mm is present in the beam. A splitting displacement Δ, in the global z direction, is applied at the end of the beam. The material and cohesive interface parameters used in the analysis are listed in Table 4.1.

The beam was modelled using two layers of thick-shell elements, with the expected crack growth path pre-defined prior to the analysis (Figure 4.3). The crack path was defined using a layer of solid cohesive elements, located along the interface layer of length $L - a$ along the beam. The initial crack, of length a, was defined in the model by using two layers of thick-shell elements with no cohesive elements in between.

In order to allow reasonable solution times, the typical element size used in the finite element model along the crack propagation direction was 2 mm. Alfano and Crisfield [5] used 0.25 mm element size, together with a maximum cohesive traction stress value, σ_{max}, equal to 57 MPa. The
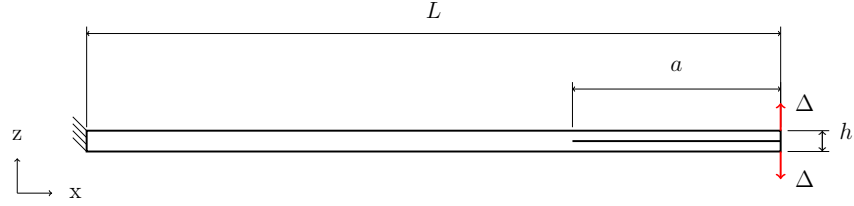
Figure 4.2: DCB test case, consists of a beam with length $L = 100$mm, thickness $h = 3$mm, and width of 20mm. A crack of an initial length $a = 30$mm is present in the beam. A splitting displacement Δ, in the global z direction, is applied at the end of the beam.

following section describes the the investigation that was performed in order to obtain the value of σ_{max} that will allow obtaining reliable results using a 2 mm mesh.
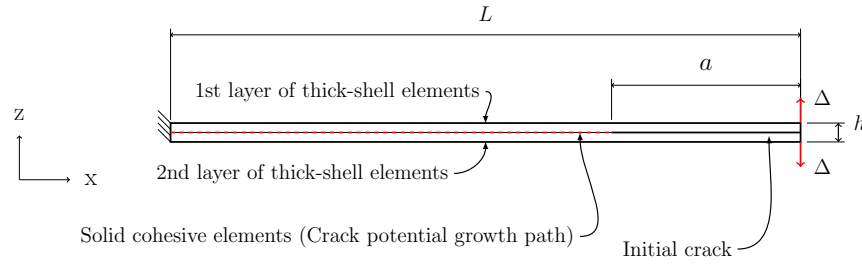
Figure 4.3: Schematic side view of the DCB finite element model. The beam is modelled using **two** layers of thick shell elements, with cohesive elements pre-defined along the potential delamination crack path.

Table 4.1: Material properties used in the numerical verification problems

Property	DCB [a] (Mode-I)	ENF [b] (Mode-II)	MMB [b] (Mixed-Mode)	Unit
Density	1.34×10^{-3}	1.34×10^{-3}	1.34×10^{-3}	g/mm^3
Elastic				
Longitudinal elastic modulus (E_{xx})	135.3	135.3	135.3	GPa
Transverse elastic modulus (E_{yy})	9	135.3	9	GPa
Out-of-plane elastic modulus(E_{zz})	9	135.3	9	GPa
Major Poisson's ratio, in plane (ν_{xy})	0.24	0.25	0.24	(-)
Major Poisson's ratio, out-of-plane (ν_{xz})	0.24	0.25	0.24	(-)
Poisson's ratio, transverse plane (ν_{yz})	0.46	0.25	0.46	(-)
In-plane shear modulus (G_{xy})	5.2	–	5.2	GPa
Transverse shear modulus (G_{xz})	3.08	–	3.08	GPa
Out-of-plane shear modulus (G_{zx})	5.2	–	5.2	GPa
Interlaminar damage				
Interlaminar normal strength (σ_{max})	8 [c]	-	57	MPa
Interlaminar shear strength (τ_{max})	-	57	57	MPa
Mode I critical energy release rate, (G_{Ic})	0.28	–	4	kJ/m^2
Mode II critical energy release rate, (G_{IIc})	–	4	4	kJ/m^2

[a] Source: [5].
[b] Source: [91].
[c] Source: Value obtained from preliminary simulations, described in Section 4.1.1.

4.1.1   Obtaining the Cohesive Properties

In Section 2.2, a brief description of the CZM was given. It was stated that in order for the CZM to correctly describe delamination crack propagation within an interface, the cohesive zone should span across several cohesive elements along the crack propagation direction. Using the out-of-plane elastic modulus, together with a maximum traction stress of $\sigma_{max} = 57$ MPa (which is the value used by Alfano and Crisfield [5] to solve a similar DCB problem), the obtained value of the cohesive zone size is $0.16 < l_{pz} < 0.77$, depending on the approximation method which appear on Table 2.1. Assuming that the element size along the crack propagation direction should allow several elements to span across the cohesive zone, a mesh size much finer than 2 mm should be used.

It was shown by Alfano and Crisfield [5] that the maximum traction stress, σ_{max}, can be reduced in order to increase the cohesive zone length,

l_{pz}, thus allowing coarser mesh to be used in the analysis. Alfano and Crisfield [5] used a value of $\sigma_{max} = 37$ MPa together with a 1 mm mesh for the solution of the DCB problem under investigation, which still yielded a reasonable solution.

In order to investigate the effect of σ_{max} on the numerical solution obtained using a 2 mm mesh, the problem was solved using different values of σ_{max}, while keeping $G_{Ic} = 0.28$ kJ/m² constant. All models were solved using LS-DYNA's explicit solver together with the default time step size. The average run-times for each model was approximately 7 minutes, when using a cluster of 12 Intel Xeon 2.40GHz processors having 6 cores each for the solution.

Figure 4.4 shows the force vs. crack opening displacement plot, obtained from σ_{max} values of 57 MPa, 8 MPa and 1 MPa, compared to the numerical solution obtained by Alfano and Crisfield [5] using a 0.25 mm fine mesh and the VCCT method. It can be seen that σ_{max} value of 57 MPa results in over-prediction of the force profile, both at the elastic loading stage, as well as the post peak, crack-propagation stage. Numerical noise is present as well, which is due to the crack front moving from one cohesive element to the other. Using a value of $\sigma_{max} = 8$ MPa, results in better agreement with the VCCT solution. Although the response is slightly more compliant during the elastic loading stage, better prediction is obtained for the maximum peak force, and the results follow the Alfano and Crisfield's solution during the crack propagation stage, with slight numerical noise which is present as the crack propagates. When the cohesive interface is modeled using a value of $\sigma_{max} = 1$ MPa, the compliance of the structure during the elastic loading phase is further increased, and under-estimation of the peak force is noticeable as well. The response, however, exhibits less noise from the higher values of σ_{max} tested.

In order to shed more light on the results shown in Figure4.4, the normal (out-of-plane) traction stress in a row of neighbouring cohesive elements located along the crack propagation direction was monitored as the interface was loaded. Figure 4.5 shows the numbering method used in order to analyze the results. The solid cohesive elements are numbered in an increasing order, such that the 1st element is the element adjacent to the initial crack. The results from this study appear in Figure 4.6, Figure 4.7 and Figure 4.8.

Figure 4.6.a shows a typical state of the normalized traction stress in the cohesive elements, using $\sigma_{max} = 57$ MPa. It can be seen that the cohesive zone spans across a single element along the crack propagation direction. Figure 4.6.b shows the normal traction stress in the first 7 cohesive elements, vs. the crack opening displacement. The results are displayed for
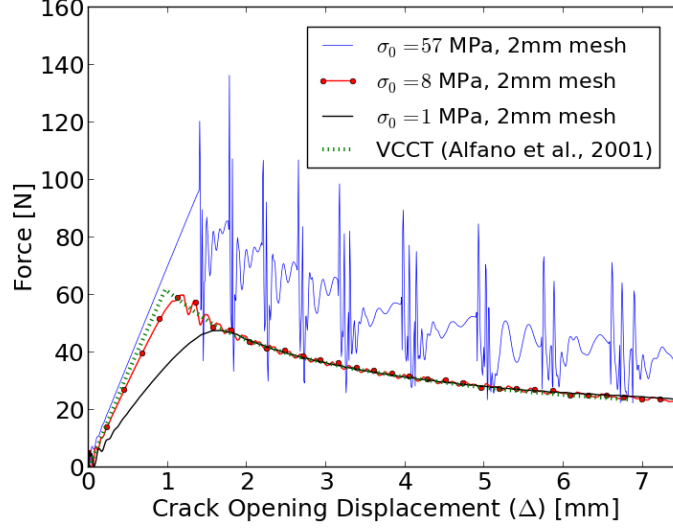
Figure 4.4: Force vs.crack opening displacement plot, obtained for a beam modeled using 2 mm mesh, and σ_{max} values of 57, 8 and 1 MPa.

solid cohesive elements located along the crack propagation path which is shown in Figure 4.4. Since the element size is too coarse with respect to the cohesive zone size, a maximum of two cohesive elements are in a loaded state at each time instant. Failure of these two elements results in a sudden load drop, which is the cause for the numerical noise shown in Figure 4.4 for the $\sigma_{max} = 57$ MPa loading case. Similar phenomena is also reported by Alfano and Crisfield [5], when this DCB problem was solved using $\sigma_{max} = 57$ MPa and 1 mm mesh.

Figure 4.7.a shows a typical state of the normalized traction stress in the cohesive elements, using $\sigma_{max} = 8$ MPa. It can be seen that the cohesive zone spans across approximately two elements along the crack propagation direction. Figure 4.7.b shows the normal traction stress in the first 10 cohesive elements, located along the crack propagation path. Since the cohesive zone size is sufficiently large, the normal traction load is shared between several cohesive elements at each time instant. During the dynamic crack propagation, as σ_{max} is reached at one cohesive element, followed by the cohesive softening phase, neighbouring cohesive elements which are still in the state of elastic loading, carry the load. This "load shifting" results in a
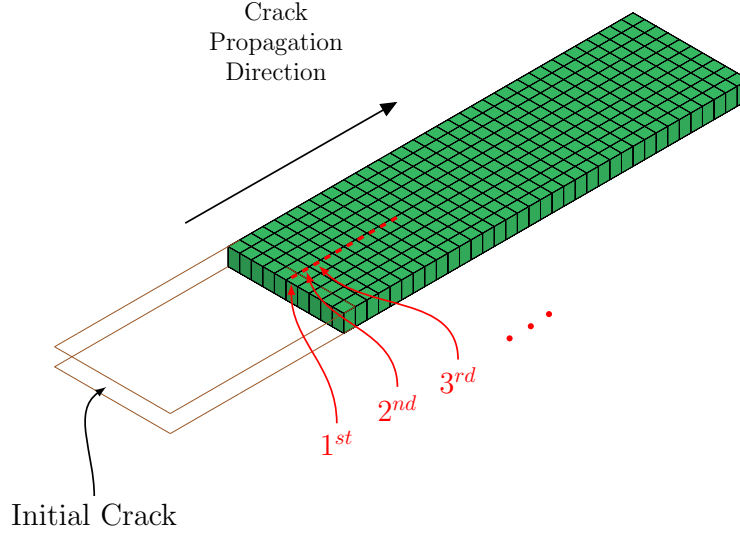
Figure 4.5: Isometric view of the DCB finite element model. The solid cohesive elements are shown in green color. A row of neighbouring cohesive elements located along the crack propagation path was used in order to investigate the cohesive behavior as the crack propagates. The results from this study appear in Figure 4.6, Figure 4.7 and Figure 4.8 for different σ_{max} values. The solid cohesive elements are numbered in an increasing order such that the 1st element is the element adjacent to the initial crack.

smoother force displacement curve and better prediction of the structural behavior, compared to the case where σ_{max} was set equal to 57 MPa.

Figure 4.8.a shows a typical state of the normalized traction stress in the cohesive elements, using $\sigma_{max} = 1$ MPa. It can be seen that the cohesive zone spans across approximately six elements along the crack propagation path. Figure 4.8.b shows the normal traction stress in the first 8 cohesive elements, located along the crack propagation direction. The extended length of the cohesive zone allows approximately six cohesive elements to be loaded simultaneously, a fact which yields a smooth load-displacement curve. However, the low value of the maximum traction stress results in increased compliance of the structure. It can be noticed from Figure 4.8.a that the effect of the cohesive zone extends approximately 32 mm ahead of the crack tip, which renders the value of $\sigma_{max} = 1$ MPa to be unrealistic. Similar behavior was reported by Alfano and Crisfield [5], when applying a

value of $\sigma_{max} = 1.7$ MPa to the problem. This important finding suggests that there is a limit to the amount of scaling that could be applied to σ_{max}, since, below a certain value, the stress distribution within cohesive interface diverges from the realistic stress distribution to an extent which makes the CZ method innaplicable to the problem.

Following the investigation process described above, a value of σ_{max} which is equal to 8 MPa was chosen when applying the LCZ method to the problem. This value allows obtaining a reasonable solution using a relatively coarse, 2 mm mesh, thus shortening the LS-DYNA and LCZ algorithm runtimes.

Ö£

(a)

(b)
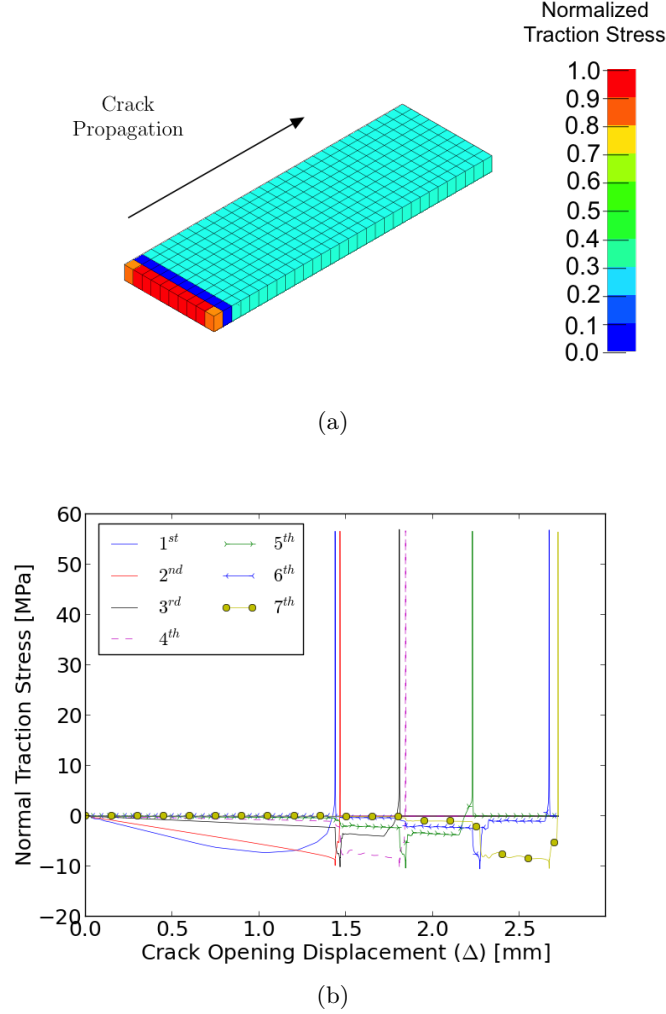
Figure 4.6: Typical cohesive behavior obtained for the DCB mode-I loading case, using a 2mm mesh size and $\sigma_{max} = 57$ MPa. **a).** Normalized out-of-plane traction stress within the cohesive interface. Only the cohesive elements are presented in this figure. **b).** Normal traction stress within a row of neighbouring cohesive elements located along the crack propagation path. The cohesive elements are located at the center of the cohesive interface width, and span along the beam's axial direction, with the first element being the first element loaded as the initial crack opens.

(a)

(b)
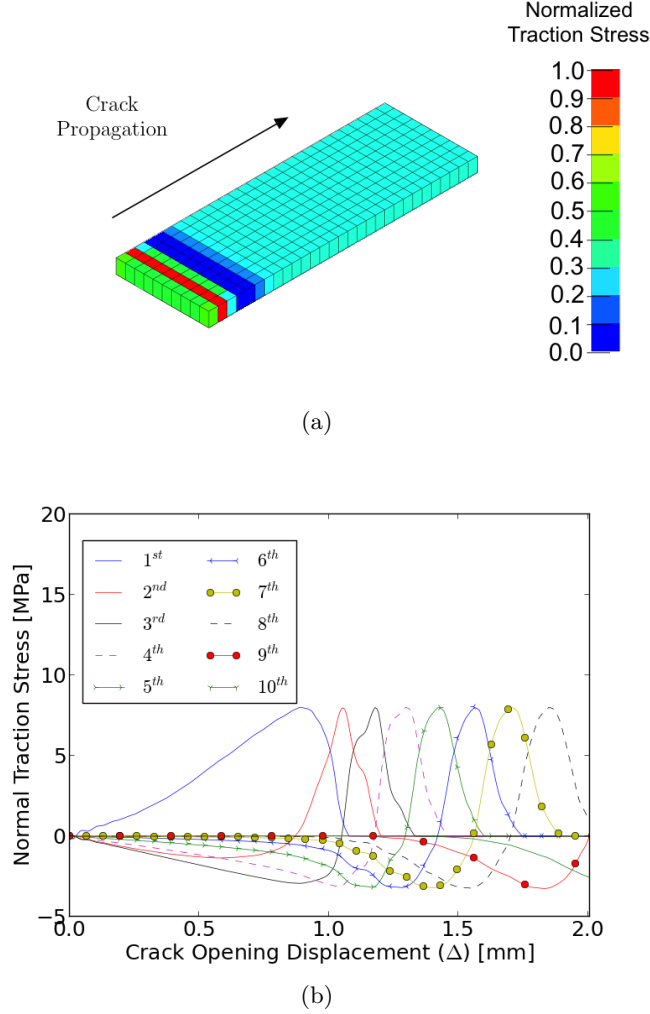
Figure 4.7: Typical cohesive behavior obtained for the DCB mode-I loading case, using a 2mm mesh size and $\sigma_{max} = 8$ MPa. **a).** Normalized out-of-plane traction stress within the cohesive interface. Only the cohesive elements are presented in this figure. **b).** Normal traction stress within a row of neighbouring cohesive elements located along the crack propagation path. The cohesive elements are located at the center of the cohesive interface width, and span along the beam's axial direction, with the first element being the first element loaded as the initial crack opens.

46

(a)

(b)
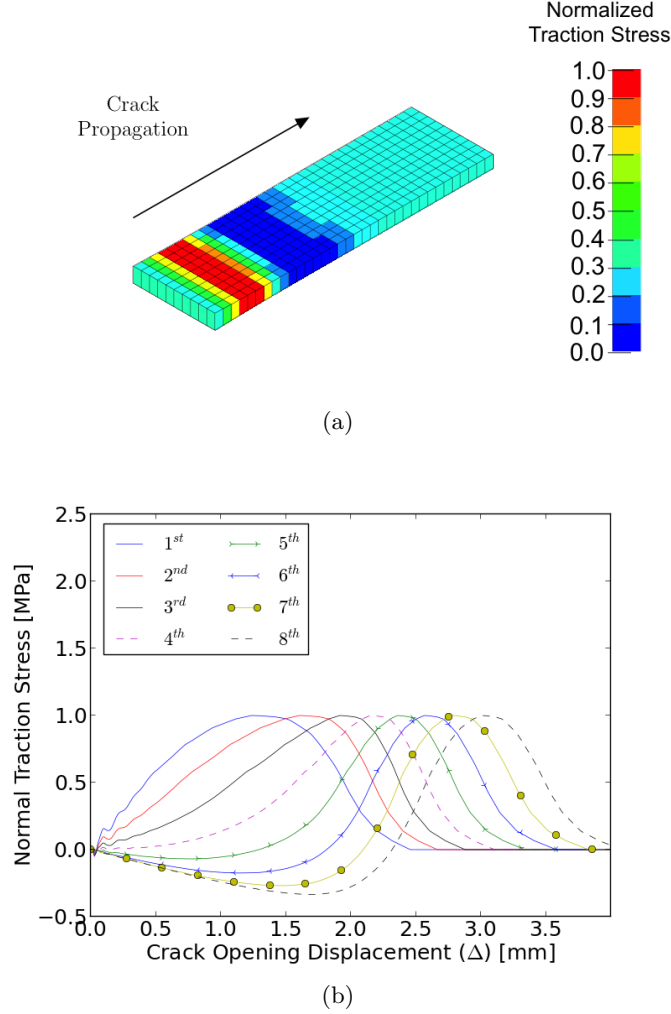
Figure 4.8: Typical cohesive behavior obtained for the DCB mode-I loading case, using a 2mm mesh size and $\sigma_{max} = 1$ MPa. **a).** Normalized out-of-plane traction stress within the cohesive interface. Only the cohesive elements are presented in this figure. **b).** Normal traction stress within a row of neighbouring cohesive elements located along the crack propagation path. The cohesive elements are located at the center of the cohesive interface width, and span along the beam's axial direction, with the first element being the first element loaded as the initial crack opens.

4.1.2   Applying the LCZ Method to the DCB Verification Problem

In order to apply the LCZ method for the solution of the DCB problem, the model was simulated using the following two configurations:

- **Case 1:** (Figure 4.3) A configuration similar to the model solved in Section 4.1.1, with the maximum traction stress, σ_{max} set equal to 8 MPa. The crack path was defined using a layer of solid cohesive elements, located along the interface layer of length $L - a$ along the beam. The LCZ algorithm **was not** used in this analysis. Thus, this case is identical to the conventional CZM, where the crack path is defined prior to the analysis.

- **Case 2:** (Figure 4.9) The beam was modelled using only *one layer* of thick-shell elements through its thickness, along the un-cracked section of the beam. Only the initial crack of length a was defined in the model. The cracked region was modelled using two layers of regular shell elements, each describing one surface of the cracked section. No cohesive elements are present in the model prior to the analysis, and the crack-growth path is not pre-defined. The LCZ algorithm was implemented to predict the delamination crack growth, and embed the local cohesive zones where and when needed. The splitting criterion for this case was defined as:

$$S = \sigma_{zz} \geq S_c \tag{4.2}$$

where S_c was set equal to 0.8 MPa (i.e. 10% of σ_{max} - the maximum stress of the cohesive interface) in order to allow early introduction of cohesive elements into the model before the out-of-plane stresses developed in the thick-shell elements become appreciable. The value of R was set equal to 12mm.

For both Cases 1 and 2, the in-plane dimensions of the thick-shell elements were 2mm×2mm. The analysis was carried out using LS-DYNA's explicit solver with a time step size of 8×10^{-5} ms.

The force vs. displacement results from the analysis of Cases 1 and 2, together with the VCCT model's prediction [5], are shown in Figure 4.10. Both the LCZ method and the conventional CZM results, are in good agreement with the results obtained in [5]. The curve corresponding to the

Figure 4.9: DCB test case 2. The beam is modelled using **one** layer of thick-shell elements, along the un-cracked section of the beam. No cohesive elements are pre-defined in the model. The LCZ algorithm was implemented to predict the crack growth.

LCZ method exhibits jaggedness due to the fact that the LCZ algorithm, in its present form, is not an integral part of LS-DYNA, thus resulting in numerical noise whenever element splitting takes place during the analysis. The evolution of the crack, and the migration of the cohesive-band for Case 2 where the LCZ algorithm is used, can be seen in Figure 3.12. The solid cohesive elements embedded in the model are presented using a darker shade.

Figure 4.10: DCB loading case (Mode-I delamination) - Reaction force at end of beam vs. crack opening displacement 2Δ. Results obtained using the conventional CZM (Case 1) vs. the LCZ algorithm prediction (Case 2), as well as the Virtual Crack Closure Technique predictions (Alfano and Crisfield [5]).

4.1.3 Mesh-Size Sensitivity

In order to investigate the effect of the mesh size on the results, the simulation performed in Case 2, was repeated using three different element sizes - 1, 2, and 4mm. The value of R was kept constant in these simulations, and was chosen to be 24mm, in order to be sufficient for the coarser element size. Figure 4.11 shows the force-displacement results for the various mesh sizes, compared to the VCCT results obtained in [5]. It can be seen that the LCZ method correctly captures the crack propagation in the structure, even for a relatively coarse mesh size of 4mm. However, the onset of delamination is somewhat under-predicted.
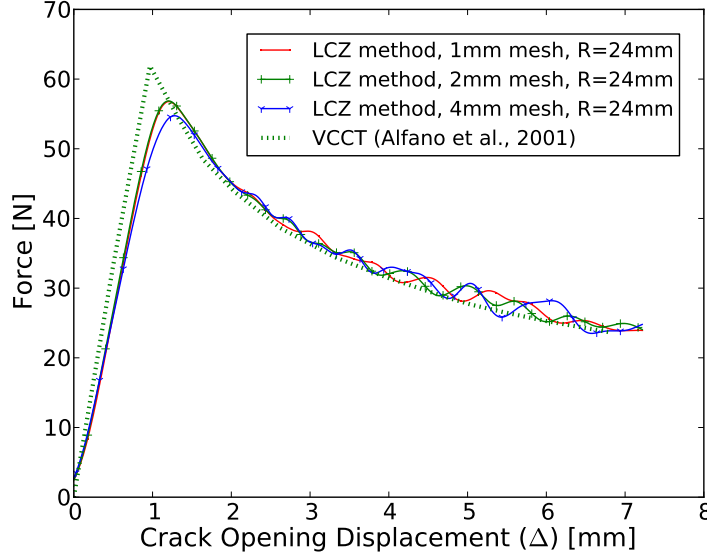
Figure 4.11: DCB loading case (Mode-I delamination) - Reaction force at end of beam vs. crack opening displacement Δ, for element sizes of 1, 2 and 4mm. In all cases $R = 24$mm. The results are compared to the Virtual Crack Closure Technique predictions (Alfano and Crisfield [5]).

4.1.4 R-Size Sensitivity

Using the LCZ method, the number of the cohesive elements in the model is directly linked to R. Since a lower number of cohesive elements in the finite element mesh will reduce the computational cost of the problem, an effort should be made to use smaller values of R, such that reliable results can still be obtained. Figures 4.12 and 4.13 show the results of solving the DCB problem, using a 1mm and 2mm mesh element size, together with varying R values, respectively. The results are compared to those obtained using the VCCT method ([5]). It can be seen that when R is equal to the element size, the results do not agree with the VCCT method. This is expected, since for the CZM to correctly capture the crack propagation in the material, the cohesive zone should span across a number of elements. Increasing R allows more cohesive elements to participate in the cohesive zone, thus obtaining a more reliable solution.

Figure 4.14 shows that fairly accurate results can be obtained when R
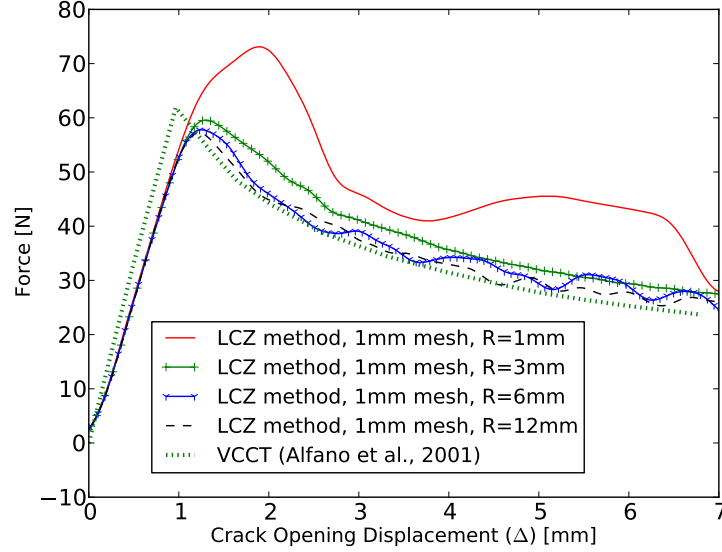
Figure 4.12: DCB loading case (Mode-I delamination) - Reaction force at end of beam vs. crack opening displacement Δ, for different values of R, and an element size of 1mm. The results are compared to the Virtual Crack Closure Technique predictions (Alfano and Crisfield [5]).

is set to a value which is 6 times the element size. In this figure, various element size models were tested, while keeping the ratio between R to the element size constant and equal to 6.

The geometrical effect of R on the obtained cohesive-band for 1mm mesh, using $R = 1$mm and $R = 6$mm is depicted in Figure 4.20(a) and Figure 4.20(b). It can be seen clearly that reducing the value of R will narrow the cohesive-band, and thereby reduce the number of cohesive elements present in the model.

4.1.5 Sensitivity to the Element Splitting Criterion

In order to investigate the effect of the splitting criterion on the results, the 2mm mesh sized DCB model was solved using varying S_c values. S was identical to the previous cases (σ_{zz}). The following equation was used to vary S_c:
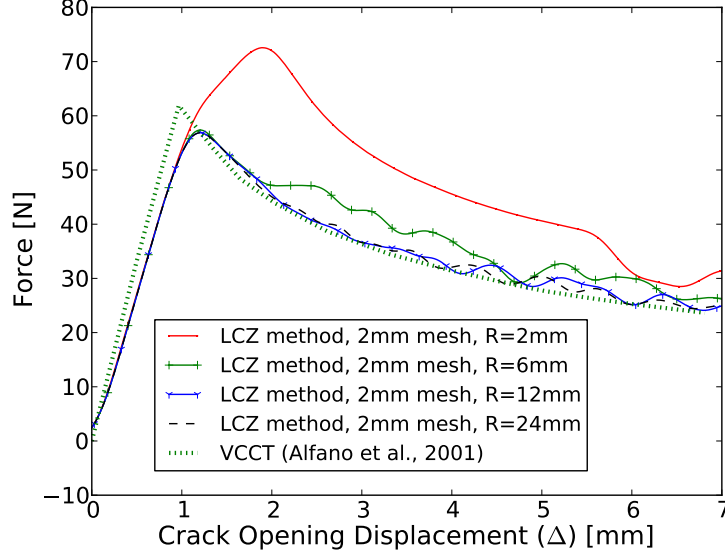
Figure 4.13: DCB loading case (Mode-I delamination) - Reaction force at end of beam vs. crack opening displacement 2Δ, for an element size of 2mm and different values of R. The results are compared to the Virtual Crack Closure Technique predictions (Alfano and Crisfield [5]).

$$S_c = threshold \times \sigma_{max} \qquad (4.3)$$

where *threshold* is a scale factor on the maximum stress value in the traction-separation law of the cohesive zone, σ_{max}. A range of values was used for this scaling factor. The results are shown in Figure 4.16. It can be seen that for higher values of this scaling factor, the obtained results exhibit some noticable load-drops, mainly around a crack opening of 1.8mm-3mm, compared to the VCCT solution. The reason for this can be seen in Figure 4.17, which shows the cohesive-band migration for a *threshold* value of 0.5, and $R = 12$mm. Figure 6.1(c) shows the state of the cohesive band at a certain point in time, where the crack has already some initial opening displacement. As the crack is being opened, the value of S in the structural elements adjacent to the cohesive-band front increases. Further splitting is not performed as S does not reach S_c. As the crack continues to open (Figure E.1(b)), further cohesive elements are deleted from the cohesive-band, after

53
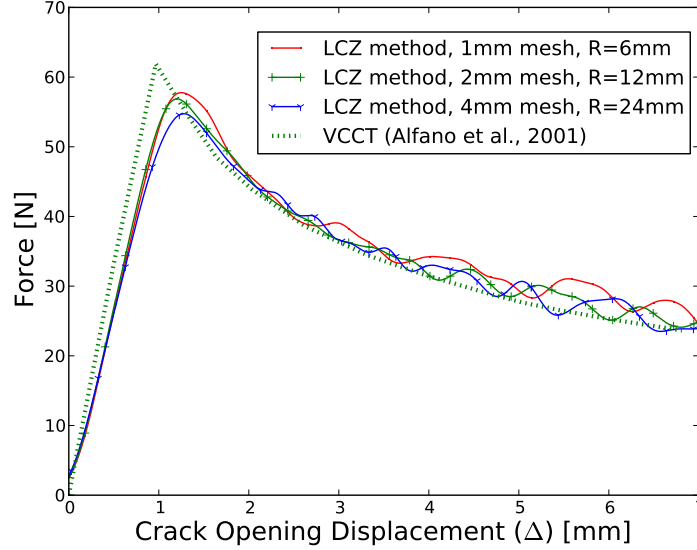
Figure 4.14: Force vs. crack opening displacement results for various element sizes used to simulate the DCB test case. R is set to be 6 times the element size. The results are compared to the Virtual Crack Closure Technique predictions (Alfano and Crisfield [5]).

having gone through their complete softening path in the traction-separation law. Only when one row of cohesive elements remains in the model, the value of S in the structural elements reaches S_c, and the next splitting operation is performed (Figure E.1(a)). Having only one row of cohesive elements in the model cannot capture the crack propagation correctly, since CZM requires a number of cohesive elements to be included across the cohesive zone. It is therefore important, when using the LCZ method, to choose R and S_c values such that sufficient number of cohesive elements will be included in the cohesive-band as the delamination crack propagates through the material.

4.1.6   Energy Balance

In order for the LCZ method to correctly capture the crack propagation, energy should be conserved during the element splitting process. Figure 4.18 shows the total internal (strain) energy in the structure for the DCB loading
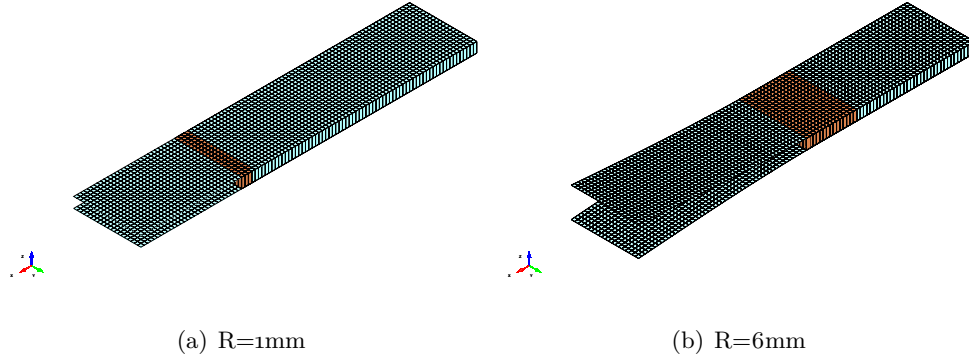
(a) R=1mm   (b) R=6mm

Figure 4.15: Typical cohesive band obtained for the DCB mode-I loading case, using a 1mm mesh size and varying R values. **a).** $R = 1$mm, **b).** $R = 6$mm.

cases (Cases 1 and 2). It can be seen that the strain energy in the model while using the LCZ method is slightly lower. This is due to the fact that the algorithm is currently not an internal part of the finite element solver (LS-DYNA), and the various operations performed by the code lead to some numerical errors. Nevertheless, the overall energy balance is encouraging, as the error in the internal energy prediction seems to be acceptable.
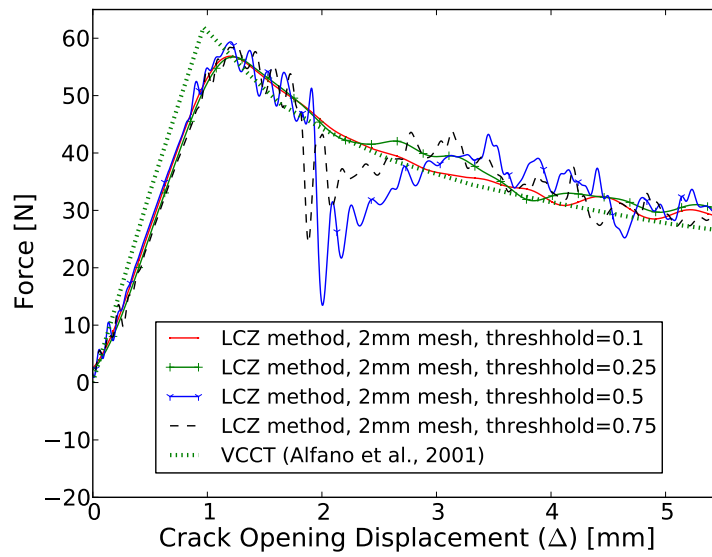
Figure 4.16: DCB loading case (Mode-I delamination) - Reaction force at end of beam vs. crack opening displacement Δ, for an element size of 2mm and different different *threshold* values. R=12mm. The results are compared to the Virtual Crack Closure Technique predictions (Alfano and Crisfield [5]).

(a)   (b)   (c)
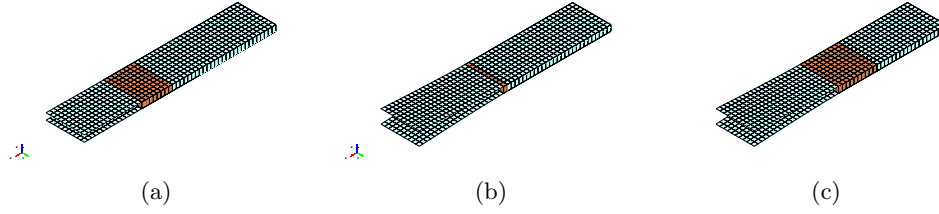
Figure 4.17: Cohesive-band migration obtained for the DCB loading case, using a 2mm mesh size and $threshold = 0.5$. **a).** The crack is being opened and the value of S in the structural elements adjacent to the cohesive-band front increases. Further splitting is not performed as S does not reach S_c. **b).** As the crack continues to open, further cohesive elements are deleted from the cohesive-band. **c).** Only when one layer of cohesive elements remains in the model, the value of S in the structural elements reaches S_c, and the next splitting operation is performed.
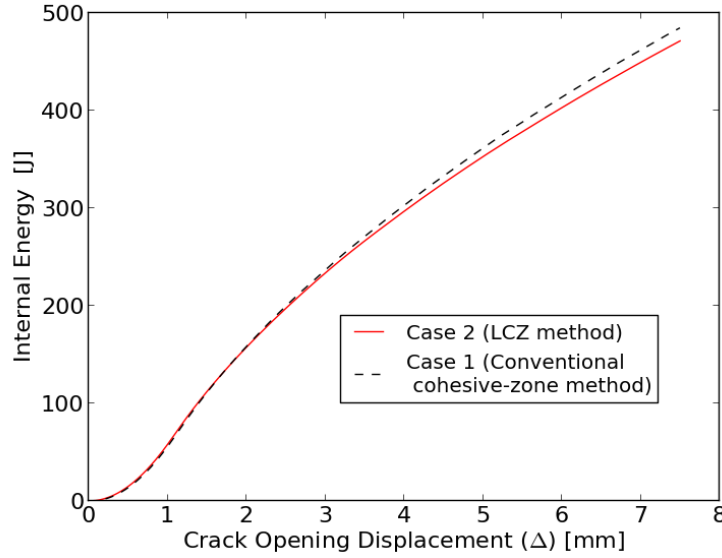
Figure 4.18: DCB loading case - sum of internal energies vs. crack opening displacement, for Case 1 (conventional CZM) and Case 2 (LCZ method).

4.2 Mode-II Delamination

To further verify the capabilities of the proposed method, a Mode-II loading case (Mi et al. [91]) was analyzed (Figure 4.19).

The example describes an End-Notch Flexure (ENF) test, and consists of a beam of total length $2L = 100$mm, thickness $h = 3$mm, and width of 1mm. A crack of an initial length $a = 30$mm is present in the beam. A specified displacement Δ, in the global negative z direction, is applied at the center of the beam. The material and cohesive interface parameters used in this ENF analysis can be found in Table 4.1.
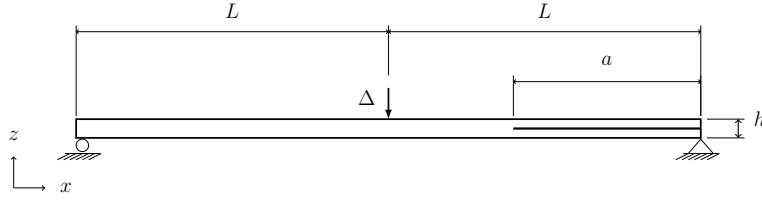
Figure 4.19: End Notch Flexure (ENF) test case, consists of a beam of total length $2L = 100$mm, thickness $h = 3$mm, and width of 1 mm. A crack of an initial length $a = 30$mm is present in the beam. A displacement Δ, in the global negative z direction, is applied at the center of the beam.

The beam was modelled using one thick-shell element through the thickness of the beam along the un-cracked section, and one element across its width. The element size along the axis of the beam was 1 mm. Figure 4.20 shows results from a preliminary analysis, performed in order to verify that the 1 mm element size is sufficient in terms of the cohesive zone length. Figure 4.20.a shows a fringe plot of the normalized shear traction stress within the cohesive elements. It can be seen from the figure that the cohesive zone spans across approximately 12 solid cohesive elements. Figure 4.20.b shows the shear traction stress vs. time within a row of neighbouring cohesive elements located along the crack propagation path. The first element is located 18 mm from the initial crack tip. It can be seen that the load is shared between several cohesive elements along the crack propagation path, which is required in order to correctly describe the crack propagation, and reduce the numerical noise of the numerical solution.

Similar to the Mode-I benchmark problem, the problem was solved using two modelling approaches: (i) the conventional modelling approach, i.e with cohesive elements existing along the delamination crack prior to the analysis ("Case 1"),and (ii) the LCZ method, where no cohesive elements were present in the model prior to the analysis ("Case 2").

Element splitting occurs in Case 2 when the following criterion is satisfied:

$$S = \tau_{zx} \geq S_c \tag{4.4}$$

$$S_c = 0.1 \times \tau_{max} \tag{4.5}$$

where the value of τ_{max} was set to 57.0 MPa. The value of R was set equal to 6mm. LS-DYNA's explicit solver was used for obtaining the solution, using a time step size of 1.7×10^{-5} ms.

Figure 4.21 shows the obtained reaction force at the loading point, vs. the z-displacement (Δ), for the LCZ algorithm prediction (Case 2), as well as the conventional CZM (Case 1). Numerical results obtained by Mi et al. [91], Liu et al. [77], and the analytical model results (Mi et al. [91]) are shown as well. Reasonable agreement between the LCZ algorithm and other results is obtained. The visible noise present in the results obtained using the LCZ algorithm is due to the fact that the algorithm is not a built-in feature of the finite element solver, and the various numerical operations performed by the algorithm on the finite element mesh lead to some numerical noise. Nevertheless, the algorithm is still able to represent the essence of the mechanical behavior correctly.
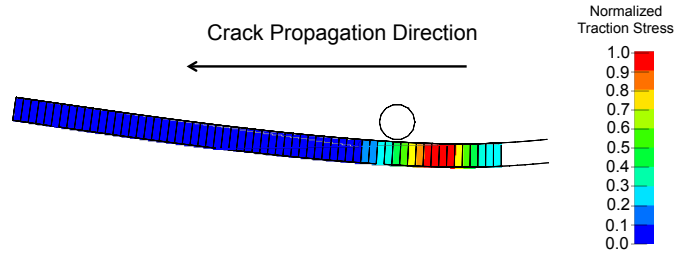
(a)
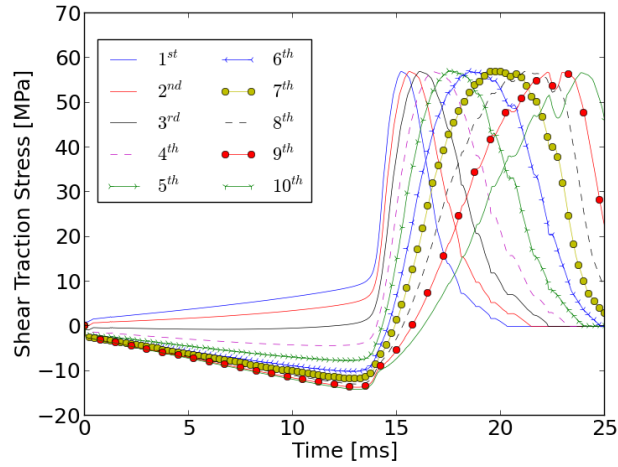
(b)

Figure 4.20: Typical cohesive behavior obtained for the ENF mode-II loading case, using a 1mm mesh size and $\sigma_{max} = 57$ MPa. **a).** Normalized shear traction stress within the cohesive interface. **b).** Shear traction stress within a row of neighbouring cohesive elements located along the crack propagation path. The first element is located 18 mm from the initial crack tip.
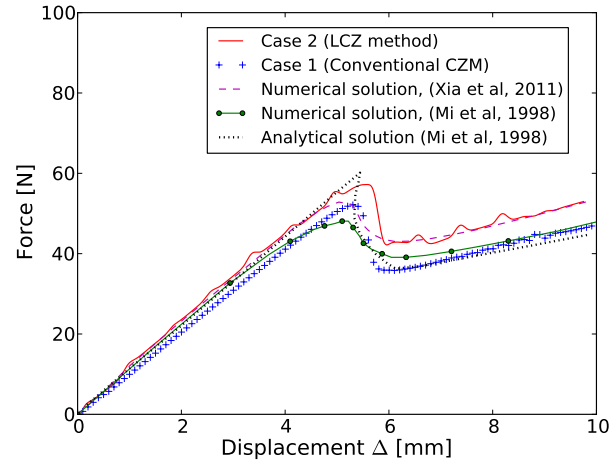
Figure 4.21: ENF loading case (Mode-II delamination) - Reaction force at loading point vs. z-displacement. The LCZ algorithm prediction is presented vs. numerical results obtained by Mi et al. [91], Liu et al. [77], and the analytical model (Mi et al. [91]).

4.3 Mixed-Mode Delamination

A mixed-mode-bending (MMB) (Mi et al. [91]) was modelled using the LCZ algorithm (Figure 4.22). The loading case consists of a beam of total length $2L = 100$mm, thickness $h = 3$mm, and width of 1mm. A crack of an initial length $a = 30$mm is present in the beam. A loading lever is placed above the beam and is attached to the beam's tip via a pivot connection. A rolling mechanism allows sliding of the loading lever at its point of interaction with the center of the beam.

A displacement constraint in the global negative z direction, is applied at the the loading lever at a point which is at a distance $c = 42$mm from the beam's center. The deflection Δ and the reaction force P at the end of the beam are monitored during the run. This loading setup results in a mixed mode ratio $G_I/G_{II} = 0.909$. The loading lever is modelled as a rigid part. The material and cohesive interface parameters used in this analysis can be found in Table 4.1. Element splitting occurs when the following criterion is satisfied:

$$\frac{S}{S_c} = \sqrt{\left(\frac{\sigma_z}{\sigma_{max}}\right)^2 + \left(\frac{\tau_{zx}}{\tau_{max}}\right)^2} \geq threshold \qquad (4.6)$$

The value of *threshold* was set equal to 0.1 to allow seeding the cohesive elements into the model early enough before significant out-of-plane normal and shear stresses develop within the thick-shell elements. The value of R was set equal to 15mm.

The beam was modelled using one thick-shell element through the thickness of the beam along the un-cracked section, and one element across its width. Offset-shell elements were used to model the initially cracked section of the beam. The element size along the axis of the beam was 0.25mm, fine enough to allow several cohesive elements to span across the cohesive zone. It was found that using a coarser mesh for this loading case, caused an unrealistic sliding of the roller along the beam, due to the coarse mesh size that did not allow the roller to roll smoothly along the beam's surface. The analysis was carried out using LS-DYNA's explicit solver with a time step size of 4.6×10^{-6} ms.

Similar to the Mode-I and Mode-II benchmark problems, two different model configurations were investigated: Case 1, where cohesive elements existed along the delamination crack prior to the analysis, and Case 2, where

the LCZ method was applied, and no cohesive elements were present in the model prior to the analysis.
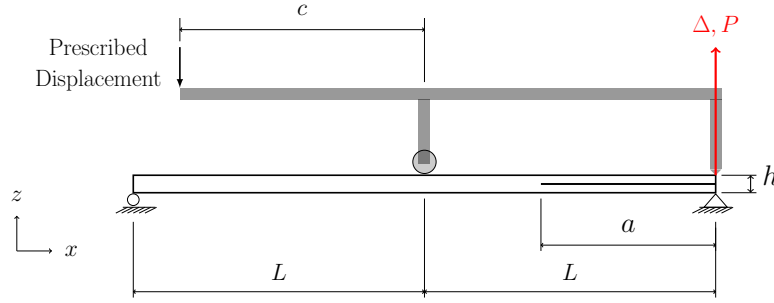
Figure 4.22: Mixed Mode Bending (MMB) test case. The loading case consists of a beam of total length $2L = 100$mm, thickness $h = 3$mm, and width of 1mm. A crack of an initial length $a = 30$mm is present in the beam. A displacement constraint Δ, in the global negative z direction, is applied at the loading lever at a point which is at a distance $c = 42$mm from the beam's center.

Figure 4.23 shows the beam's deformed geometry during the loading process, while Figure 4.24 shows the obtained reaction force at the beam's end (P), vs. the beam's end displacement in the global z direction (Δ), using the LCZ algorithm (Case 2) as well as the conventional CZM (Case 1). The numerical and analytical solutions obtained by Mi et al. [91] are also superposed on the graph for comparison. While the LCZ method leads to a more jagged response during the pre-peak regime of loading (attributed to the fact that it is not a built-in feature of LS-DYNA), the predicted curve is in reasonable agreement with those obtained using the conventional CZM (Case 1) and the various solutions by Mi et al. [91].

4.4 Summary and Conclusions

In this chapter, the LCZ method was applied to pure delamination crack propagation under mode I, mode II, and mixed mode loading scenarios. The results were compared to analytical results, as well as to results obtained using other numerical methods.
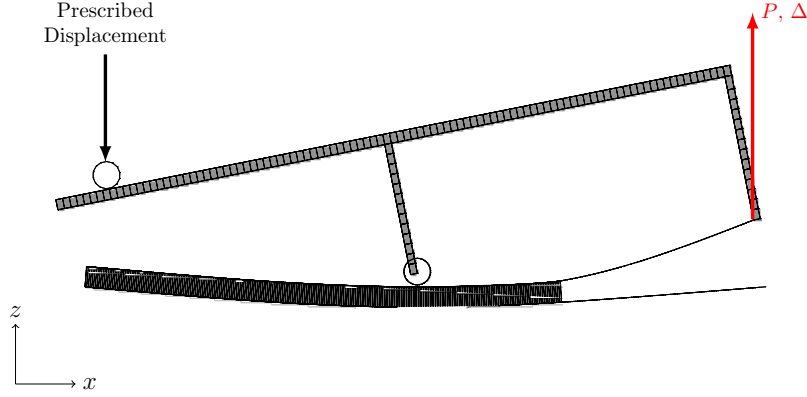
Figure 4.23: Mixed Mode Bending (MMB) test case finite element model during the loading process. The load at the end of the beam (P) vs. the beam's end displacement (Δ) is shown in Figure 4.24.

For the mode I loading scenario, good agreement was obtained between the force vs. displacement profile obtained using the LCZ method and the VCCT method. Mesh sensitivity analysis shoed little influence on the results, for the range of element size tested. For all mesh size tested, the maximum force predicted was slightly lower (5%-8%) than the maximum force predicted by the VCCT method. A slight decrease in the maximum load was noticed for the 4mm element size, which is an expected outcome for the CZM, which shows a decrees in the maximum load with increased element size.

For the numerical case under investigation, a value of R which was set equal to at least 6 times the element size, was required in order to obtain reliable results, and the threshold value should be small enough with respect to the maximum load of the traction-separation law. These findings are expected, otherwise, the resulting cohesive band does not span across a minimum number of cohesive elements required in order to obtain reliable results from the CZM.

Reasonable results were obtained for the mode-II and mixed-mode problems solved using the LCZ method. Owing to the fact that the algorithm is currently not an internal part of the finite element solver (LS-DYNA) used in this study, the various numerical operations performed by the algorithm on the finite element mesh lead to some numerical noise. The limited element formulations that are currently available in LS-DYNA pose some challenges
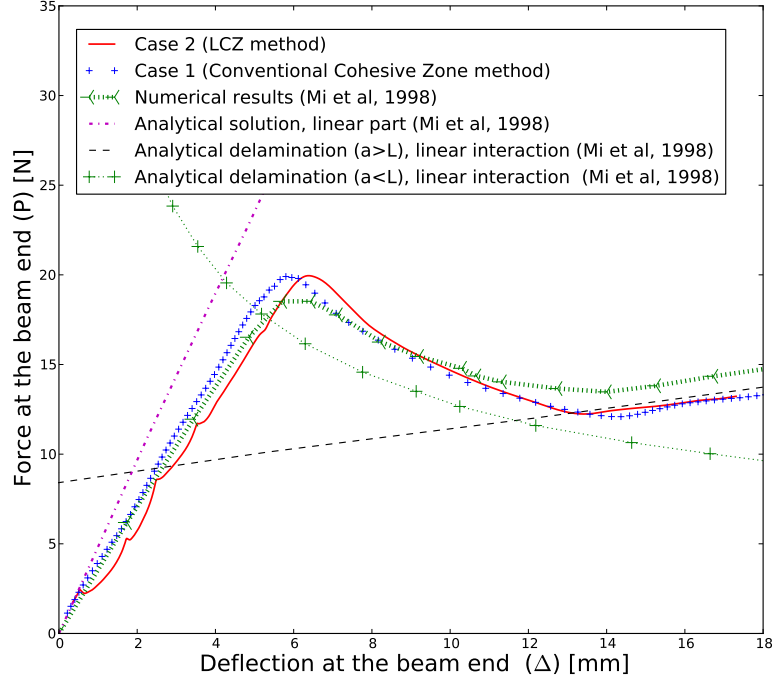
Figure 4.24: MMB loading case (Mixed-Mode delamination) - Reaction force at end of beam, P, vs. vertical deflection at the beam end, Δ. The LCZ algorithm prediction is shown in comparison to the results obtained using the conventional CZM as well as the analytical results obtained by Mi et al. [91].

in achieving full compatibility between the offset-shell elements (in the split region) and the thick-shell elements (in the unsplit region) of the mesh. In the current LCZ method this difficulty is overcome by introducing narrow regions of overlapping shell elements in the transition region. Nevertheless, the algorithm is able to capture the delamination crack propagation correctly. It is expected that further improvements in speed and accuracy of the computations will be attained once the algorithm is embedded within the finite element solver, and a layered thick-shell formulation with rotational nodal degrees of freedom is implemented in LS-DYNA. This would

allow a smoother connectivity between the split and neighbouring unsplit regions of the mesh.

Chapter 5

Validation

Following the verification process, which was described in Chapter 4, this chapter describes the validation process performed to the LCZ method. Validation of a numerical code is often referred to as the procedure taken in order to establish its legitimacy, i.e its ability to correctly represent the physics of the problem it intends to solve. Here, the LCZ method was validated by its application to loading cases combining delamination crack propagation together with intralaminar damage growth. Section 5.1 will describe its application to static loading of a double-notched coupon, Section 5.2 will describe its application to a dynamic tube crushing loading case, and Section 5.3 will describe its application to a dynamic plate-impact event.

5.1   Tensile Loading of a Notched Coupon

In order to test the LCZ method capability to predict delamination combined with in-plane damage growth, a simple double-notched tensile experiment was chosen as a benchmark problem. A brief description of the experiment is brought bellow, followed by the description of the numerical model. The results obtained by applying the LCZ method for the simulation of the experiment are presented thereafter.

5.1.1   Material and Test Specification

A $[90/0]_s$ Hexcel E-glass/913 double-notched tensile coupon, was experimentally loaded to complete failure by Hallett and Wisnom [48]. The test-specimens were prepared using 0.125mm thick pre-preg tapes cured in an autoclave, resulting in a nominal specimen thickness of 0.5 mm. The specimen, shown in Figure 5.1, had a length of 200 mm, where a region having length $L_2 = 50$ mm was clamped at each end of the specimen to an Instron universal tensile machine, resulting in an effective tensile length of 100 mm (L_1). Two symmetric notches, cut from the specimen at its center, resulted in a narrow region a, 10 mm in width.

The elastic material sublaminate parameters, are brought in Table 5.1.

Table 5.1: Elastic Hexcel E-glass/913 material properties

Parameter	Unit	Value	Source
Density (ρ)	(g/mm^3)	1.97E-3	[20]
Longitudinal Modulus (E_{11})	GPa	43.9	[46]
Transverse Modulus (E_{22})	GPa	15.4	[46]
Transverse Modulus (E_{33})	GPa	15.4	[46]
Minor Poisson's ratio (ν_{21})	(-)	0.11	[46]
Minor Poisson's ratio (ν_{31})	(-)	0.11	[46]
Transverse Poisson's ratio (ν_{32})	(-)	0.3	[46]
Shear Modulus (G_{12})	GPa	4.34	[46]
Shear Modulus (G_{23})	GPa	4.34	[46]
Shear Modulus (G_{31})	GPa	4.34	[46]

The experimental results are described in detail in [48]. In all specimens tested, damage initiated at the notch tip. Transverse cracks in the 0° ply grew simultaneously with transverse cracks along the 90° ply. Triangular shaped delamination grew along the 90/0 interface as the plies continued to split. Complete failure of the specimen occurred at the ultimate load due to the final failure of the 0° fibers. Fibers closer to the notch tip failed first, and subsequent failure of fibers quickly followed with a sudden drop in the load-carying capability of the specimen.
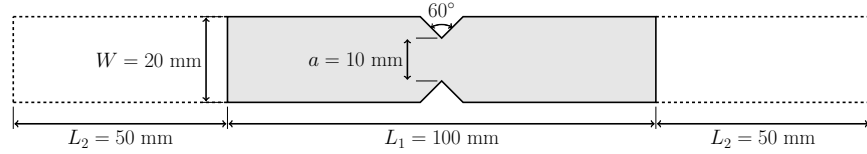
Figure 5.1: A double-notched $[90/0]_s$ Hexcel E-glass/913 test coupon geometry used in the tensile experiments performed by Hallett and Wisnom [48]. This experiment was used as a benchmark problem to test the capability of the LCZ algorithm to simulate delamination combined with in-plane damage growth.

5.1.2   Finite Element Model

The finite element model of the coupon is shown in Figure 5.2. Three planes of symmetry exist in the model - yz, xz and xy planes. Thus, it is sufficient to model 1/8 of the coupon in order to correctly capture its behavior during the tensile experiment. The darker shaded region in Figure 5.2.**a**, which is bounded by the zy and xz planes, resembles 1/4 of the test coupon. The actual finite-element model was further simplified, taking into account the symmetry of the xy plane, allowing the specimen to be modelled using a *single* through-thickness layer of LS-DYNA's thick-shell elements, each element representing two material plies - a single 0° ply, as well as a single 90° ply. This was achieved by taking advantage of LS-DYNA's *PART COMPOSITE keyword, which allows multiple material models and material directions to be assigned to a single element. Each of the thick-shell elements contained 8 through-thickness integration points, to which separate material angles were assigned, defining the appropriate material orientations through the thickness of the element (Figure 5.2.**c** and Figure 5.2.**d**). In their work, Hallett and Wisnom [46] showed the importance of introducing discrete elements within the plies, to capture the correct stress distribution during the failure process, and to allow discrete failure modes which were also found in the experiments. A similar approach was used here, where two sets of LS-DYNA's discrete beam elements were used to model the in-plane matrix splitting cracks. One set of beams was used to model the matrix splitting cracks along the 0° fiber direction within the 0° ply (Figure 5.2.**(c.2)**), and a second set of beam elements was used to model the matrix splitting cracks along the 90° fibers direction within the 90° ply (Figure 5.2.**(c.3)**). It is important to note that the nodes of the thick-shell elements bounding the splitting cracks were artificially displaced in order to create this figure and visualize the beam elements, as the discrete beam elements have a zero initial length at $t = 0$, and could not be visualized otherwise.

A closer isometric view at the crack tip, showing the connectivity of the thick-shell elements to the discrete beams, is shown in Figure 5.2.**d**. Similar to Figure 5.2.**c**, the nodes of the thick-shell elements bounding the splitting cracks were artificially displaced in order to visualize the discrete beam elements in this figure.

The elements edge length in the in-plane direction is approximately 0.2 mm long. Appropriate boundary conditions were applied to all nodes which lie on one of the symmetry planes, and displacement constraint was prescribed to the end of the coupon, where the load was applied by the Instron

machine clamps. The model was solved using the explicit numerical solver of LS-DYNA, and care was taken to ensure that the load was applied at a rate which allows a numerical solution within a reasonable amount of time, yet will ensure that the inertia effects on the results were negligible. The finite element model, at $t = 0$, contained $12,685$ thick shell elements and 245 discrete beam elements. When applying the LCZ algorithm to solve the problem, it is expected that the thick-shell elements will adaptively split as cohesive elements will be seeded within the coupon, and delamination could thus propagate in the coupon as the splitting cracks grow in the in-plane dimension.
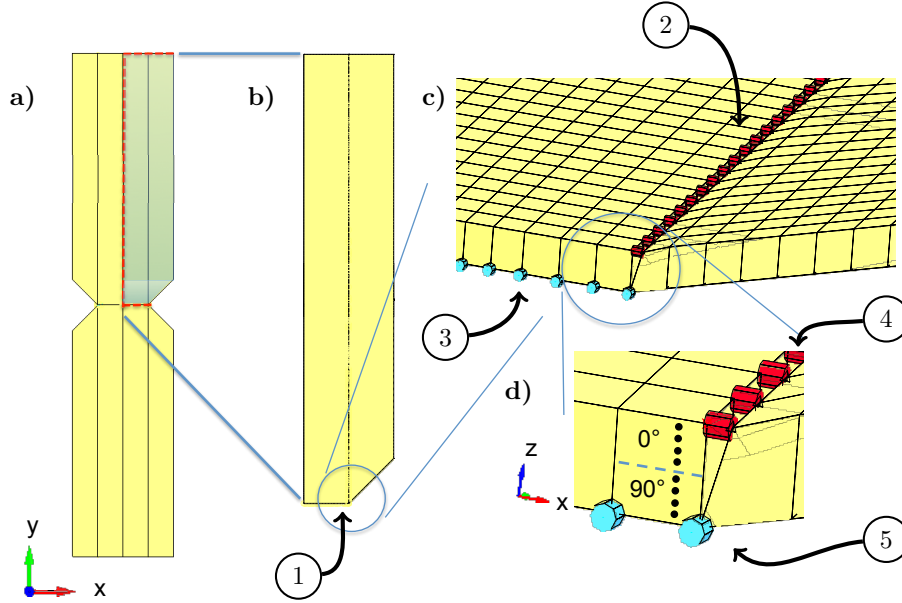
Figure 5.2: Finite element model used for solving the double-notch $[90/0]_s$ specimen under tensile loading condition, simulated using the LCZ algorithm. **a).** Front view of a the unclamped section of the test coupon. **b).** Only 1/8 of the test coupon was modeled, taking advantage of the coupon and the ply orientation symmetry. **c).** A closer isometric view of the crack tip. The specimen was modelled using a *single* through-thickness layer of LS-DYNA's thick-shell elements. Discrete beam elements were used to model the in-plane splitting cracks - where one set of beams was used to model the splits in the 0° ply **(2)**, and a second set of beams was used to model the splitting cracks in the 90° ply **(3)**. The nodes of the thick-shell elements bounding the splitting cracks were artificially displaced in order to create this figure, and visualize the beam elements, which have zero initial length in the actual model at $t = 0$. **d).** A closer isometric view of the crack tip, showing the connectivity of the thick-shell element to the discrete beams. Here, too, the nodes of the elements bounding the splitting cracks were artificially displaced in order to create this figure, and visualize the beam elements. Each of the thick-shell elements contained 8 through-thickness integration points, to which separate material angles were assigned. The elements edges which lie within the xy plane are approximately 0.2 mm in length.

5.1.3 Intralaminar Damage Modelling

Two of LS-DYNA's built-in material models were simultaneously used during the analysis - ∗MAT ENHANCED COMPOSITE DAMAGE (∗MAT 54) to model the homogenized damage in the continuum elements, and ∗MAT GENERAL NONLINEAR 6DOF DISCRETE BEAM (∗MAT 119) to model the discrete damage within the in-plane direction. When applied to thick-shells, ∗MAT ENHANCED COMPOSITE DAMAGE material behaves as an elastic, *perfectly plastic* orthotropic material. Maximum stress for each direction of loading can be defined, as well as the failure strain for each mode of loading.

Hallett and Wisnom [46] reported that during the experiments, a transverse crack density of approximately 30 cracks/cm was measured in the 90° ply. In order to compensate for the influence of these cracks on the overall stiffness reduction of this ply , the Young's modulus of the 90° ply was reduced by 50% in the transverse direction *only*. This was backed by analysis made by Kashtalyan and Soutis [63]. Similar reduction factor was used here for the Young's modulus of the 90° ply in the transverse direction.

Table 5.1 and Table 5.2 summarize the elastic and damage properties used during the analysis, respectively, for the 0° and 90° material directions. The LS-DYNA material cards used in the analysis for the 0° and 90° plies, appear in Appendix D, Program D.1 and Program D.2, for the 0° and 90° material directions, respectively.

The strain-to-failure values for each mode of loading, were chosen such that based on the element size used in the analysis, realistic fracture energy values would be obtained. Thus, failure strain values of 0.14 was chosen for the transverse (matrix) loading direction in tension, yielding a fracture energy of 1 kJ/m², 0.5 for transverse shear (yielding a fracture energy of 7.7 kJ/m²) , and 0.1 for the axial direction, in tension (yielding a fracture energy of 19.83 kJ/m²).

In order to capture the discrete nature of the in-plane splitting, discrete beam elements were used (∗ELEMENT BEAM THICKNESS), to which ∗MAT GENERAL NONLINEAR 6DOF DISCRETE BEAM was assigned. This material model allows arbitrary force vs. displacement curves to be defined for the axial as well as the transverse loading directions of the beam, thus, traction-separation curves can be defined, resulting in a "cohesive-like" behavior of the elements. Hallett and Wisnom [46] used a user-defined cohesive material model, to which the strain energy release rate values of the material for mode-I and mode-II loading directions (G_{Ic} and G_{IIc}) were input directly. Since ∗MAT GENERAL NONLINEAR 6DOF DISCRETE

BEAM does not support the use of these values directly, traction-separation curves were to be used instead. Load-curves that yield the appropriate strain energy release rate for the material were applied, and a simple finite element models was used in order to verify this transition, where the behavior of the discrete beams to which *MAT GENERAL NONLINEAR 6DOF DISCRETE BEAM was compared to the behavior of standard solid cohesive elements modelled using *MAT COHESIVE GENERAL. Figure 5.3 shows the finite element model used for calibrating the discrete beam material model, and Figure 5.5 shows the stress vs. strain plots obtained in the cohesive interface during axial loading of the interface, using both modelling approaches. It can be noted that both modelling approaches yield similar results, as well as similar strain-energy release rate values.
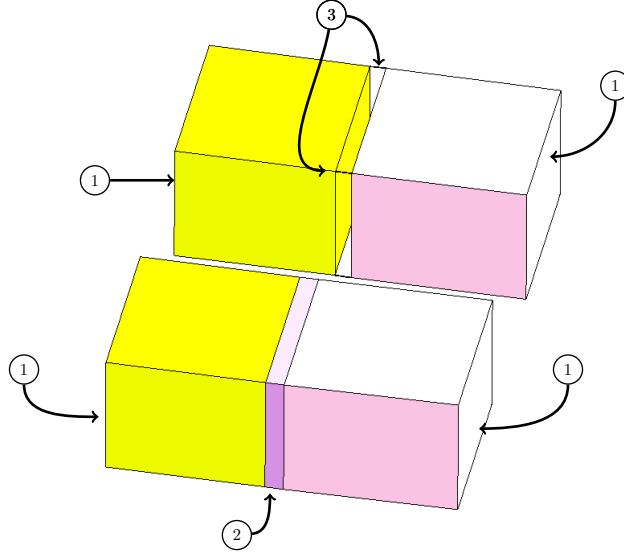
Figure 5.3: Typical finite-element model used to calibrate the discrete cohesive element material model. **1.** Thick shell elements to which cohesive elements were connected and were displaced using a prescribed displacement constraint. **2.** Solid cohesive element to which *MAT COHESIV GENERAL was assigned. **3.** Discrete beam elements in which *MAT GENERAL NONLINEAR 6DOF DISCRETE BEAM was used.
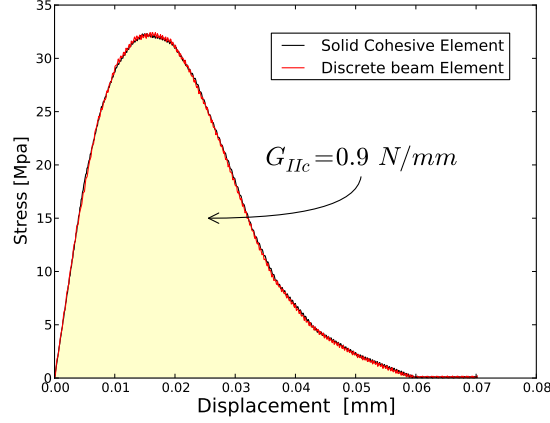
Figure 5.4: Typical stress vs. displacement obtained using the finite element model in Figure 5.3. In this case, the solid cohesive element and the discrete beam elements were loaded in shear. The obtained strain energy release rate for both configurations (G_{IIc}) is 0.9 N/mm or kJ/m^2).

Table 5.3summarizes the cohesive properties assigned to the discrete beam elements for mode-I and mode-II loading directions. The critical strain energy release rate values are taken from Hallett and Wisnom [46], where the maximum normal and shear stress values were adjusted to allow damage to accumulate within the discrete elements. Choosing higher values for the normal and shear stresses did not allow the discrete elements to deform in a manner that correctly distributed the stress within the coupon.

5.1.4 Interlaminar Damage Modelling

For interlaminar damage modelling, the LCZ method was applied. This allowed the finite element model to include no cohesive interface for the through-thickness direction prior to the analysis. The following mixed-mode element splitting criterion was used in order to trigger through-thickness element splitting and adaptive insertion of solid cohesive elements into the model:

$$S = \sqrt{\left(\frac{\sigma_z}{\sigma_{max}}\right)^2 + \left(\frac{\tau_{zx}}{\tau_{max}}\right)^2} \geq S_c \qquad (5.1)$$

where σ_{max} was defined as 50 Mpa, and τ_{max} was defined as 25 Mpa.

A critical value $S_c = 0.6$ was chosen. It is important to note that the values of the parameters related to the element splitting criterion has little physical meaning, as they merely serve as a flag to seed the cohesive elements when the potential for delamination exist.

LS-DYNA's *MAT COHESIVE GENERAL material model was assigned to the solid-cohesive elements (8-noded solid elements (*ELEMENT SOLID, ELFORM=19) inserted during the analysis, in order to capture the interface failure.

The interlaminar cohesive properties used in the analysis are listed in Table Table 5.3. It can be noted that although the fracture energy values used for the mode-I and mode-II intralaminar cohesive model are identical to the values used in the interlaminar cohesive model, the maximum stress values for both normal and shear direction are different. It was found that using values similar to the values used for the interlaminar cohesive interfaces resulted in unreliable results, even when the conventional application of the CZM was used to model the intralaminar damage.

The radial distance R used by the LCZ algorithm was set to $1mm$, which is approximately 5 times the in-plane element size used in the analysis.

Table 5.2: LS-DYNA's *MAT 54 Material model damage parameters used in the $[90/0]_s$ double-notched coupon simulation

Parameter	Unit	Value	*MAT 54 variable
Maximum stress in the axial direction, under compression [a] (σ_{1c}^f)	MPa	620	xt
Maximum stress in the axial direction, under tension [a] (σ_{1t}^f)	MPa	1140	xt
Maximum stress in the transverse direction, under compression [a] (σ_{2c}^f)	MPa	128	yc
Maximum stress in the transverse direction, under tension [a] (σ_{2t}^f)	MPa	39	yt
Maximum in-plane shear stress (τ^f) [a]	MPa	80	sc
Maximum strain for matrix straining in tension or compression (ε_2^f)	(-)	0.14	dfailm
Maximum in-plane shear strain (ε_{shear}^f)	(-)	0.5	dfails
Maximum strain for fiber tension $(\varepsilon_{1t}^f$	(-)	0.1	dfailt

[a] Source: [20].
[b] Source: [91]

Table 5.3: Cohesive properties used in the $[90/0]_s$ double-notched coupon simulation

Intralaminar damage (In-plane discrete cohesive elements)				
Parameter	σ_{max}	τ_{max}	G_{Ic}	G_{IIc}
Unit	MPa	MPa	N/mm	N/mm
	33	33	0.25	0.9
Interlaminar damage (Solid cohesive elements created by the LCZ algorithm)				
Parameter	σ_{max}	τ_{max}	G_{Ic}	G_{IIc}
Unit	MPa	MPa	N/mm	N/mm
	50	25	0.25	0.9

Results and discussion

Figure 5.5 shows the resulting force vs. displacement curve obtained during the run, as well as typical cohesive bands created as the loading of the coupon increases. The noticeable noise in the loading curve obtained during the simulation is due to the fact that the LCZ algorithm is not integrated into LS-DYNA, and the frequent external interaction of the LCZ algorithm with the finite element solver introduces some numerical noise into the results. Nevertheless, the simulation is able to predict the maximum load before failure and the displacement at failure with good accuracy.

As the specimen is loaded and the load is further increased, the *zx* component of the shear stress (out-of-plane shear stress) within the thick-shell elements located at the notch-tip is increased to levels which cause the element-splitting criteria to be satisfied. Adaptive insertion of cohesive elements is then automatically performed, as can be seen in Figure 5.5, for a crack-opening displacement of approximately 0.1mm. As the loading further increases, beam elements across the splitting interfaces deform. Cohesive elements are seeded along the edges of the splitting cracks, as well as across the free edges of the coupon.

Figure 5.6 shows the experimentally and numerically obtained damage pattern, at 25.8% of the maximum load. A still image from the experiment [48] is shown in Figure 5.6.a. Small matrix cracks begin to develop at the notch tip, in both 0° and 90° plies. Figure 5.6.b and Figure 5.6.c, shows the LCZ algorithm damage prediction for the matrix cracks at the 90° and 0° ply, respectively, where red color indicates fully damaged material in the transverse direction, and blue color indicates undamaged material.

As the load increases, the matrix damage, which originally originated at the notch tip, spreads across the coupon, in both 0° and 90° plies. Figure 5.7 shows the experimentally and numerically obtained delamination damage, at the vicinity of the notch at the maximum load before failure. Figure 5.7.a shows the delamination pattern predicted by the LCZ algorithm, at the 0°/90° interface. Figure 5.7.b shows the experimental results from [48]. The predicted delamination pattern follows a somewhat narrow triangular shape, which emerges from the notch tip and spreads along the 0° fiber direction. Further increasing the load causes the stress at the 0° fibers to increase beyond their load bearing capacity, and the fibers fail almost instantaneously across the coupon, which leads to a total failure of the specimen.
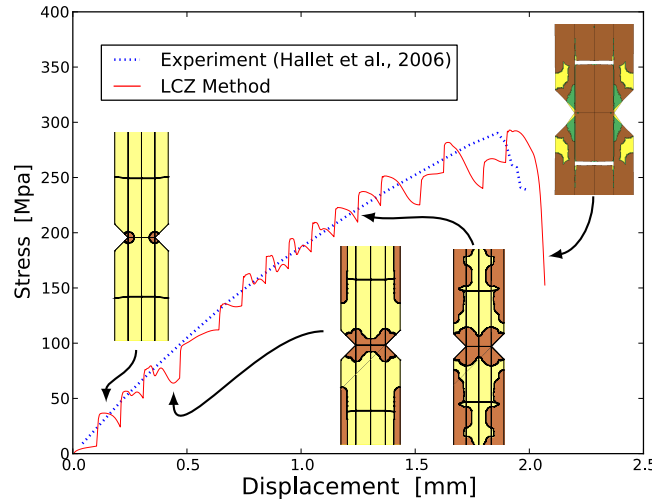
Figure 5.5: Far stress vs. displacement obtained from double-notched $[90/0]_s$ E-glass/913 test coupon using the LCZ method, together with the experimental results [48]. Typical cohesive bands created adaptively during the analysis by the LCZ algorithm are shown in brown colour. Final failure of the coupon occurs due to failure of the 0° plies, accompanied by triangular delamination patterns (shown in green color).

Figure 5.8.a shows the numerically predicted 90° ply matrix damage at

a)   b)   c)
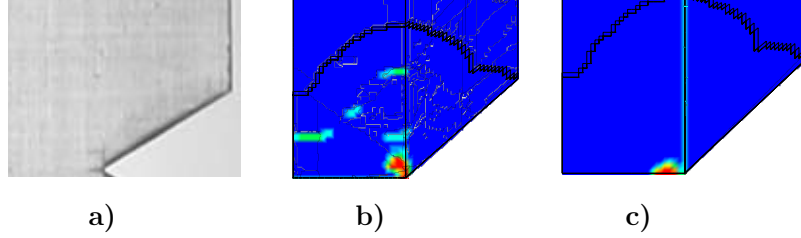
Figure 5.6: Experimental damage, and damage obtained using the LCZ algorithm, applied to a double-notched $[90/0]_s$ E-glass/913 test coupon. Images shown are for 25.8% of the maximum load. **a).** Experimental damage obtained using stills from digital video footage [46] **b).** Transverse matrix damage in the 90° ply. Red colour indicates a fully damaged material, while blue colour indicates an undamaged material. **(c)** Transverse matrix damage at the 0° ply.

the vicinity of the notch at the maximum load before failure. Damaged is predicted to be located along a 10 mm wide narrow section of the test specimen. The experimental results, shown in Figure 5.8.b, agree well with this prediction - the image presents large number of matrix crack located along an area having the width of the narrow section of the coupon (10 mm). Some of these cracks are highlighted in Figure 5.8.b using red rectangles.

Figure 5.9.a shows the numerically predicted matrix damage within the 0° ply. The simulations predict a narrow band approximately 14 mm in wide, of fully developed matrix damage at the 0° ply. Figure 5.9.a shows the experimental obtained damage. Although less noticeable than the cracks in the 90° ply, cracks in the 0° ply are still visible. Several cracks are highlighted using a red rectangle.

(a)

(b)
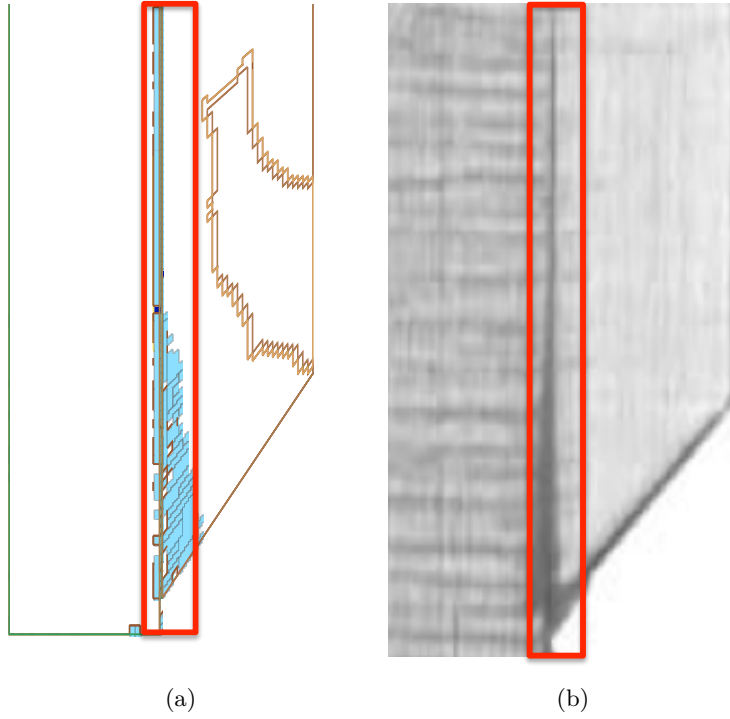
Figure 5.7: Delamination damage in a double-notched $[90/0]_s$ E-glass/913 test coupon, highlighted using red rectangles. **a).** Delamination damage predicted using the LCZ algorithm. **b).** Experimental damage obtained using stills from digital video footage [46].

(a)   (b)
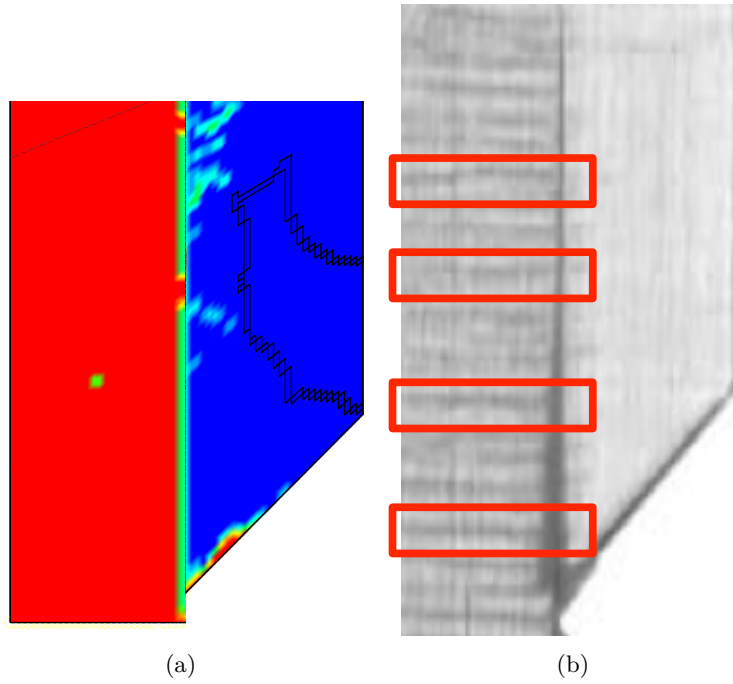
Figure 5.8: 90° ply matrix damage in a double-notched $[90/0]_s$ E-glass/913 test coupon. **a).** Damage predicted using the LCZ algorithm. Fully damaged material is represented using a red color, while undamaged material is colored in blue. **b).** Experimental damage obtained using stills from digital video footage [46]. Several matrix cracks in the 90° ply are highlighted using red rectangles.

(a)   (b)
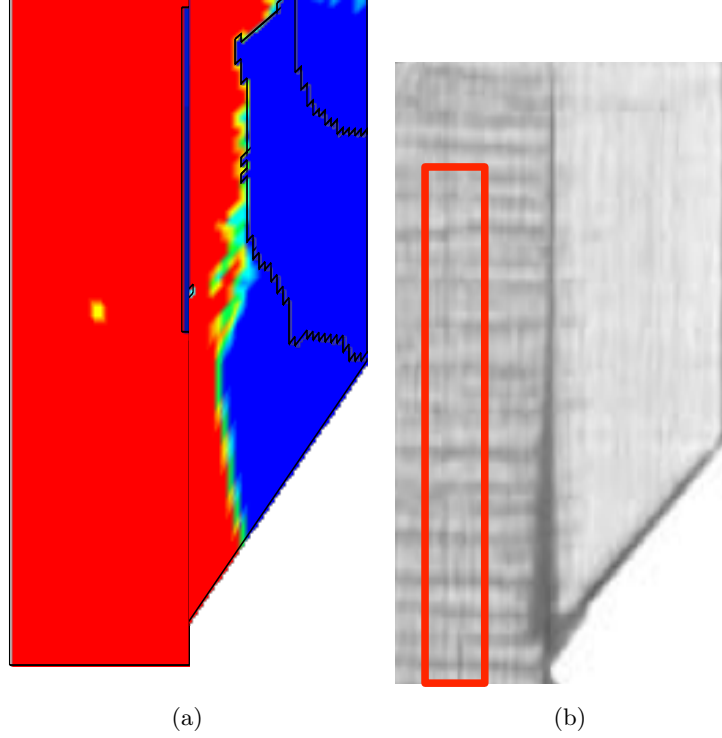
Figure 5.9: 0° ply matrix damage in a double-notched $[90/0]_s$ E-glass/913 test coupon. **a).** Damage predicted using the LCZ algorithm. Fully damaged material is represented using a red color, while undamaged material is colored in blue. **b).** Experimental damage obtained using stills from digital video footage [46]. Several matrix cracks in the 0° ply are highlighted using red rectangles.

5.2 Dynamic Tube Crush Simulation

5.2.1 Introduction

To demonstrate the capability of the LCZ method to model progressive damage in composite structures undergoing impact, a test case involving dynamic axial crushing of composite tubes will be investigated. This problem has been tackled previously using the first generation of the composite damage models, CODAM, developed at the University of British Columbia, and implemented as a user-defined material model in LS-DYNA, in tandem with the built-in cohesive based tie-break contact interface for modelling delamination ([84]). The work performed here, is a continuation of this work - it involved using the second generation of the continuum damage model developed at the UBC Composite group (CODAM2), and applying the LCZ method to test the method's capability to predict delamination under dynamic loading conditions. The cohesive properties were kept constant with respect to the strain-rate of the problem.

Although in some cases the cohesive interface properties might exhibit rate-dependencies, they were treated here as constant with respect to the loading rate of the interface. Introducing strain-rate dependencies to the cohesive model and the LCZ method might be the topic of future research.

5.2.2 Material and Test Specimens

The experiments performed by McGregor et al. [85], included dynamic crushing of braided tubes having a rectangular cross-section. Although several tube dimensions were tested, the work performed here focuses on a two-ply tube configuration, with an initial length of 360 mm having a square cross section, with an outside dimensions of 55 mm and wall thicknesses of 2.3 mm (Figure 5.11.a). The tubes were braided using Fortafil 556 80K carbon as the axial tows, and Grafil 700 12K carbon as the biaxial tows, using Ashland Hetron 922 resin, with each ply having a $[0°/ \pm 45°]$ braid architecture. The $0°$ denotes an angle which is parallel to the tube's main axis. The manufacturer's properties for the resin and braiding materials are listed in Table 5.4.

Dynamic testing of the tubes was conducted in a 10 kJ drop tower using a drop-mass of 535 kg and a maximum drop height of 2.0 m (Figure 5.10). Prior to performing the experiment, each tube was glued to a steel mounting plate using a standard hot melt adhesive, and the mounting plate was bolted to the bottom of the drop mass, with the tube pointing downward. The drop-mass was then allowed to fall freely, and impact a dynamic load-cell

mounted at the bottom of the drop-tower assembly. Two experiments with impact velocities of 2.5 m/s and 2.9 m/s are considered here for simulation purposes For the current study. Figure 5.10.**a** shows the drop tower assembly with the drop-mass located at the upper position, just before being released toward impact with the load cell. The composite tube, connected to the drop mass via the connecting plate, is visible at the center of the image. Figure 5.10.**b** shows an image taken by a fast-speed video camera, with a resolution of 512×512 pixels and 2200 frames per second, just at the moment when the tube-assembly impacted the load-cell located at the bottom of the drop-tower, and before any noticeable deformations are visible. In order to initialize a stable and progressive crushing process, the leading edge of the tubes (located at the tubes-end impacting the load cell) was chamfered at a 45° angle. In addition, a metallic plug was inserted into the bottom of the tube prior to the experiment, to serve as a fracture initiator and to allow the debris/fronds formed during the crushing process to flow smoothly and not accumulate between the tube and the impact plane. The tube, mounting plate, and plug-initiator are shown in Figure 5.11.
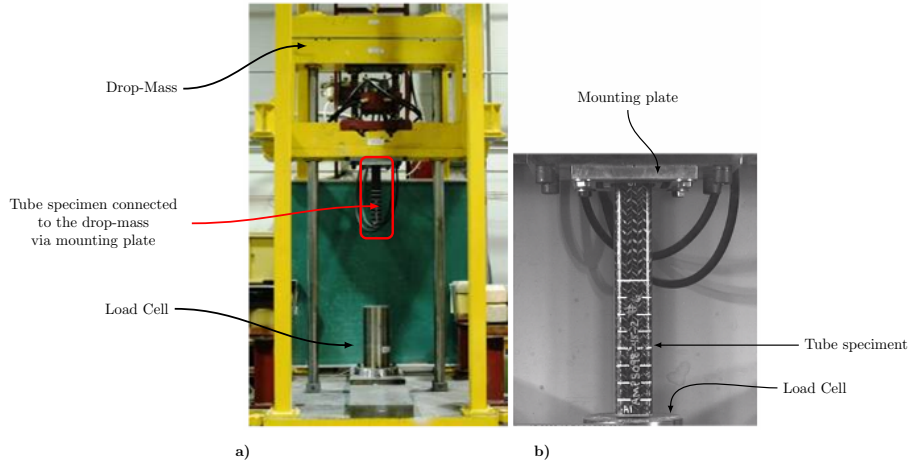
Figure 5.10: Drop tower assembly together with composite tube **a).** The drop-mass is located at the top of the drop tower, to which the composite-tube is connected via the mounting plate. When released, the mass is dropped and the composite tube impacts the load cell. **b).** The composite tube is shown in an image taken using a high-speed video camera, just at the moment of impact with the load cell, before any noticeable deformation is obtained.
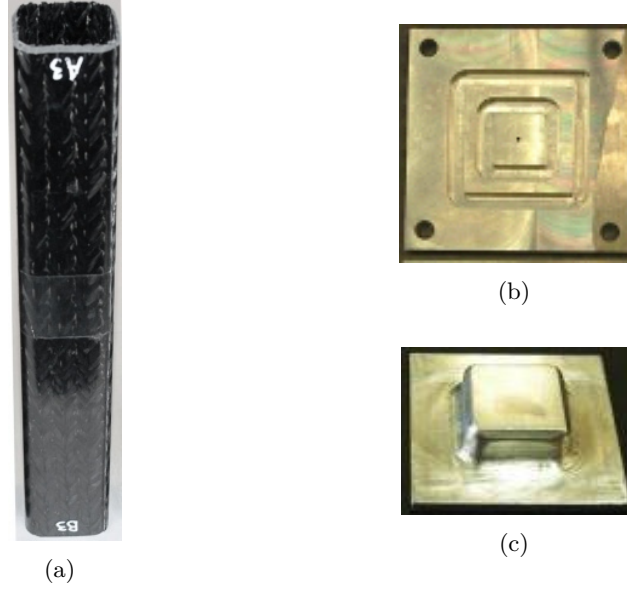
Figure 5.11: **a).** Square-profile Composite tube with a $[0°/ \pm 45°]$ braid architecture used in the tube-crushing experiment. **b).** Mounting plate used to connect the tube to the drop-mass **c).** Plug initiator
.

Table 5.4: Manufacturer's Constituent properties for tube braiding material. Source: [85]

Property	Fortafil #556 80K	Grafil #34 − 700 12k	Hetron 992
Number Of Filaments	80,000	12,000	-
Strength (MPa)	3,790	4,820	86.2
Modulus (GPa)	231	234	3.17
Density (g/cm³)	1.8	1.8	1.14
Tow cross-sectional area (mm²)	2.34	0.444	-
Elongation At Break (%)	1.64	2	6.7
Filament Diameter (μm)	6	7	-

Force vs. displacement results from the tube-crush experiments are brought in Figure 5.12, for impact velocities of 2.5 m/s and 2.9 m/s. It

is noticeable that the plug-initiator and the tube leading edge which was intentionally chamfered at 45°, successfully eliminated the initial load-peak, as their presence initialized the fracture at an early stage and allowed progressing and stable crushing to develop without the presence of a maximum-load level which is considerably higher than the average load during the stable crushing process.

The work performed during the crushing process was calculated using Equation C.1. Values of $W_f = 2629.05$ J and $W_f = 3541.57$ J were computed for the 2.5 m/s and 2.9 m/s impact velocities, respectively. Using a tube cross-sectional area of 475.87 mm², material density $\rho = 1.3 \times 10^{-3}$ g/mm³ in Equation C.2, resulted in values of SEA which are equal to 23.11 J/g and 23.29 J/g for the 2.5 m/s and 2.9 m/s impact velocities, respectively.
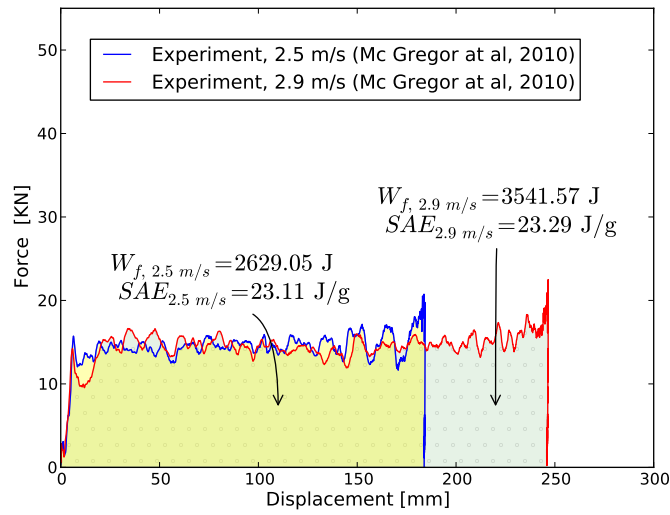
Figure 5.12: Force vs. displacement results obtained from the tube-crush experiments, for impact velocities of 2.5 m/s and 2.9 m/s (McGregor et al. [85]). The work performed during the crushing process, as well as the specific Energy Absorption values were calculated using Equation C.1 and Equation C.2, and are displayed as well.

5.2.3   Finite Element Model

In order to apply the LCZ method to the problem, and provide an alternate and comparative numerical solution to the LCZ method's results, two simulation approaches are used. In the first approach (Figure 5.13), which is referred to as the conventional cohesive zone method (conventional CZM) within this thesis, the 2-ply braided composite tube is represented by two layers of regular shell elements with an element size of 2.5mm, each with 4 through-thickness integration points and tied together using a conventional cohesive type tie-break contact interface available in LS-DYNA. The material behavior of each shell element is governed by CODAM2 (MAT219) in LS-DYNA, which is the second-generation of the sub-laminate based continuum damage mechanics models developed at the University of British Columbia.

In the second modelling approach where the adaptive LCZ algorithm is applied to the problem, the tube is modelled using a single layer of thick-shell elements (ELFORM=5 in LS-DYNA) through the thickness of the tube (Figure 5.14), with 8 integration points through the element thickness. Here, too, the element size used was 2.5mm. No cohesive elements are introduced in the model prior to the analysis, as they are added adaptively to the structure during the transient simulation.

In both modelling approaches, the chamfer at the end of the tube is modelled using a row of shell elements with a thickness equal to half the thickness of the tube wall, connected to the end of the tube. These shell elements are the first to come in contact with the plug initiator. These elements are required in order to initiate a stable crushing process.

In both modelling approaches, the finite element model consists of 3 main components: a drop weight, a tube, and a plug to initiate the crushing process. Only a quarter of each component is modelled as shown in Figure 5.13 and in Figure 5.14, and the required symmetry boundary conditions are enforced accordingly. The drop weight is modelled as a rigid body using solid elements with a mass of a quarter of the total mass (i.e. 134 kg). The plug initiator is also modelled as a rigid body using solid elements and is fixed in space.
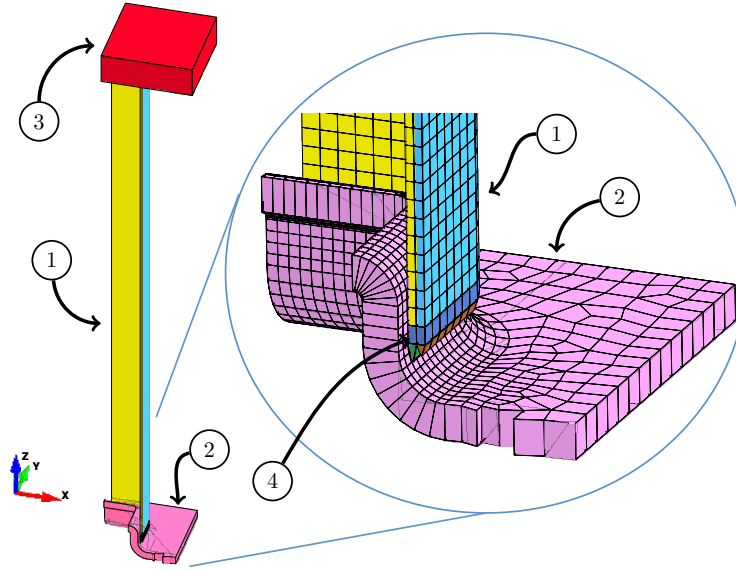
Figure 5.13: An isometric view of the LS-DYNA finite-element model used for the tube-crush analysis in Phase *I* and Phase *II*, and concisted of the following parts: Composite tube (**1**), plug (**2**), dropped mass (**3**). The 45° chamfer at the leading-edge of the tube was modelled using shell elements with varying cross-section thickness (**4**)

An initial velocity of 2.7 m/s (corresponding to the average of the two velocities, 2.5 m/s and 2.9 m/s, used in the tests) is assigned to the drop weight causing the tube to impact the plug.
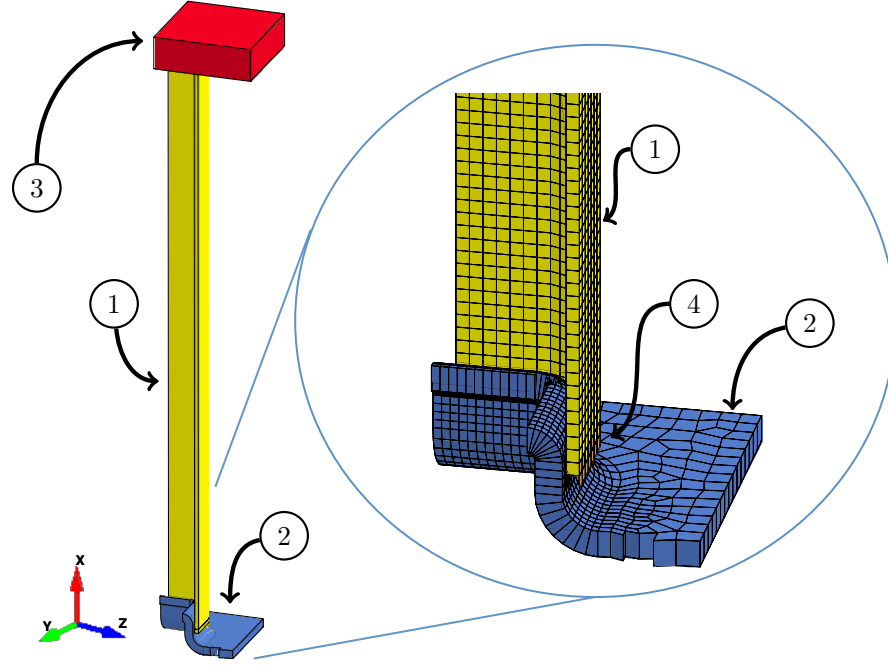
Figure 5.14: An isometric view of the LS-DYNA finite-element model used for the tube-crush analysis, consisting of the following parts: Composite tube (**1**), plug (**2**), dropped mass (**3**), and a row of shell elements, resembling the 45° chamfer which is present in the experimental tube, which is required in order to initiate a stable crushing process (**4**).

5.2.4   Intralaminar Damage Modelling

CODAM2 (Forghani [35], Forghani et al. [37]), served as the intralaminar damage model for the braided tube . Within CODAM2, the intra-laminar damage consisting of fibre breakage and matrix cracking is modelled using a sub-laminate based approach, which acknowledges the existence of orthotropic layers within the sub-laminate and casts the damage formulation in terms of the strain components in those directions. Another feature of this material model, compared to its predecessor, is its non-local averaging capability. This is to alleviate the problem of mesh size and orientation dependency which is commonly encountered in continuum damage models that lead to a strain softening response. CODAM2 has been implemented

as a built-in material model (MAT219) in LS-DYNA, thus making it possible to take advantage of the efficiencies that come with all of the built-in features of the code, a requirement for the LCZ method to be applied to the problem.

The CODAM2 parameters required to identify the in-plane orthotropic response of the braided material were estimated using constituent properties and information obtained from standard and specialized coupon tests. The details of material characterization can be found in McGregor et al. [87]. Based on the failure mechanisms of the tube, tension along the local y-axis (transverse or hoop direction) and compression along the local x-axis (axial or longitudinal direction) were identified as the primary loading directions. Therefore, the input material damage properties were calibrated assuming the braided material system to be an equivalent (lumped) single layer of orthotropic composite.

The input model parameters are calibrated based on the characterized properties for a representative volume element (RVE) for each damage mode, together with the physical and elastic material properties, are listed in Table 5.5. The strain values for the damage saturation associated with all damage modes are scaled according to the size of the element, such that for each mode of loading, the fracture energy is element size independent, in keeping with Bazant's crack band scaling method (Bazant and Planas [10]). A detailed description of the calibration process is brought in Appendix F.

Figure 5.15.a and Figure 5.15.b show the resulting stress-strain profile that result from applying the calibrated material model to a 2.5mm element under axial and hoop loading directions, respectively.

5.2.5 Interlaminar Damage Modelling

In the standard modelling approach, where delamination damage is simulated using a conventional tie-break interface, the interface damage initiates when a quadratic traction-based criterion is satisfied. When this criterion is met, the interface tractions are gradually decreased to zero at a user-defined critical crack opening displacement. The traction-separation law used for this model is considered to be identical for both the normal (Mode I) and shear (Mode II) crack openings (see Table 5.5 for the input variables used). These values are the same as those used by McGregor et al. [85] to simulate the tube crushing experiments where a tie-break contact was also used to model delamination.

In the second approach where the LCZ algorithm is applied for delamination modelling, the cohesive elements which are adaptively added to the
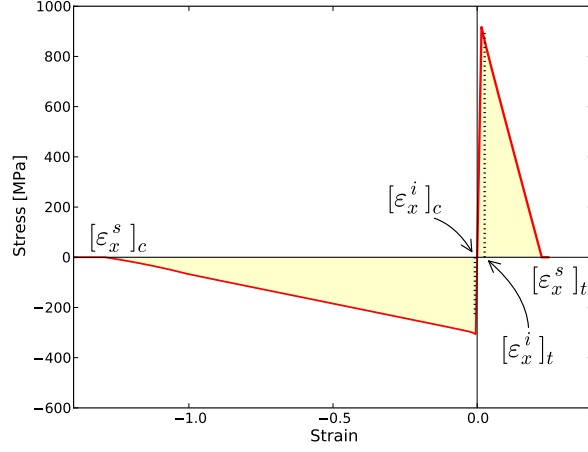
(a)
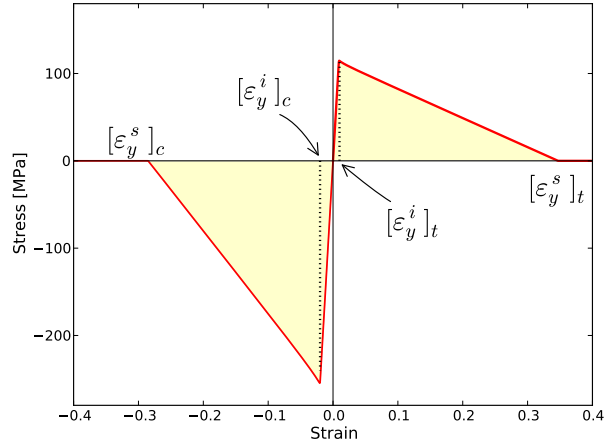
(b)

Figure 5.15: Stress - strain curves used as an input for the CODAM2 material model, calibrated for a 2.5 mm element size. **a.** Axial loading direction where $[\varepsilon_x^i]_t$ and $[\varepsilon_x^s]_t$ denote the damage initiation and saturation strains in tension, $[\varepsilon_x^i]_c$ and $[\varepsilon_x^s]_c$ denote the damage initiation and saturation strains in compression. **b.** Transverse loading direction where $[\varepsilon_y^i]_t$ and $[\varepsilon_y^s]_t$ denote the damage initiation and saturation strains in tension, $[\varepsilon_y^i]_c$ and $[\varepsilon_y^s]_c$ denote the damage initiation and saturations strains in compression.

90

Table 5.5: Model input parameters for the $[0°/\pm45°]$ braided composite tube.

Property	Value	Unit
Density[a]	1.3×10^{-3}	g/mm^3
Ply thickness[a]	1.15	mm
Elastic		
Longitudinal elastic modulus[a] (E_{xx})	60	GPa
Transverse elastic modulus[a] (E_{yy})	12.5	GPa
Out-of-plane elastic modulus[c] (E_{zz})	8	GPa
Major Poisson's ratios[c], ($\nu_{yx} = \nu_{zx} = \nu_{zy}$)	0.3	(-)
In-plane shear modulus[a] (G_{xy})	9	GPa
Transverse shear modulus[c] ($G_{xz} = G_{yz}$)	9	GPa
Intralaminar damage		
Initiation strain for damage under tension in the transverse direction [a] $[\varepsilon_y^i]_t$	9×10^{-3}	(-)
Saturation strain for damage under tension in the transverse direction[b] $[\varepsilon_y^s]_t$	3.47×10^{-1}	(-)
Initiation strain for damage under tension in the axial direction[a] $[\varepsilon_x^i]_t$	1.5×10^{-2}	(-)
Saturation strain for damage under tension in the axial direction[b] $[\varepsilon_x^s]_t$	2.24×10^{-1}	(-)
Initiation strain for damage under compression in the transverse direction[a] $[\varepsilon_y^i]_c$	2×10^{-2}	(-)
Saturation strain for damage under compression in the transverse direction[b] $[\varepsilon_y^s]_c$	2.85×10^{-1}	(-)
Initiation strain for damage under compression in the axial direction[a] $[\varepsilon_x^i]_c$	5×10^{-3}	(-)
Saturation strain for damage under compression in the axial direction[b] $[\varepsilon_x^s]_c$	1.29	(-)
Interlaminar damage		
Interlaminar normal strength[a] (σ_{max})	50	MPa
Interlaminar shear strength[a] (τ_{max})	50	MPa
Mode I critical energy release rate[a], (G_{Ic})	1.75	kJ/m^2
Mode II critical energy release rate[a], (G_{IIc})	1.75	kJ/m^2

[a] Source: [85].
[b] Calibrated values, as described in Section 5.2.4.
[c] Assumed value in this study.

structure, are 8-noded solid elements (*ELEMENT SOLID, ELFORM=19). LS-DYNA's *MAT COHESIVE GENERAL material model is assigned to these elements in order to capture the interface failure. The cohesive parameters used in this model are identical to those listed in Table 5.5 for the tie-break interface. In order to assess the potential for splitting the structural thick-shell elements and seeding the solid cohesive elements, the following interactive stress-based element-splitting criterion was used in the analysis:

$$S = \sqrt{\left(\frac{\sigma_n}{\sigma_{max}}\right)^2 + \left(\frac{\sigma_s}{\tau_{max}}\right)^2} \geq S_c \qquad (5.2)$$

where σ_n and σ_s are the through-thickness normal and shear stress components with σ_{max} and τ_{max} being the respective maximum values of these quantities. The critical value for splitting the thick-shell elements, S_c, is assumed to be 0.5, which is sufficiently large to allow the cohesive elements to be introduced in relatively small regions of the model. The maximum values of the out-of-plane normal and shear stresses, σ_{max} and τ_{max}, are taken to be 50 MPa, and the radius of the splitting region, R is assumed to be 8 mm, slightly more than three times the element size used in the analyis, which is recommended in order to capture the correct behavior of the crack propagation using CZM. A coefficient of friction of 0.22 was defined for the contact between the newly created surfaces, and a value of 0.32 was used between the tube and the plug. This value is slightly higher than the value, 0.22, used by McGregor et al. [85], as preliminary simulations using solid cohesive elements showed that a slightly higher value of the friction coefficient was necessary in order to obtain accurate results.

5.2.6 Results and Discussion

The force vs. displacement results obtained from the numerical simulation (CODAM2 / LCZ) is presented in Figure 5.16, together with results obtained using classical shells and a tie-break contact algorithm. The corresponding experimental results reported in McGregor et al. [86] are also shown for comparison. Good agreement between the numerical and experimental results is obtained. The final obtained displacements at which the dropped mass was brought to a halt is 224.16 mm, which is within the range of the maximum displacement measured for the lower and higher impact velocities used in the tests (183.87 mm and 245.83 mm, for impact velocities of 2.5 m/s and 2.9 m/s, respectively).
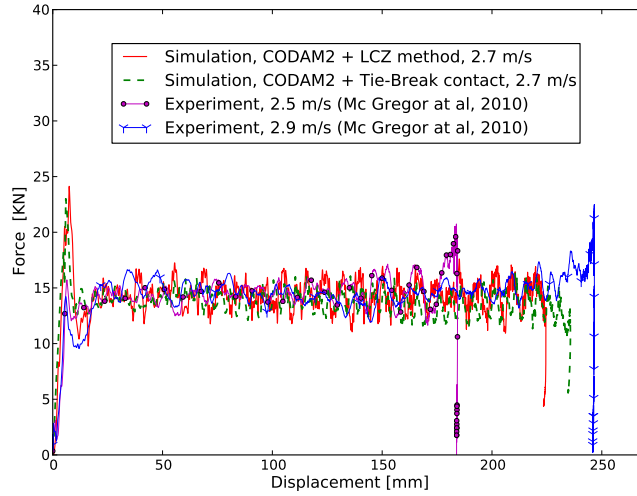
Figure 5.16: Force vs. displacement results obtained from the numerical simulation of the tube crush tests using the combined CODAM2 and the LCZ algorithm. Also shown for comparison are the results obtained using the conventional delamination modelling approach that employs the tie-break contact interface. These results for impact velocity of 2.7 m/s are shown together with the experimental results for impact velocities of 2.5 m/s and 2.9 m/s.

The predicted initial peak force, which is noticeable before stable crushing begins, exceeds the corresponding force measured in the experiments,

probably due to the inaccurate discretization of the chamfer which plays an important role in initializing a stable and progressive crushing. The specific energy absorption (SEA) calculated from the numerical simulation (23.21 J/g) is in very good agreement with the experimentally determined values of 23.11 J/g and 23.29 J/g corresponding to impact velocities of 2.5 m/s and 2.9 m/s, respectively.

Both the conventional modeling approach, as well as the LCZ method, yield a similar topology of the crushed tube geometry, which is shown for the bottom of the tube (crushed zone) in Figure 5.17. As the tube is forced against the plug, its plies fail due to a combination of several damage mechanisms, mainly tension along the y-axis and compression along the x-axis, and delamination which results in complete separation of the plies. Fronds are created as the progressive crushing process continues and the tube is further pushed against the plug.
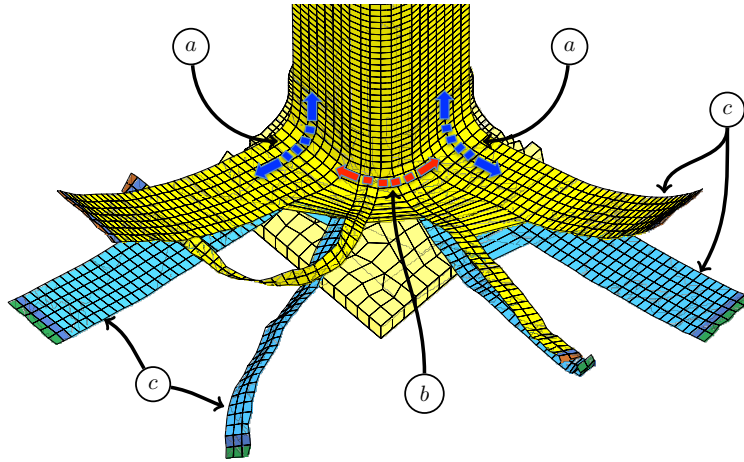
Figure 5.17: Typical topology of the crushed tube geometry, demonstrating the dominant damage mechanisms. Transverse (hoop) damage develops at the tube's corners (**a**), Delamination results in complete separation of the plies (**b**). Fronds are created as the progressive crushing process continues and the tube is further pushed against the plug (**c**).

Figure 5.18 shows a close-up view at the bottom of the tube, demonstrating the propagation of the cohesive-band when the LCZ method is applied. The initial finite element model contains no cohesive elements, and the tube is modelled using a single through-thickness layer of thick-shell elements

(Figure 5.18.a). As the element-splitting criterion is satisfied within the first thick-shell element, a splitting operation is performed and solid-cohesive elements are introduced into the model, shown in a darker colour in Figure 5.18.b. As the tube is pushed against the plug, elements located at the tube's corners fail, and fronds consisting of shell elements begin to develop (Figure 5.18.c). Progressive and stable crushing process develops, at which elongated fronds are created as the tube is pushed against the plug and the cohesive band further propagates into the tube. New cohesive elements are created along the leading edge of the cohesive band, and as cohesive elements are deleted due to delamination, shell elements are separated and new, free surfaces, are created (Figure 5.18.c).
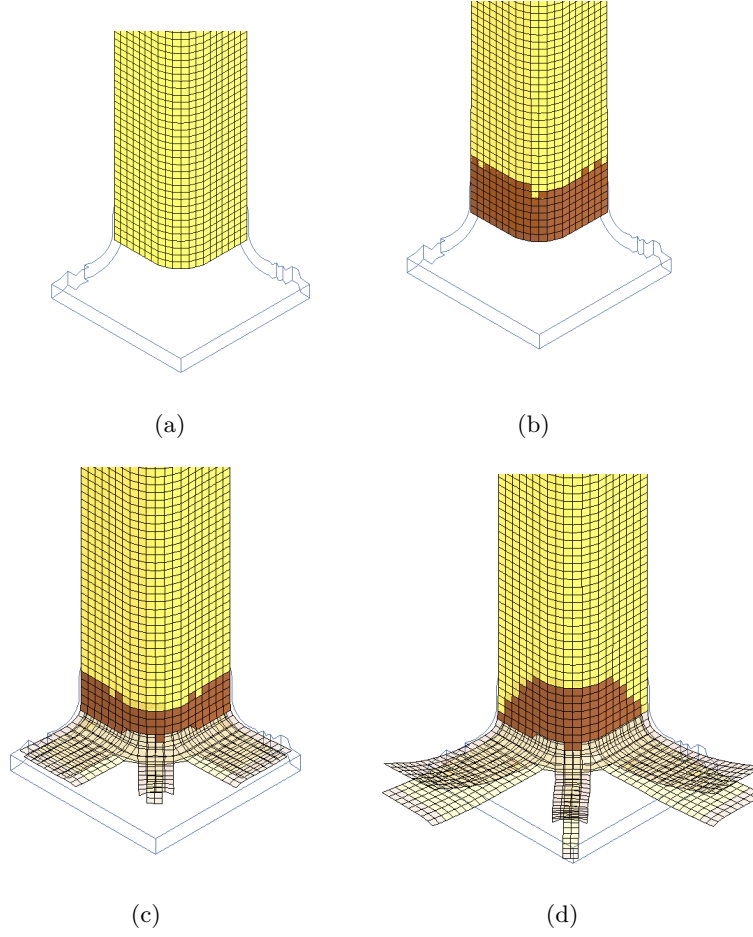
Figure 5.18: Propagation of the cohesive-band when the LCZ method is applied to the tube-crushing simulation. **a).** Initial finite element model. **b).** Solid-cohesive elements are introduced into the model as the element-splitting criterion is satisfied, shown here in a darker colour. **c).** Fronds consisting of shell elements develop. **d).** Progressive and stable crushing process results in separation of shell elements as new surfaces are created.

The model topology and CODAM2 damage values for the axial and hoop directions, reported at $t = 40$ ms after initial impact, are shown in Figure 5.20 and Figure 5.19, respectively, for both the conventional CZM, as well as results obtained from applying the LCZ method to the problem. The topology obtained from both methods are similar but not identical - the

fronds created using the LCZ method are somewhat more symmetric compared to the fronds obtained using the conventional CZM. A slight difference can be seen in the intralaminar (CODAM2) damage values reported, where the LCZ method yields some regions of lower axial damage value compared to the conventional CZM.

This example demonstrates the ability of the LCZ method to model the progression of delamination in a dynamic event, without prior introduction of cohesive elements or cohesive contact at all possible ply interfaces in the finite element mesh. Although some minor differences are observed when the method is compared to the standard application of the cohesive-zone method to the problem, the LCZ method is able to correctly predict the force vs. displacement profile, the SEA of the material, as well as the total displacement of the dropped-mass.
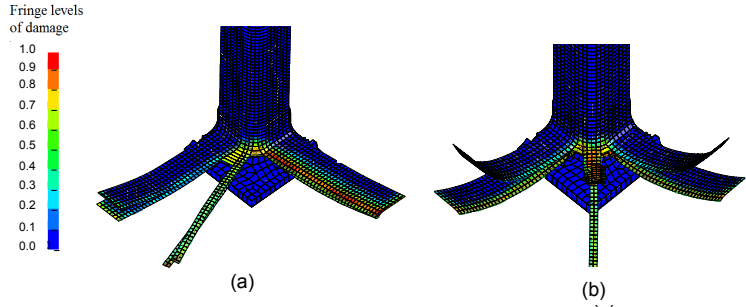
Figure 5.19: Model topology and CODAM2 intralmainar damage values in the axial direction (compression), at $t = 40ms$. Damage value of 0.0 represents an undamaged material, and a damage value of 1.0 represents a fully damaged material. **a)**. Results obtained using the conventional CZM. **b)**. Results obtained using the LCZ method.

5.3 Dynamic Plate Impact Simulations

In order to validate the predictive capability of the LCZ method to simulate a dynamic loading case involving multiple through-thickness delamination crack propagation, non-penetrating impact response of T800/3900-2 CFRP laminates with quasi-isotropic stacking sequence of $[45/90/-45/0]_{3s}$ was investigated. The impact experiments, performed by Delfosse et al. [24], covered a wide range of impact energies obtained using high-mass drop-weight
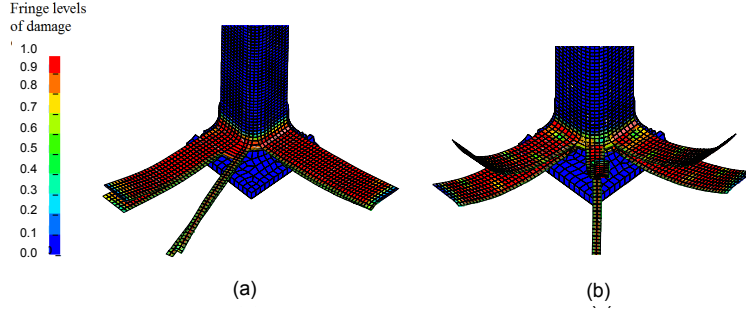
Figure 5.20: Model topology and CODAM2 intralmainar damage values in the hoop direction (tension), at t= 40 ms . Damage value of 0.0 represents an undamaged material, and a damage value of 1.0 represents a fully damaged material. **a)**. Results obtained using the conventional CZM. **b)**. Results obtained using the LCZ method.

and low-mass gas-gun impact tests. Similar to the case of the dynamic tube-crush validation problem, the cohesive interface properties were treated here as constant with respect to the loading rate of the interface. Introducing strain-rate dependencies to the cohesive model and the LCZ method might be the topic of future research.

5.3.1   Material and Test Specifications

A rectangular composite plate, 152.4 mm ×101.6 mm ×4.65 mm in size (Figure 5.21 and Figure 5.22), served as a target for the experiments. The plate was clamped to an aluminum backing plate having a 76.2 × 127.0 mm^2 rectangular opening, using four rubber fasteners (Figure 5.22), and impacted using a 25.4 mm diameter hemispherical shaped hardened steel projectile.

The experiments performed by Delfosse et al. [24] consisted of low-velocity impact tests, where a 6.33 kg impactor was dropped from a drop tower from various heights, impacting the plate at velocities ranging from 1.76 m/s to 4.29 m/s (Resulting in impactor's kinetic energies of 9J to 56J, for the lowest and highest impact velocities, respectively), and high-velocity tests, in which a 0.314 kg projectile was launched using a gas gun, and impacted the plate at velocities ranging from 7.74 m/s to 23.19 m/s (Resulting in projectile's kinetic energies of 9J to 58J, for the lowest and highest impact velocities, respectively). The contact force between the plate and the pro-
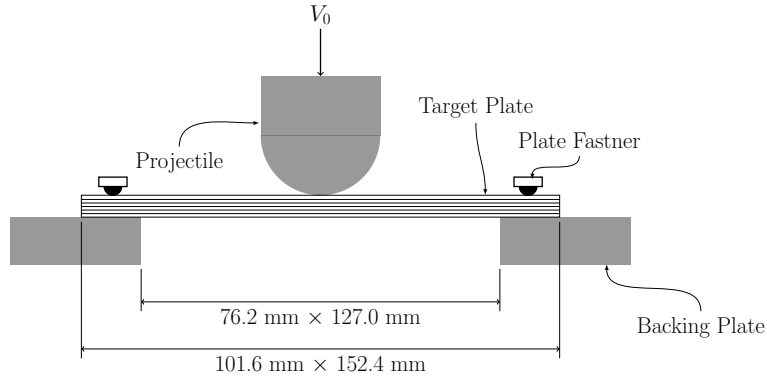
Figure 5.21: A side view of the plate-impact experiment configuration. A composite target plate is attached to an aluminum backing plate using four rubber fasteners (of which only two are shown in the figure). The projectile has an initial velocity V_0 as it strikes the plate at normal incidence.
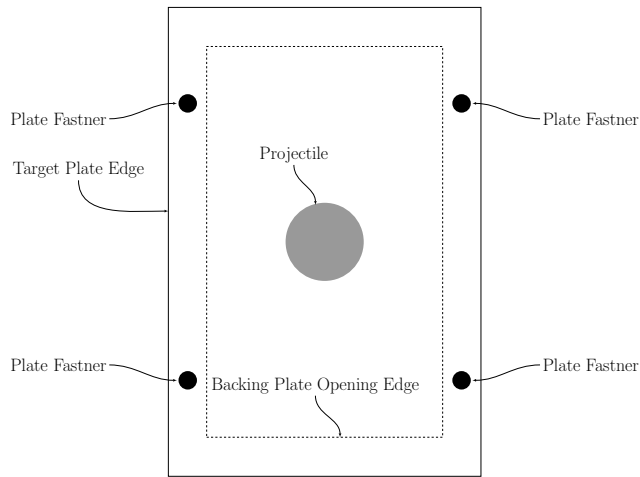
Figure 5.22: A top view of the plate-impact test configuration. The target plate is attached to the aluminum backing plate using four rubber fasteners. The opening in the aluminum backing plate is marked using a dashed line.

jectile was measured using a load-cell, and impact velocities were measured using three pairs of optical gates placed right before the point of impact. The resulting projected internal delamination area was mapped using pulse-echo ultrasonics. Since the equipment was capable of mapping the first level of delamination encountered through the thickness of the panel, a destructive inspection process was carried out to determine the total delamination area Delfosse et al. [24].

5.3.2 Finite Element Model

Figure 5.23 shows an isometric view of the finite-element model. Due to symmetry, only a quarter of the test configuration is modelled, and the required boundary conditions are applied to the finite-element model accordingly. Similar to an assumption made by Forghani and Vaziri [36] and Williams et al. [129], only the portion of the plate which is positioned above the aluminum-backing opening is modelled (i.e the size of the actual plate modelled is 76.2 mm×127 mm), and simply supported boundary condition are applied around the free edges of the plate. The plate is modelled using LS-DYNA's thick-shell elements, with an in-plane square element size of 1 mm. Several models were tested, with varying number of through-thickness thick-shell elements (1, 3, 4 and 5), in order to assess the sensitivity of the results to the number of potential through-thickness delamination cracks. The projectile was modelled using perfectly-rigid solid elements, with an appropriate material density that would yield masses of 6.33 and 0.314 kg, based on the test conditions. An initial projectile velocity was defined in the negative z-direction, with a value suiting the case under investigation. The model was analyzed using the default time step size calculated by the explicit solver, resulting in a time step size ranging from 1×10^{-5} to 6×10^{-5} ms, depending on the number of through-thickness elements in the model (where a smaller time step size relates to a higher number of through-thickness thick-shell elements).

5.3.3 Intralaminar Damage Modelling

The intralaminar modelling approach used in the analysis, is based on the previous work by Forghani and Vaziri [36]. LS-DYNA's built-in isotropic material model, *MAT PLASTICITY WITH DAMAGE (*MAT_81), which combines both damage and plasticity, is used in order to simulate damage evolution within each sublaminate ([45°/90°/ − 45°/0°]). Since the laminate (and its sublaminates) investigated in this study are quasi-isotropic
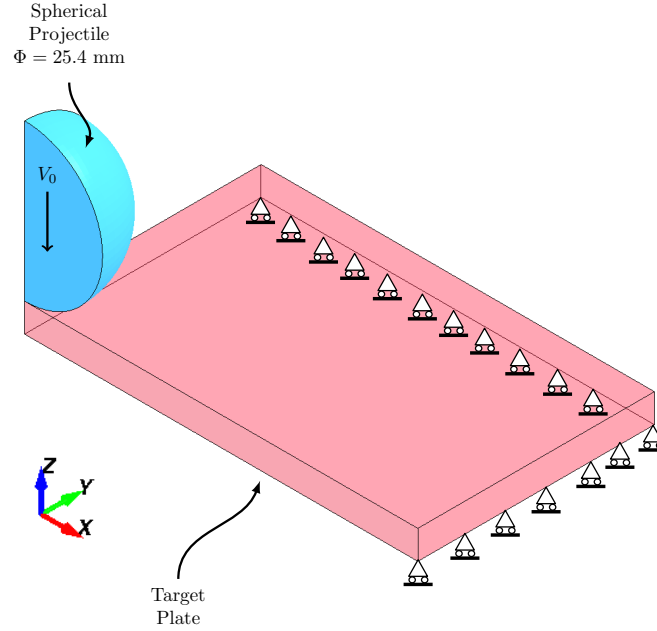
Figure 5.23: An isometric view of the plate-impact finite-element model. Due to the problem's symmetry, a quarter of the test geometry is modelled. Similar to an assumption made by Forghani and Vaziri [36] and Williams et al. [129], only the portion of the plate which is positioned above the aluminum-backed opening is modelled (i.e the size of the actual plate modelled is 76.2mm ×127 mm), and simply supported boundary conditions are applied to the free edges of the plate

and therefore exhibit an isotropic behavior in-plane, this material model is considered to be a suitable choice.

A typical behavior of *MAT_81 under cyclic loading is shown in Figure 5.24. Upon loading, stress increases linearly along the loading path $\bar{o}a$, until the value of the stress reaches its maximum value, σ_u. As the loading further increases, the stress drops linearly, until it reaches point b, where unloading begins. The unloading path $\bar{b}c$ does not follow a secant path to the origin, and it crosses the state of zero stress at point e. It is characterized by a reduced slope compared to the loading path $\bar{o}a$, driven by some damage that has already developed in the material. During a second loading cycle, a decrease in the ultimate strength of the material is noticeable, where the value of the maximum stress now reaches point f.

Within *MAT_81 , the maximum stress σ_u, and the stiffness of the damaged material, C^d, are scaled based on the growth of a damage parameter, d, which is a user-defined function of the equivalent plastic strain. The value of the maximum stress σ decreases based on the following equation:

$$\sigma = \sigma_{eff}(1 - d) \tag{5.3}$$

where σ_{eff} is the value of the effective stress.

The structural stiffness of the damaged material, C^d, decreases with a growth of d, according to the relation:

$$C^d = C^0(1 - d) \tag{5.4}$$

where C^0 is the undamaged-material stiffness. For more information regarding the behavior of *MAT_81, the reader is referred to LS-DYNA users manual (2013) and [26].
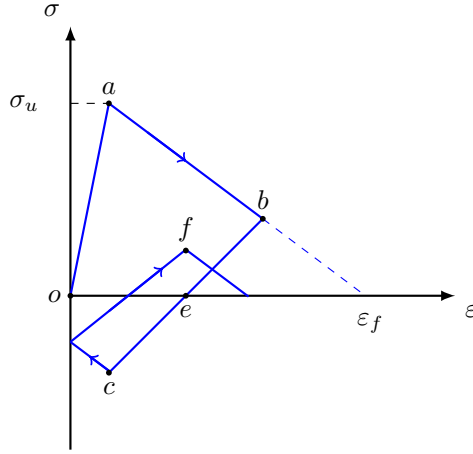
Figure 5.24: Typical strain-softening behavior of LS-DYNA's *MAT PLASTICITY WITH DAMAGE material model (*MAT_81) during a full load/unload cycle. This material model is used to simulate the in-plane damage behavior of the sublaminate of the T800/3900-2 CFRP laminate with layup of $[45/90/-45/0]_{3s}$

The material parameters used in the analysis are based on the values used by Forghani and Vaziri [36] for simulating the plate impact event. The lamina elastic properties of the T800/3900-2 CFRP and the effective sublaminate properties are listed in Table 5.6.

Table 5.6: Model input parameters for the T800/ 3900-2 CFRP sublaminate [45°/90°/−45°/0°] (Williams et al. [129] and Forghani and Vaziri [36])

Property	Value	Unit
Density	1.543×10^{-3}	g/mm^3
Sublaminate thickness	0.775	mm
Elastic		
Effective elastic modulus[a] ($E_{xx} = E_{yy} = E_{zz}$)	48.37	GPa
Effective shear modulus[a] ($G_{xy} = G_{yz} = G_{zx}$)	18.36	GPa
Effective Poisson ratios[a] ($\nu_{xy} = \nu_{yz} = \nu_{xz}$)	0.32	(-)
Intralaminar damage		
Intralaminar peak stress (σ_u)	800	MPa
Intralaminar damage saturation strain (ε_f)	0.148	(-)
Interlaminar damage		
Mode I critical energy release rate (G_{Ic})	0.8	kJ/m^2
Mode II critical energy release rate (G_{IIc})	2.0	kJ/m^2
Interlaminar normal strength (σ_{max})	80	MPa
Interlaminar shear strength (τ_{max})	150	MPa

[a] Out-of-plane elastic properties are assumed to be the same as the in-plane properties because of the isotropic limitations of *MAT_81 material model in LS-DYNA .

5.3.4 Interlaminar Damage Modelling

Interlaminar damage is modelled using LS-DYNA's cohesive solid elements, to which *MAT_81 is assigned. Similar to the tube crush benchmark problem, a mixed mode criterion is used, in order to account for the interactive effect of damage in mode-I and mode-II loading. The interlaminar damage properties used in the analysis are listed in Table 5.6.

Similar to the tube crush benchmark problem, two modelling approaches were used: The conventional application of the CZM, where cohesive elements were present along all potential delamination interfaces prior to the analysis, and the LCZ method, where cohesive elements were adaptively seeded along the delamination propagation interface using the LCZ

algorithm. An interactive stress-based element-splitting criterion was used (Equation 5.2) in order to assess the potential for splitting the structural thick-shell elements and seeding the solid cohesive elements . The critical value for splitting the thick-shell elements, S_c, is assumed to be 0.4. Choosing a small value for this parameter will cause large number of thick-shell elements to satisfy the element splitting criterion, thus increasing the size of the geometrical region being split in each splitting step, making the LCZ method less favourable compared to the conventional CZM. Increasing the value of S_c, however, will result in smaller regions of thick-shell elements to be split, up to a point where excessive numerical noise is introduced. The maximum values of the out-of-plane normal and shear stresses, σ_{max} and τ_{max}, are taken to be 80 MPa and 150 MPa, respectively, and the radius of the splitting region, R is assumed to be 8 mm, to allow sufficient number of cohesive elements to be included within the cohesive band. A coefficient of friction of 0.4 was defined for the contact between the newly created surfaces, which is an acceptable value for rough composites. The multi-delamination capability of the LCZ method is applied to the problem, i.e, each thick-shell element can adaptively split through its thickness, and since the plate was modelled using multiple number of through-thickness elements, multiple delamination cracks can propagate independently within the material.

5.3.5 Results and Discussion

In order to examine the capability of the LCZ method to simulate the plate-impact event, impact force and kinetic energy time histories were computed and compared to the results obtained from the application of the conventional CZM to the problem, as well as the results obtained from the experimental data. Similarly, the predicted damage patterns were examined and compared to available experimental measurements. The results are presented for different number of through-thickness cohesive interfaces, when using the conventional CZM, the FE models included the a-priori placed cohesive interfaces, while when using the LCZ method, the cohesive elements were automatically generated and seeded during the computational run.

4.29 m/s Impact Event

For an impactor mass of 0.314 kg impacting the plate at 14.59 m/s, Figure 5.37 and Figure 5.38 show the impact-force vs. time and impact-force vs. displacement profiles, respectively, obtained from the simulations using

different number of through-thickness cohesive interfaces.

When a single cohesive interface is used, unstable growth of delamination occurs, resulting in a sudden load drop which is visible in Figure 5.25.a at a time of approximately 1.1 ms from impact, and in Figure 5.26.a at a displacement of approximately 4.5 mm. According to the conventional CZ prediction, this sudden growth of delamination leads to a delamination crack that spans across most of the plate (Figure 5.7), where the LCZ method predicts complete failure of the cohesive interface. Neither of these behaviors was observed in the experiment, as can bee seen by examining the experimental delamination pattern which is shown at the bottom of Table 5.7. It is believed that this unstable growth can be driven by an insufficient through-thickness mesh refinement, which does not allow correct distribution of the energy through the interlaminar and intralaminar damage mechanisms. However, the divergence of the delamination area predicted by the LCZ solution from the experimental findings is smaller compared to the results predicted by the conventional CZ method.

As the number of cohesive interfaces is increased, better prediction is obtained. Both of the LCZ's method and the conventional CZ's method predictions yield stable results for the 3, 4, and 5 cohesive-interface models investigated. For the first 2 ms after impact, as the impactor is bending and pushing the plate downwards, the 3, 4 and 5 interface models show good agreement between the experiment and the numerical predictions, for both conventional CZ as well as the LCZ method's predictions. As the maximum load is reached, and the impactor begins to rebound from the plate, both conventional and LCZ method over predict the force compared to the experimental results, for the 3 and 5 interface models. For the 4 interface model, the LCZ method's prediction is higher in the rebound phase compared to the numerical prediction of the conventional CZ, up to a time of approximately 4 ms from impact, and is then lower compared to the conventional CZ prediction until complete separation of the impactor from the plate.

Examining the delamination patterns predicted by the simulation for different number of interfaces (Table 5.7), it can be seen that better prediction of the delamination pattern is obtained as the number of cohesive interface is increased, for both conventional CZ and the LCZ method. The experimental delamination pattern is somewhat oval, and increasing the number of cohesive interfaces results in a better depiction of this oval contour by the simulations. The contour predicted by the LCZ method using the 4 interface model is an exception for this behavior, where a somewhat less oval pattern is obtained compared to the pattern predicted by the 3 inter-

Figure 5.25: Predicted and experimental impact force vs. time for a 6.33 kg impactor, impacting the plate at 4.29 m/s. The numerical results were obtained using the LCZ method and the conventional CZM, for different number of through-thickness cohesive interfaces: **a).** 1 cohesive interface**b).** 3 cohesive interfaces **c).** 4 cohesive interfaces **d).** 5 cohesive interfaces.

face model. Further increasing the number of cohesive interfaces from 4 to 5 will improve the results, and yield a contour that better resembles the experimental findings.

The predicted propagations of delamination at different time states, are shown in Figure 5.27.a and b, for the conventional CZM and LCZ methods, respectively, where both methods are solved using a model that employs 5 cohesive interfaces. The figures show a local cross-sectional view of the plate in the vicinity of the impactor, where the coloured regions mark the

Figure 5.26: Predicted and experimental impact force vs. plate displacement, for a 6.33 kg impactor, impacting the plate at 4.29 m/s. The numerical results were obtained using the LCZ method and the conventional CZM, for different number of through-thickness cohesive interfaces: **a).** 1 cohesive interface **b).** 3 cohesive interfaces **c).** 4 cohesive interfaces **d).** 5 cohesive interfaces.

delamination crack along the interfaces. The cross-section is taken along the length of the plate. Delamination damage first appears at around $t = 0.6$ms from impact. Delamination damage predicted by the LCZ method, initiates at the central interface, whereas delamination predicted by the conventional CZM initiates at interface numbers 2 to 4 (where "1" denotes the interface closest to the impactor and "5" denotes the interface closest to the distal surface of the plate). As the load increases, delamination

grows further and at 1 ms the delamination crack spans across interfaces 2,3 and 4, according to both the conventional CZM as well as the LCZ predictions. Delamination does not propagate beyond $t = 2.8$ms, which is the point in time when rebound of the impactor begins. At this state of fully developed delamination damage, only a slight difference is observed between the conventional CZ and the LCZ prediction. While the conventional CZ predicts delamination damage at interfaces 2,3,4 and 5, the LCZ method predicts delamination damage at all interfaces, including a relatively small area of delamination right under the point of contact with the spherical surface of the impactor, located at the first interface.

Figure 5.30.a and Figure 5.30.b show the impactor's kinetic energy, predicted by the conventional CZ method and the LCZ method, respectively. Both methods under-predict the kinetic energy when a single-cohesive-interface is used. This is probably a result of the unstable delamination crack propagation and decrease in the structural stiffness due to the size of the resulting crack. As the number of cohesive interfaces is increased, both conventional CZ and LCZ methods show an improvement in the kinetic energy prediction, where better convergence is achieved using the conventional CZ. In both methods, 5 interface models yield results which agree very well with the experimental findings.
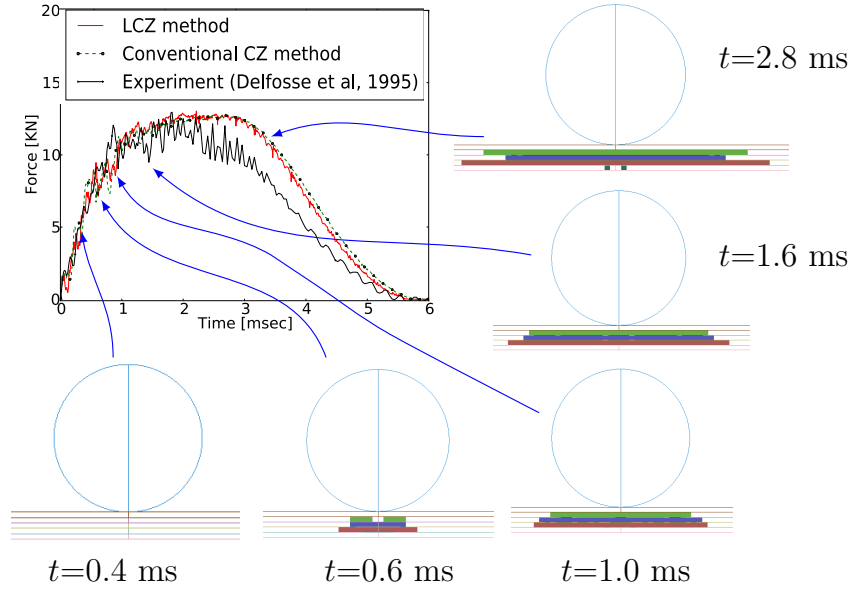
Figure 5.27: Delamination propagation predicted by the conventional CZ, for a 4.29 m/s, 6.33 kg projectile using a 5 interface model.
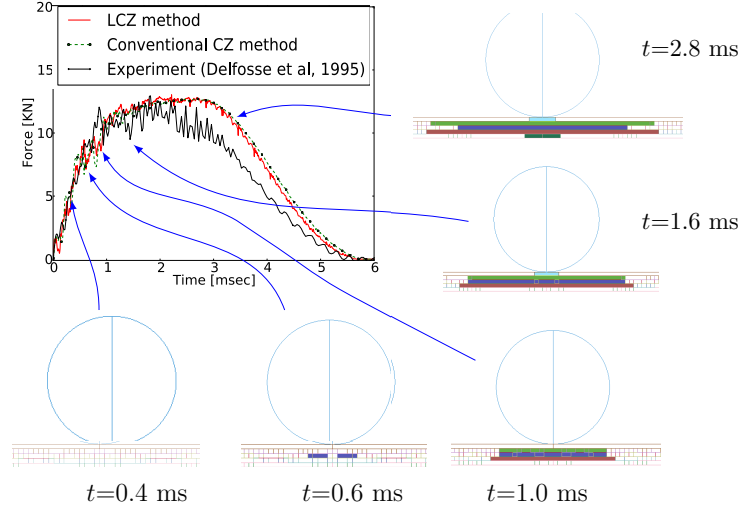
Figure 5.28: Delamination propagation predicted by the LCZ method, for a 4.29 m/s, 6.33 kg projectile using a 5 interface model.
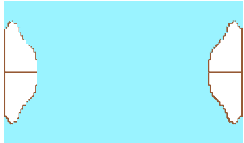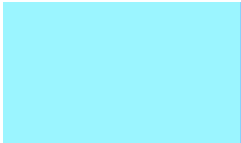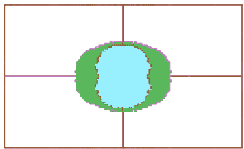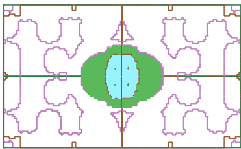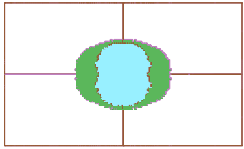
18.97 m/s Impact Event

Figure 5.31 and Figure 5.32 show the impact-force vs. time and impact-force vs. displacement profiles obtained from the simulations, respectively, for an impactor mass of 0.314 kg impacting the plate at 18.97 m/s. Table 5.8 shows the delamination patterns predicted by the conventional and LCZ method, as well as the image obtained from the experimental ultrasonic scan. Similar to the 4.29 m/s impact event, a single-cohesive interface results in a delamination crack growth which reaches the edges of the plate (Table 5.8). Increasing the number of cohesive interfaces to 3, 4 and 5 interfaces, will result in stable crack growth which better resembles the delamination damage found in the experiment. The oscillations which are noticeable in the impact force for all cases tested, are caused mainly by the natural oscillations of the plate which are driven by the dynamic impact event.

Figure 5.33 and Figure 5.34 show a schematic representation of the in-

Table 5.7: Predicted delamination patterns for a 4.29 m/s, 6.33 kg impactor, plate-impact event, obtained using the conventional CZ method, compared to the experimental and LCZ's method prediction. Fringe colors represent different through-thickness interfaces.

Number of through-thickness cohesive interfaces	Conventional CZ method	LCZ method
1		
3		
4		
5		
Experimental result [129]		

Figure 5.29: Projected delamination area, for an 6.33 kg impactor impacting the plate at 4.29 m/s, as a function of the number of through thickness cohesive interfaces, predicted by the Conventional CZ and LCZ methods, as well as the experimental results.

plane and delamination damage patterns for a time of 0.3 milliseconds and 1.3 milliseconds, respectively, obtained using a 3 cohesive interface model and the LCZ method. Initially, the plate is modelled using 3 through-thickness thick-shell elements. Assuming that delamination occurs in all of the potential interfaces, each thick shell element splits into two offset shell elements, thus resulting in plate consisting of of 6 offset shell elements through its thickness. The fringe plots located to the left side of Figure 5.33 and Figure 5.34 show the values of LS-DYNA's *MAT_81 damage parameter for each of the offset shell layers created during the splitting process, where a value of 1 resembles a fully damaged material, and a value of 0 resembles an undamaged material. The right side of Figure 5.33 and Figure 5.34 shows a schematic through-thickness place locator of each offset shell layers, together with the delamination damage of each of the three cohesive interfaces in the model. The largest delamination crack is predicted to take place within the second (middle) interface, while the in-plane damage

spans across a smaller region compared to the delamination damage of the neighbouring interfaces.

Figure 5.35 shows the predicted projected delamination area as a function of the number of through-thickness cohesive interfaces. Similar to the 4.29 m/s impact event, both of the conventional CZ, as well as the LCZ method over-predict the delamination area for the number of interfaces tested, and the LCZ method converges faster toward the experimental solution. Here, too, it is believed that the number of cohesive interfaces, which is lower in the numerical models compared to the actual experimental laminate architecture results in delamination cracks which cover a larger area.
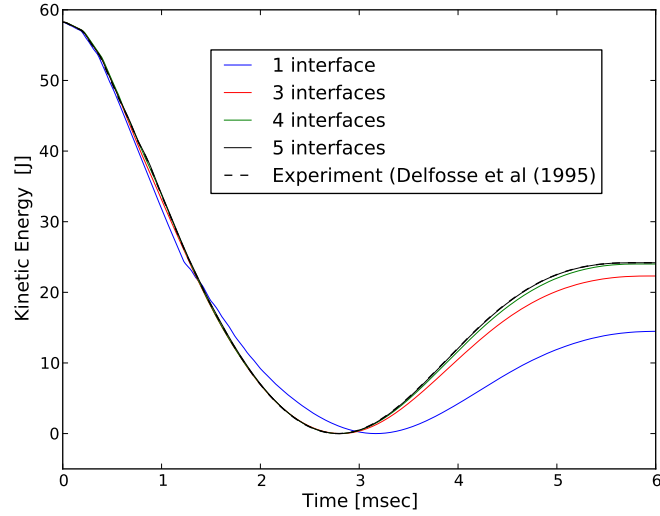
(a)
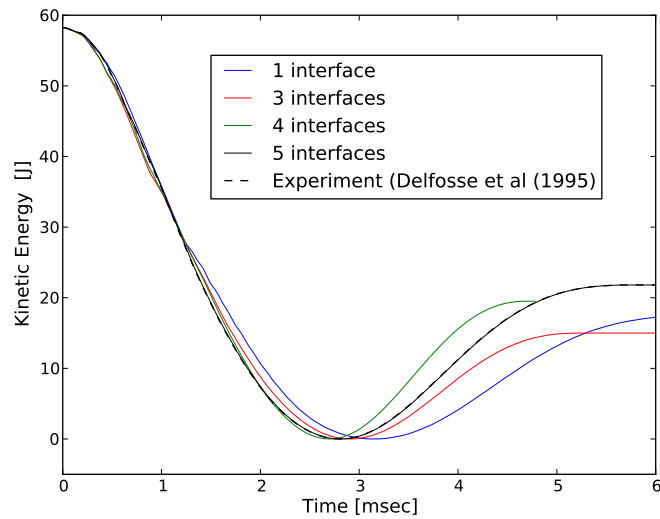
(b)

Figure 5.30: Predicted and experimental impactor's kinetic energy vs. time, for a 4.29 m/s impact velocity and impactor mass of 6.33 kg. **a).** The predicted results are shown for different number of through-thickness cohesive interfaces using the conventional CZM .**a).** Results obtained using the LCZ method
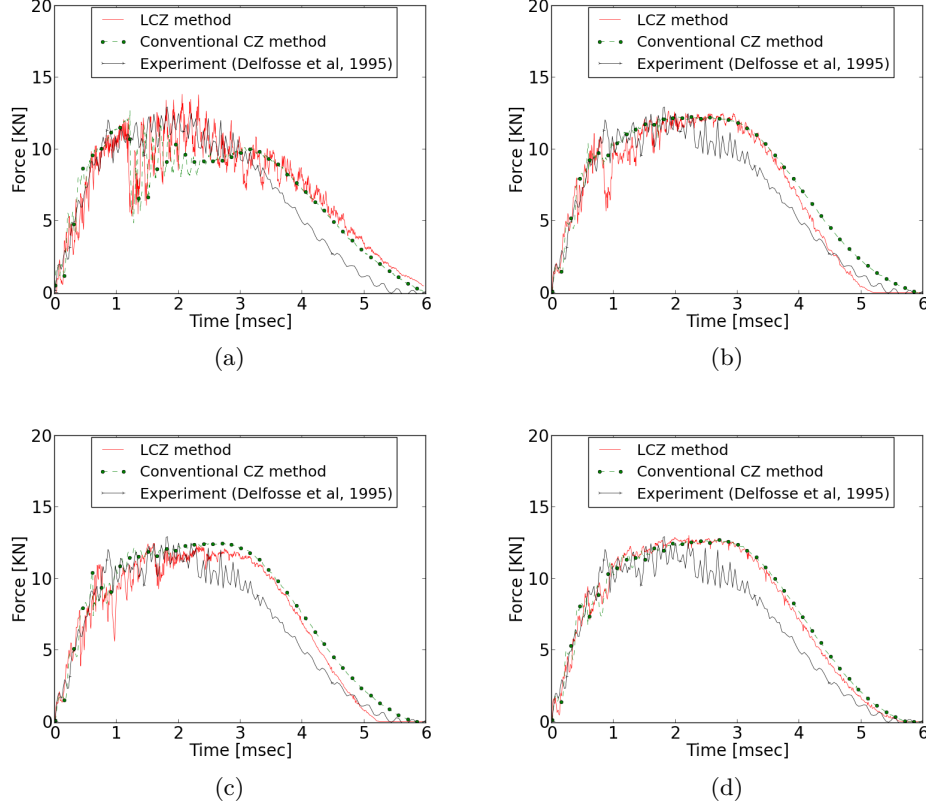
.

114
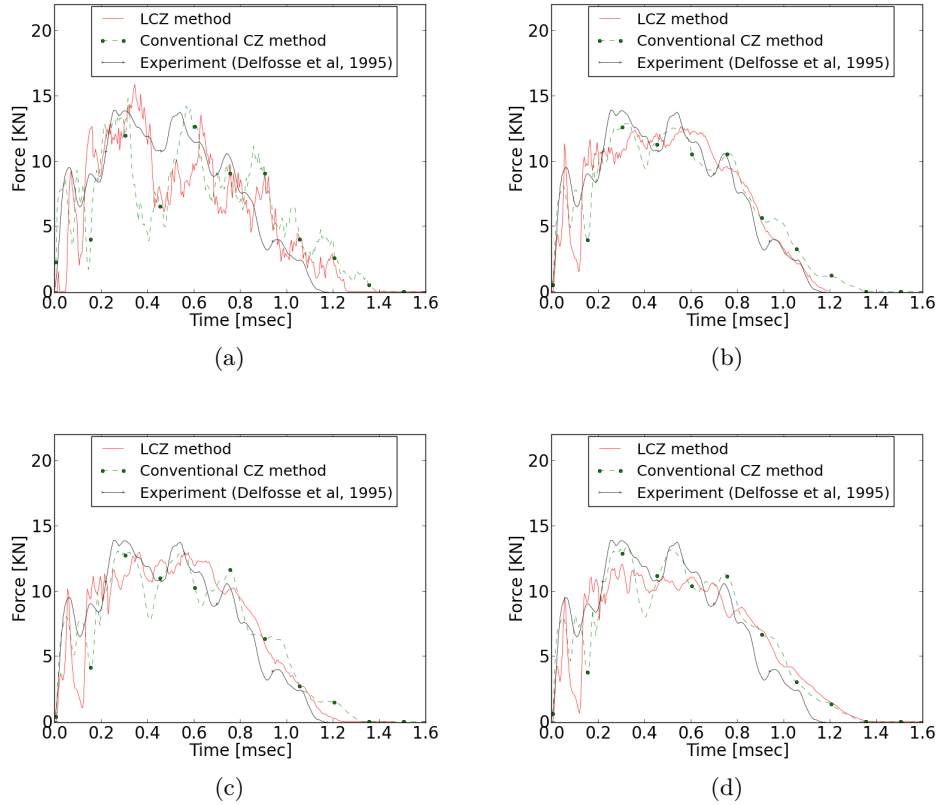
Figure 5.31: Predicted and experimental impact force vs. time for a 0.314 kg impactor, impacting the plate at 18.97 m/s. The numerical results were obtained using the LCZ method and the conventional CZM, for different number of through-thickness cohesive interfaces: **a).** 1 cohesive interface,**b).** 3 cohesive interfaces, **c).** 4 cohesive interfaces, **d).** 5 cohesive interfaces.
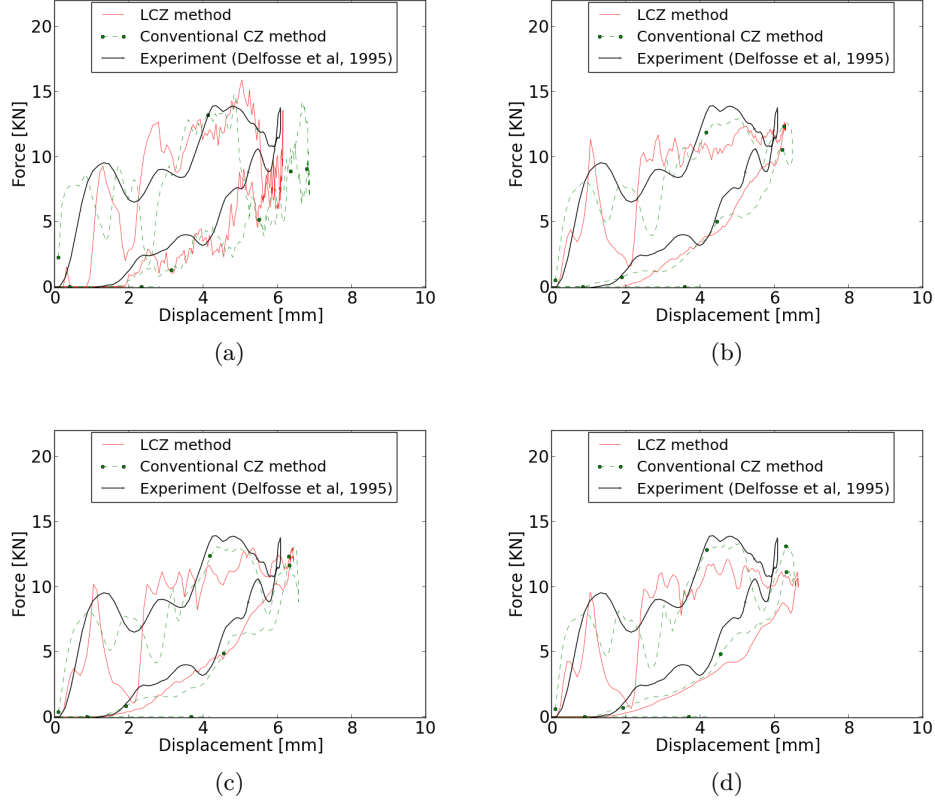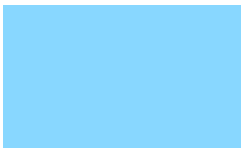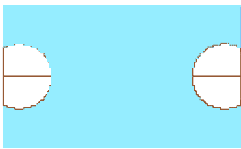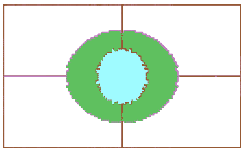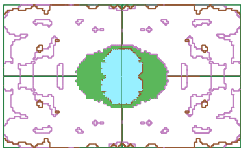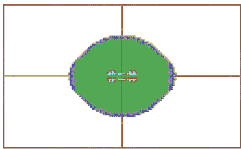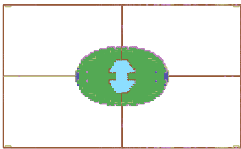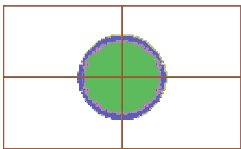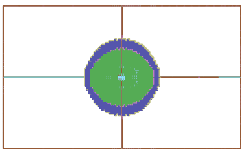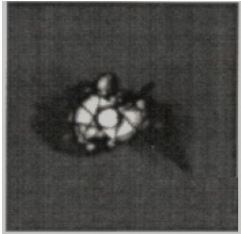
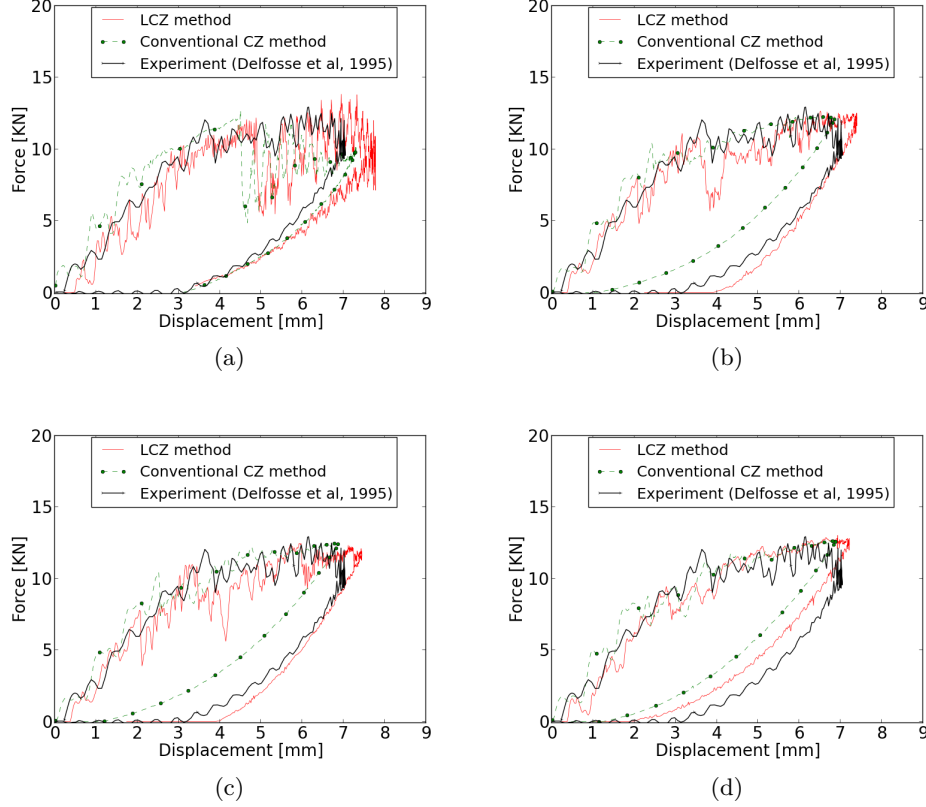Figure 5.32: Predicted and experimental impact force vs. plate displacement, for a 0.314 kg impactor, impacting the plate at 18.97 m/s. The numerical results were obtained using the LCZ method and the conventional CZM, for different number of through-thickness cohesive interfaces: **a).** 1 cohesive interface,**b).** 3 cohesive interfaces, **c).** 4 cohesive interfaces, **d).** 5 cohesive interfaces.

Table 5.8: Predicted delamination pattern for a 18.97 m/s, 0.314 kg projectile, plate-impact event, obtained using the conventional CZM, compared to the experimental and LCZ's method prediction. Fringe colors represent different through-thickness interfaces.

Number of through-thickness cohesive interfaces	Conventional CZ method	LCZ method
1		
3		
4		
5		
Experimental result [129]		

Figure 5.33: Damage in a 3 interface model, impact velocity of 18.97 m/s, at time of 0.3 ms.

Figure 5.36.a and Figure 5.36.b show the impactor's kinetic energy, predicted by the conventional CZ method and the LCZ method, respectively. Except for the case where the LCZ method was used to solve a 5 interface model, all models tested resulted in under-prediction of the impactor's kinetic energy. When the LCZ method was used, increasing the number of cohesive interfaces in the finite element model lead to better convergence of the results. This trend was less pronounced when the conventional CZ method was applied to the problem, where the improvement of the results was either negligible or even worsened by an increased number of interfaces (A 3 interface model yielded inferior results compared to a single interface model).
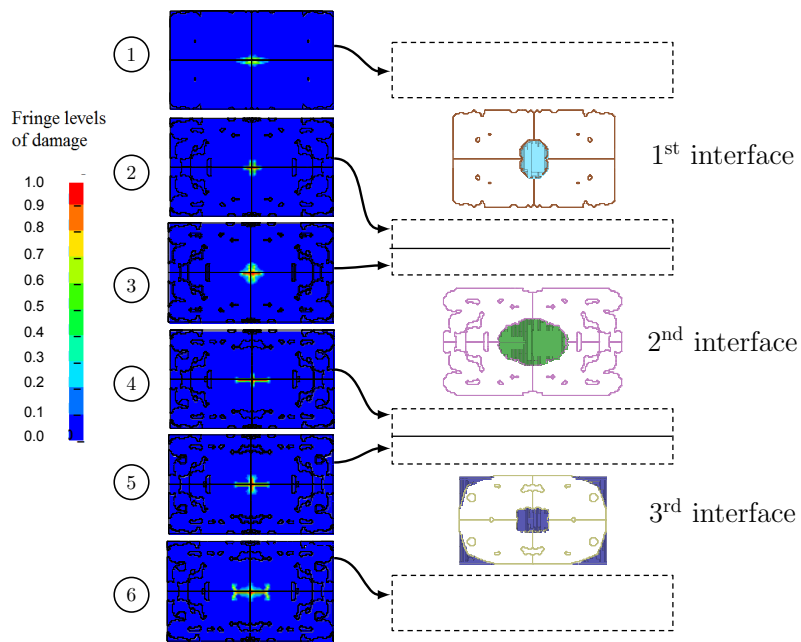
Figure 5.34: Damage in a 3 interface model, impact velocity of 18.97 m/s, at time of 1.8 ms.
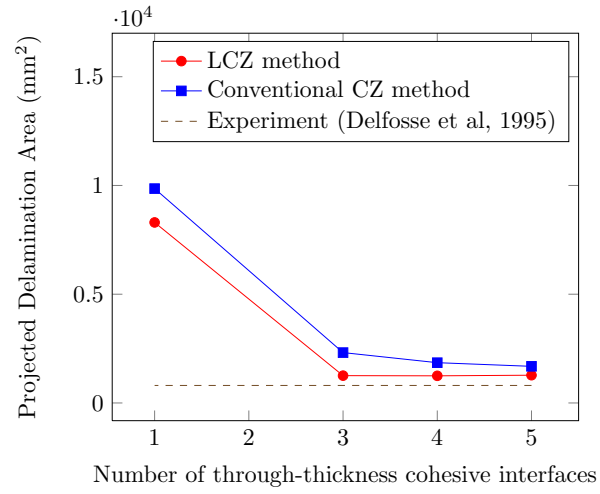
Figure 5.35: Projected delamination area, for an 0.314 kg impactor impacting the plate at 18.97 m/s, as a function of the number of through thickness cohesive interfaces, predicted by the Conventional CZ and LCZ methods, as well as the experimental results.
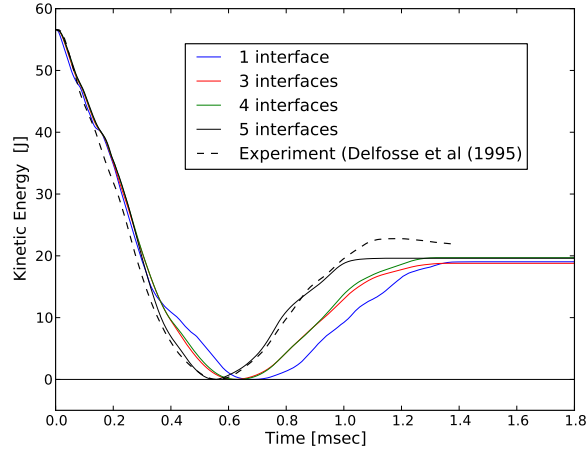
(a)
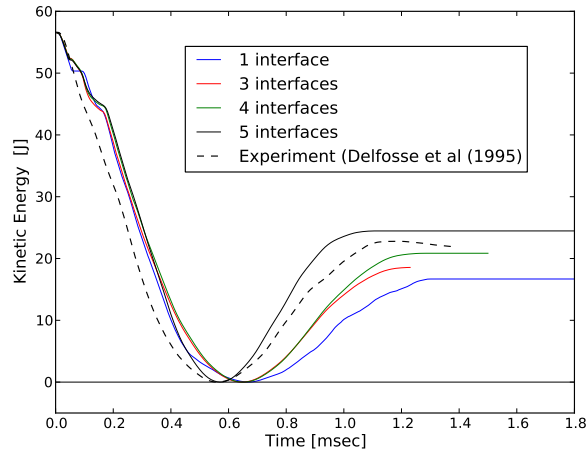
(b)

Figure 5.36: Predicted and experimental impactor's kinetic energy vs. time, for a 18.97 m/s impact velocity and impactor mass of 0.314 kg. **a).** The predicted results are shown for different number of through-thickness cohesive interfaces, using the conventional CZM. **b).** Results obtained using the LCZ method.

14.59 m/s Impact Event

Figure 5.37 and Figure 5.38 show the impact-force vs. time and impact-force vs. displacement profiles obtained from the simulations, respectively, for an impactor mass of 0.314 kg impacting the plate at 14.59 m/s. Table 5.9 shows the delamination patterns predicted by the conventional and LCZ method, as well as the image obtained from the experimental ultrasonic scan, and Figure 5.39 show the impactor's kinetic energy as a function of time. The force vs. time profiles show good agreement with the experimental data, for both the conventional CZ as well as the LCZ method's solution. The force vs. displacement plots show lower agreement, particularly for the single cohesive interface models, where overall the numerical predictions under-predict the impact force. As with all other plate impact scenarios tested, using a single cohesive interface to describe the plate, results in an unstable delamination crack growth, yielding a crack that reaches the plate's boundaries (Table 5.9). However, the divergence of the LCZ solution's prediction from the experimental findings is smaller compared to the results predicted by the conventional CZ method. Figure 5.40 shows the predicted projected delamination area depending on the number of through-thickness cohesive interfaces. Similar to all other cases tested, it can be seen that the conventional CZ, as well as the LCZ method, over-predict the delamination area for the number of interfaces used and that both converge to the experimental value as the number of interfaces increases, with the LCZ method requiring fewer number of interfaces for convergence.

It is believed that the number of cohesive interfaces throughout the thickness which is lower in the numerical models than the actual number of interfaces results in delamination cracks which cover a larger area.
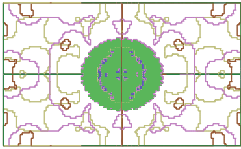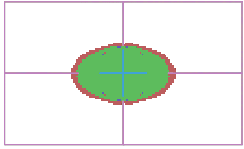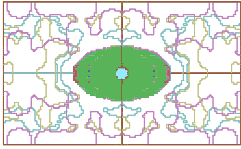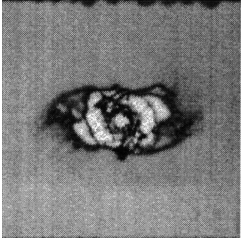
Figure 5.39 shows the impactor's kinetic energy as a function of time. The final predicted kinetic energy of the impactor (Figure 5.39), converges to the experimental result with an increased number of cohesive interfaces, for both of the LCZ and conventional CZ method's predictions.

5.4 Summary and Conclusions

The LCZ method, which was verified for the solution of pure delamination crack propagation in Chapter 4, was applied here for the solution of a tensile loading of a double-notched coupon, dynamic tube crushing experiments, as well as dynamic plate impact events.

For the tensile loading of the double-notch coupon, the method was combined with LS-DYNA's `*MAT_54`, to capture the in-plane behavior
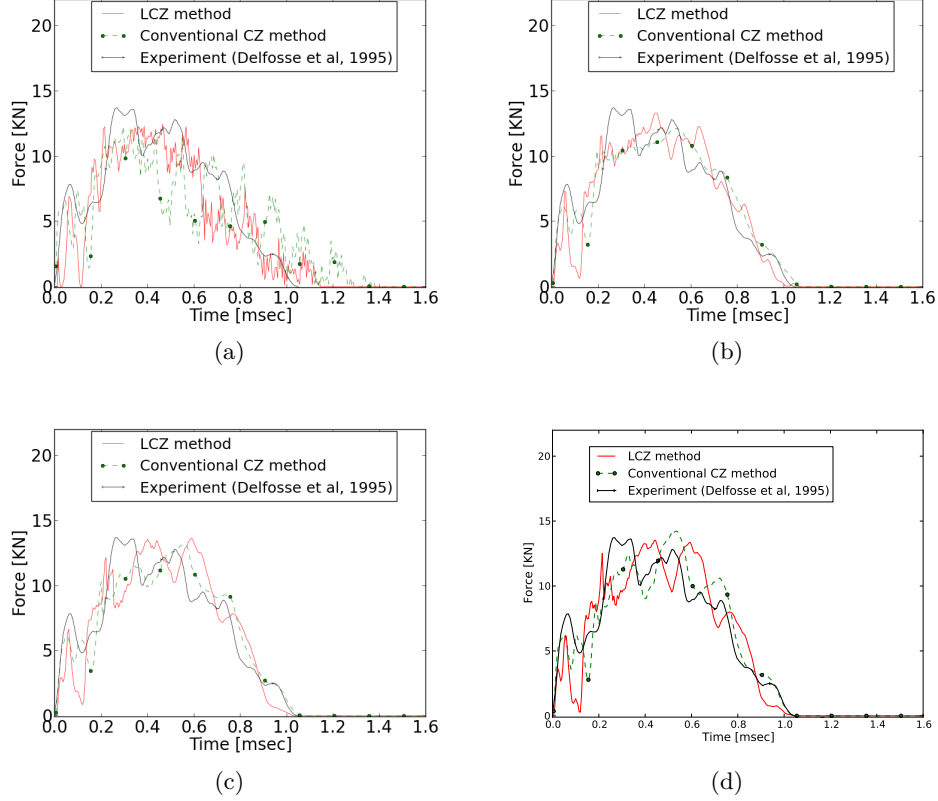
Figure 5.37: Predicted and experimental impact force vs. time for a 0.314 kg impactor, impacting the plate at 14.59 m/s. The numerical results were obtained using the LCZ method and the conventional CZM, for different number of through-thickness cohesive interfaces: **a).** 1 cohesive interface, **b).** 3 cohesive interfaces, **c).** 4 cohesive interfaces, **d).** 5 cohesive interfaces.

and overall strength reduction of the coupon, such that both in-plane as well as out of plane damage could be simulated simultaneously.

For the tube crush loading scenario, a continuum damage model developed at the University of British Columbia (CODAM2), was applied to capture the in-plane damage within the tube's wall, and the LCZ method was applied to the model in order to capture interlaminar damage. Impact-force profiles were compared to the experimental data, as well as to results obtained using the conventional CZM. Good agreement was obtained for
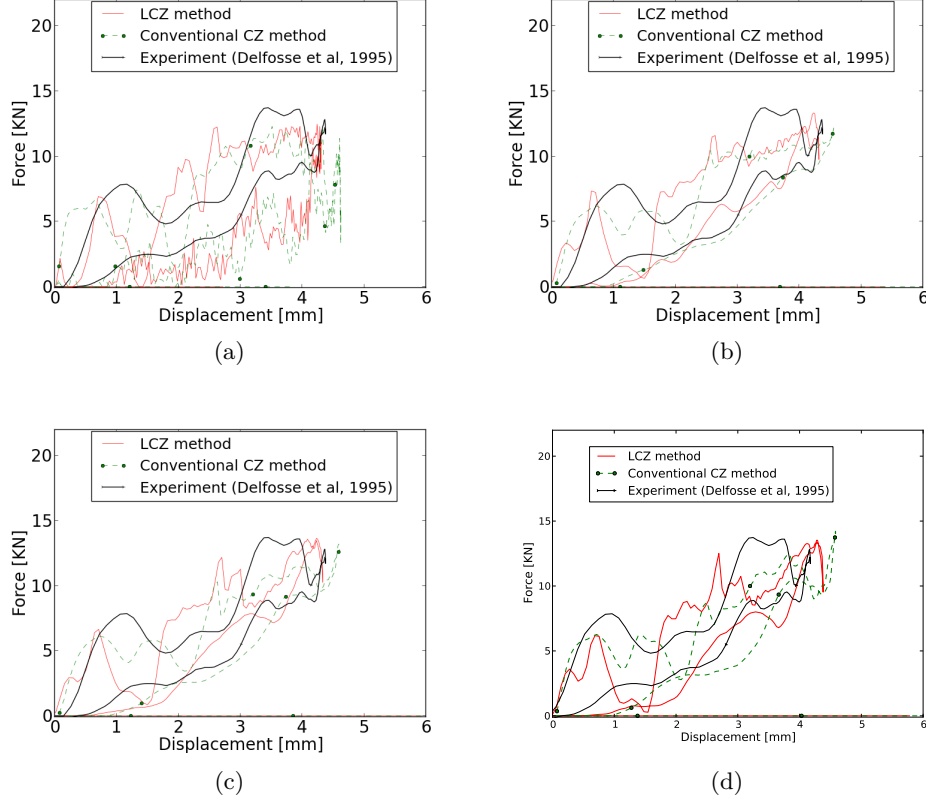
Figure 5.38: Predicted and experimental impact force vs. plate displacement, for a 0.314 kg impactor, impacting the plate at 14.59 m/s. The numerical results were obtained using the LCZ method and the conventional CZM, for different number of through-thickness cohesive interfaces: **a).** 1 cohesive interface,**b).** 3 cohesive interfaces, **c).** 4 cohesive interfaces, **d).** 5 cohesive interfaces.

both numerical methods compared to the experiments. Slight differences were observed between the prediction of damage using the two numerical approaches. The LCZ algorithm was able to adaptively split the structural elements through their thickness during the dynamic tube-crushing process, and seed the cohesive elements along the required locations.

A new capability of the LCZ method, which allows adaptive introduction of multiple through-thickness delamination cracks into the structure,
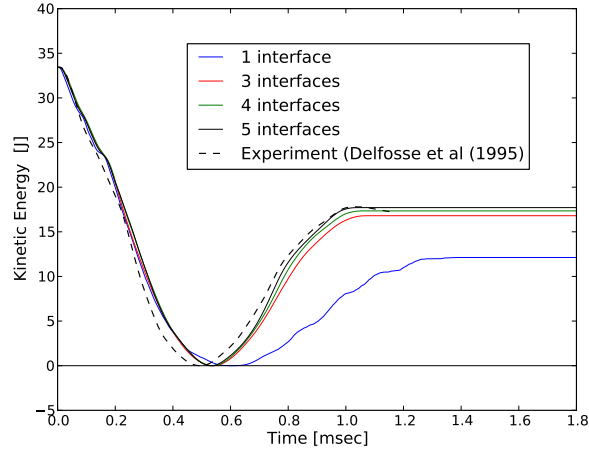
(a)
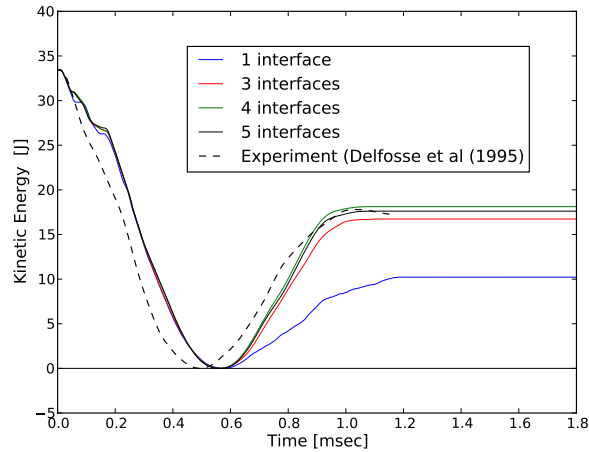
(b)

Figure 5.39: Predicted and experimental impactor's kinetic energy vs. time, for a 14.59 m/s impact velocity and impactor mass of 0.314 kg. **a).** The predicted results are shown for different number of through-thickness cohesive interfaces, using the conventional CZM. **b).** Results obtained using the LCZ method.
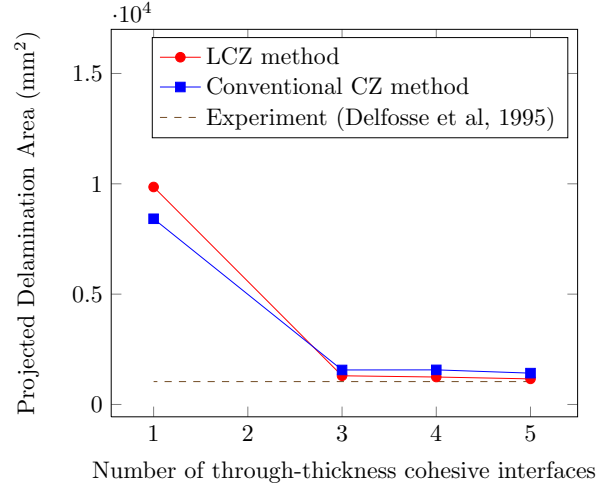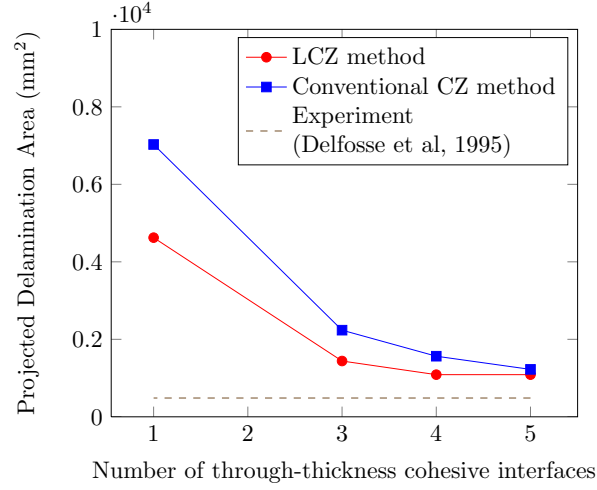
Figure 5.40: Projected delamination area, for an 0.314 kg impactor impacting the plate at 14.59 m/s, as a function of the number of through-thickness cohesive interfaces, predicted by the Conventional CZ and LCZ methods, as well as the experimental results.

was applied to a plate-impact event used as a benchmark problem. The test configuration was modelled using various number of through-thickness cohesive interfaces, and the problem was solved using both the LCZ method, as well as the conventional CZ method. Impact-force vs. displacements profiles, as well as impact force vs. time histories, were compared to the experimental data, together with the impactor's kinetic energy, predicted delamination patterns, and predicted delamination area. The results were presented for three impact velocities and different values of the impactor mass.

For the range of velocities tested, the impact force profiles obtained from the numerical simulations were with reasonable agreement of the experimental data, for 3, 4, and 5 through-thickness cohesive interfaces. Good results was obtained from the LCZ method, as well as the conventional CZ method. When a single cohesive interface was used, the delamination crack propagated in an unstable manner, for both conventional CZ as well as the LCZ

solution. This is believed to be caused by the insufficient through-thickness discretization of the finite element model, which requires a larger area of delamination crack to be formed in order to absorb enough energy by this damage mechanism. The through-thickness discretization is believed to have an effect on the projected delamination area, which although resembled the experimental pattern for all number of through-thickness cohesive interfaces tested, covered a larger area in the simulations compared to the experimental results. Increasing the number of cohesive interfaces in order to evaluate this assumption was not performed in this study, as it will result in a finite element model which exceeds the number of interfaces found in the experimental setup, given that each sublaminate is treated as an isotropic and homogenized material.

Kinetic energy profiles of the impactor were with reasonable agreement of the experimental data, for all cases tested, for both LCZ simulation as well as the numerical solution obtained using the conventional CZM. Increasing the number of cohesive interfaces improved the results for both numerical methods.

The work performed here proved the ability of the LCZ method to be combined with other in-plane damage theories, where intra-laminar damage is treated in a smeared manner, and the element stiffness is reduced gradually as a function of damage evolution within the finite element volume. Such methodology combines the numerical advantages of smeared modelling techniques with the need to model delamination in a discrete manner.

The numerical advantages and performance of the method will be discussed in the next chapter.
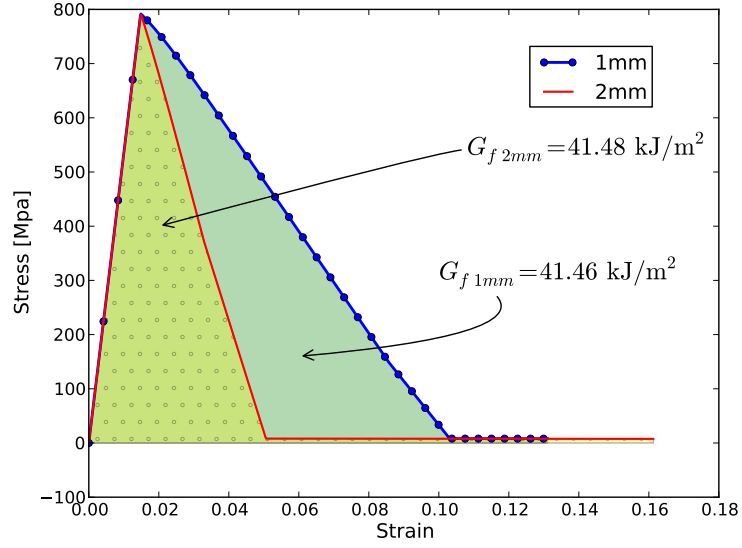
Figure 5.41: Stress vs. strain for plate impact model, 2mm and 1mm mesh
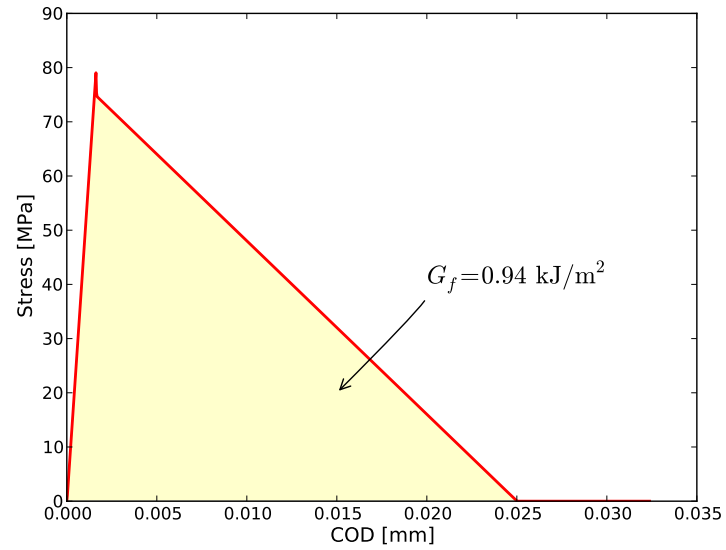
Figure 5.42: Stress vs. COD obtained from Tie-Break contact, Mode-I crack opening
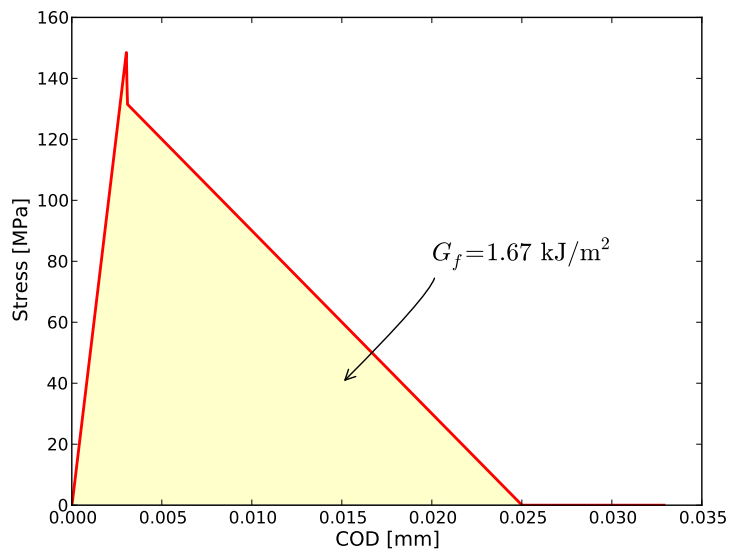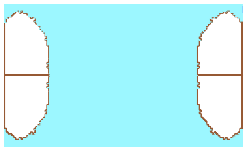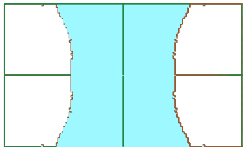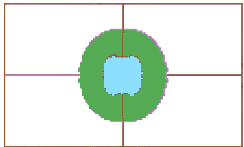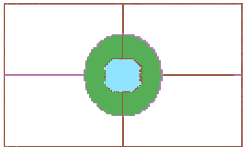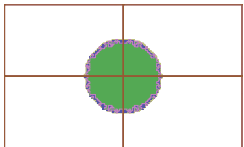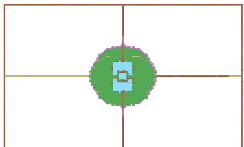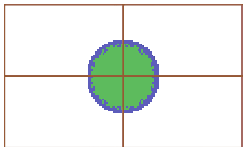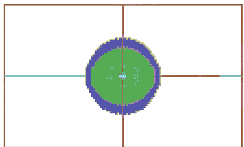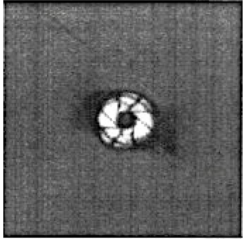
Figure 5.43: Stress vs. COD obtained from Tie-Break contact, Mode-II crack opening

Table 5.9: Predicted delamination pattern for a 14.59 m/s, 0.314 kg projectile, plate-impact event, obtained using the conventional CZM, compared to the experimental and LCZ's method prediction.

Number of through-thickness cohesive interfaces	Conventional CZ method	LCZ method
1		
3		
4		
5		
Experimental result [129]		

Chapter 6

Numerical Performance of the LCZ method

6.1 Introduction

In line with the motivation for the development of the LCZ method, and taking into account the fact the the LCZ algorithm is not yet an internal part of a commercial finite element code, some preliminary simulations were performed in order to evaluate the numerical performance of the algorithm compared to the conventional CZM. The following sections will describe the performance of the LCZ method and its efficiency when solving larger models, and its overall effect on the structural stiffness.

6.2 Solution of Larger Models

Solving larger models using the conventional CZM, often requires large number of numerically-expensive cohesive interfaces to be present in the model, which can increase the computational load to an extent which renders this method inapplicable to large engineering applications. Using the LCZ method, however, requires no cohesive elements to be present in the model a priori of the finite element analysis, as they are seeded only at specific locations where delamination has the potential to initiate and grow. In order to compare the numerical efficiency of the LCZ method with respect to the conventional CZM, a series of numerical models with increased number of elements, were solved. These models were based on the tube-crush model - for each model tested, the tube portion of the model was duplicated, where each model had a different number of tube duplications. Models containing 2, 6 and 10 tubes are shown in Figure 6.1.a, Figure 6.1.b, and Figure 6.1.c, respectively. It is important to note that only the tube portion of the model was duplicated, i.e, only a single plug and dropped mass was used in each of the models, thus in each of the models tested, only a single tube was undergoing active crushing.

The models were then solved using six CPUs for each model. Given the fact that the LCZ algorithm is currently in a development state and is not an integrated part of LS-DYNA, only the actual LS-DYNA run-time obtained from solving the models using the LCZ algorithm was compared to the LS-DYNA run-time using the conventional CZM.

The resulting LS-DYNA run-time, in seconds, for each of the models solved, is listed in Table 6.1. The ratio between the LS-DYNA run-time using the conventional application of CZM (using solid cohesive elements a-priori seeded along all of the cohesive interfaces), t_{conv}, and the LS-DYNA run-time using the LCZ method t_{LCZ}, is plotted vs. the number of tubes in the model in Figure 6.2. Even for a single tube model, the LS-DYNA run-time using the conventional cohesive-zone method is 1.79 times longer than the run-time using the LCZ method, where for a model containing 10 tubes, the ratio between the run-times of the two methods is 5.4 in favour of the LCZ method.

<center>(a)   (b)   (c)</center>
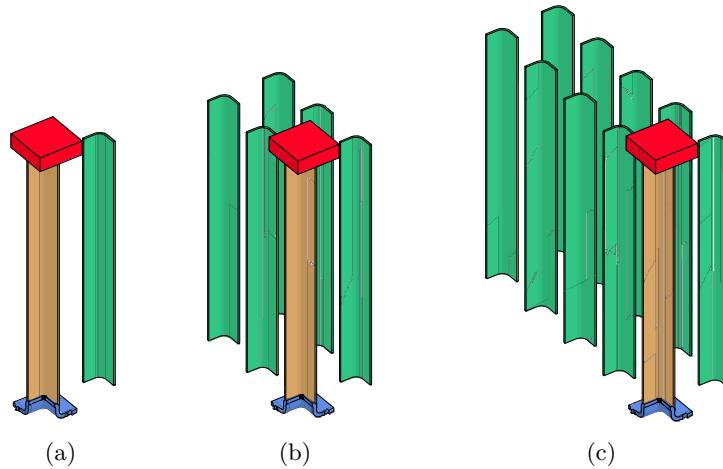
Figure 6.1: Isometric view of three finite element models used to test the LCZ method's efficiency over the conventional CZM, using increasing number of tubes: **a).** Two tubes. **b).** Six tubes. **(c)** Ten tubes.

To compare the efficiency of the LCZ method (which is based on solid cohesive elements as the numerical representation of the cohesive interface) against the conventional CZM using a cohesive contact interface, the simulations for the conventional CZM were repeated using a cohesive contact algorithm (LS-DYNA's TIEBREAK contact) replacing all of the solid cohe-

Table 6.1: LS-DYNA run-time in seconds, using solid cohesive elements, obtained using the conventional CZM, as well as using the LCZ method. The ratio between the LS-DYNA run-time using both methods is presented as well.

	Number of tubes					
	1	2	4	6	8	10
Conventional cohesive-zone method (t_{conv})	52,371	85,188	193,500	214,225	339,976	483,520
LCZ method (t_{LCZ})	29,300	51,307	79,342	81,023	79,241	89,502
t_{conv}/t_{LCZ}	1.79	2.07	2.7	3.12	4.3	5.4

sive elements in the model. The LS-DYNA resulting run-time, in seconds, for each of the models solved, is listed in Table 6.1. The ratio between the LS-DYNA run-time using the conventional application of CZM (using a co-hesive contact algorithm a-priori defined along all of the cohesive interfaces in the model), t_conv, and the LS-DYNA run-time using the LCZ method, is plotted vs. the number of tubes in the model in Figure 6.3. For a single tube model, the LS-DYNA run-time using the conventional cohesive-zone method is 1.73 times longer than the run-time using the LCZ method. As the number of tubes is further increased, a meandering trend can e noticed. It is believed that the internal treatment of the contact algorithm within the finite element solver is the main cause for the slight decrease in the efficiency for some of the cases tested. For all cases tested, however, the run-time using the LCZ method was considerably shorter compared to the run-time using the conventional CZM.

Table 6.2: LS-DYNA run-time in seconds obtained using the conventional CZM, together with a TIEBREAK contact algorithm, and the LS-DYNA run-time using the LCZ method with solid cohesive elements. The ratio between the LS-DYNA run-time using both methods is presented as well.

	Number of tubes					
	1	2	4	6	8	10
Conventional cohesive-zone method (t_{conv})	50,762	85,188	161,026	231,630	308,147	376,564
LCZ method (t_{LCZ})	29,300	51,307	79,342	81,023	79,241	89,502
t_{conv}/t_{LCZ}	1.73	1.66	3.02	2.86	3.90	4.21
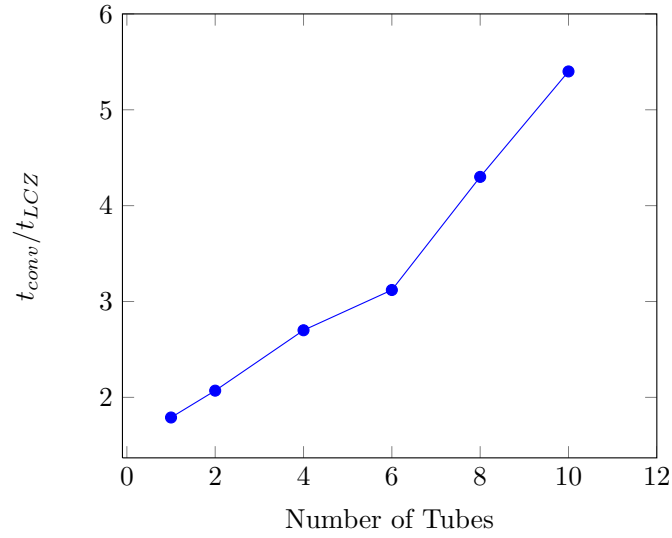
Figure 6.2: Ratio between the LS-DYNA run-time using the conventional application of CZM (using solid cohesive elements a-priori seeded along all of the cohesive interfaces), t_{conv}, and the LS-DYNA run-time using the LCZ method, t_{LCZ}, vs. the number of tubes in the models.
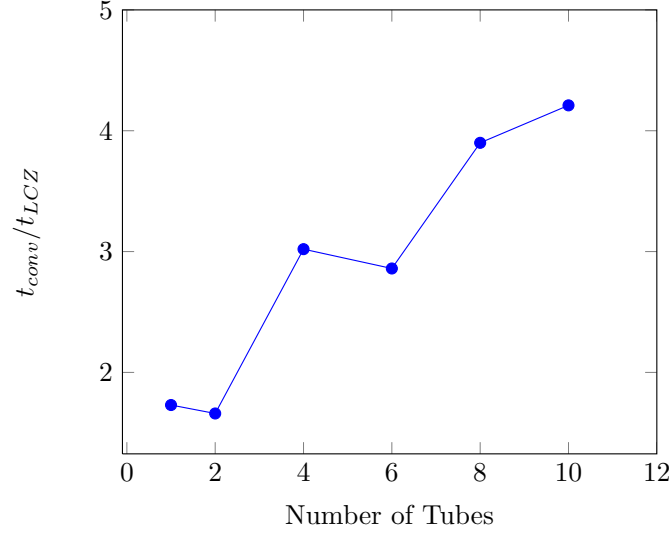
Figure 6.3: Ratio between the LS-DYNA run-time using the conventional application of CZM using a cohesive contact algorithm along all of the cohesive interface, t_{conv}, and the LS-DYNA run-time using the LCZ method, t_{LCZ}, vs. the number of tubes in the models.

6.3   Effect of CZM on the Structural Stiffness

Since the use of CZM in its standard form requires introduction of large number of cohesive elements in all possible locations where delamination is likely to grow, using this method to predict delamination crack growth in large structures is not practical from the numerical standpoint. In their work, Kaliske et al. [62] investigated the effect of the CZM on the numerical complexity of a finite element model. It was shown that for a two dimensional uniform finite-element mesh consisting of 4-node elements (Figure 6.4.a), introducing cohesive interfaces in all possible crack-growth paths can lead to a 4-times increase in the number of DOF within the model (Figure 6.4.b). Furthermore, using cohesive elements in wide regions of the model will artificially render the structure more compliant. This is demonstrated

in Figure 6.5, where a schematic 3D model consisting of two continuum elements with an initial thickness t, which are connected to each other using a cohesive interface of an initial zero thickness is loaded normal to the cohesive interface. Once a load F is applied, (Figure 6.5.b), the continuum elements deform to a thickness $t + \delta t$, and the cohesive interface opens to a displacement Δ. In this loaded state, the traction continuity requires that:

$$\sigma = E_3 \varepsilon = K\Delta \tag{6.1}$$

where σ is the stress resulting from the applied force F, E_3 is the continuum element's Young's modulus in the normal (out-of-plane) direction, ε is the strain of the continuum element, and K is the stiffness of the cohesive interface.

The effective strain, ε_{eff}, of the material is:

$$\varepsilon_{eff} = \frac{\delta t}{t} + \frac{\Delta}{t} = \varepsilon + \frac{\Delta}{t} \tag{6.2}$$

Combining Equation 6.1 and Equation 6.2 yields:

$$\varepsilon_{eff} = E_3 \left(\frac{1}{1 + \frac{E_3}{Kt}} \right) \tag{6.3}$$

Thus, in order for the cohesive interface stiffness to have a lower effect on the effective stiffness of the laminate, the condition $E_3 << Kt$ needs to be satisfied. Since E_3 and t are given material and geometrical properties, and the sublaminate thickness t is generally small (on the order of tenths of millimetres), this implies that in order to reduce the unwanted compliance introduced to the model by the cohesive interface, the cohesive stiffness needs to be much higher than the stiffness of the sublaminate plies. However, large values of the interface stiffness may cause numerical noise and loss of stability [115].
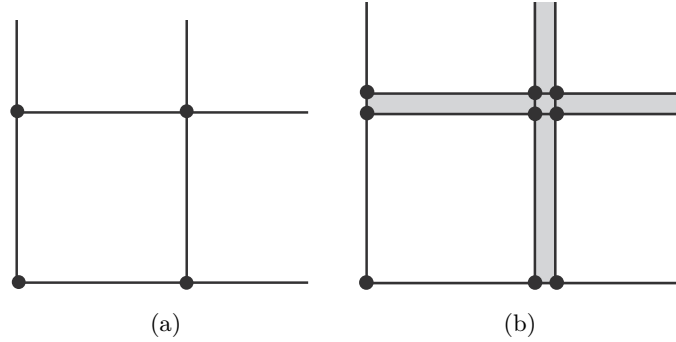
Figure 6.4: A simple finite-element topology demonstrating the increase of numerical complexity when cohesive elements are introduced into the model. **a.)** A simple 2D model consisting of 4-node elements. **b.)** Cohesive elements are introduced in between the continuum elements, shown here in darker shade.
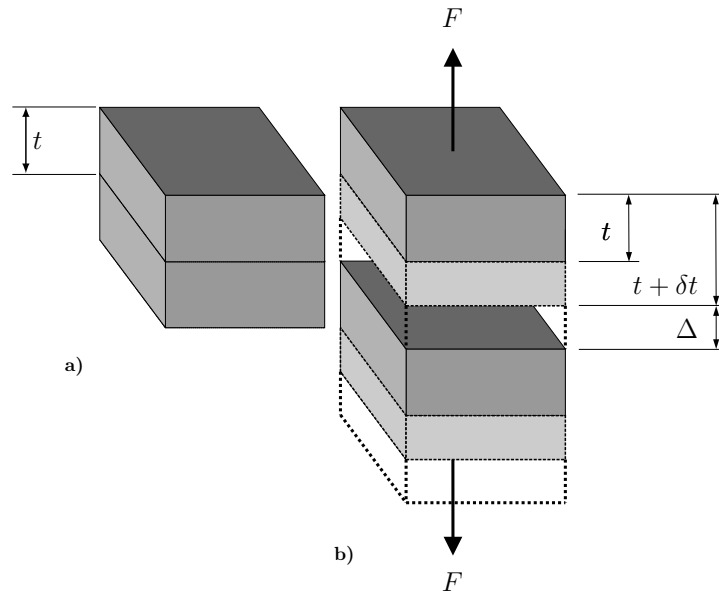
Figure 6.5: Schematic 3D model demonstrating the behavior of a cohesive interface. **a.)** Two continuum elements with an initial thickness t, connected to each other using a cohesive interface of an initial zero thickness, are shown in this figure in an unloaded state. **b.)** Once a load F is applied normal to the cohesive interface, the continuum elements deform to a thickness $t + \delta t$, and the cohesive interface opens to a displacement Δ.

6.3.1 Simply Supported Beam Under Bending Load

The effect of the CZM on the structural stiffness of a simply supported beam was investigated. The model geometry is shown in Figure 6.6. A simply supported beam of length $2L = 99$ mm, thickness $h = 3$ mm, and width of 1 mm, is subjected to a 1 mm displacement Δ in the negative z direction, which is applied at the center of the beam. Three beam configurations were numerically tested: the first, which is shown is Figure 6.7.a, consists of a beam having no cohesive interfaces within the finite element model. The second configuration, shown in 6.7.b, consists of 5 cohesive interfaces through the thickness of the beam, with solid cohesive elements located along all potential delamination crack paths within the interfaces. The cohesive interfaces were modelled using LS-DYNA's *MAT COHESIVE GENERAL is applied, and are shaded in brown color. The third configuration, shown in Figure 6.7.c, consists of two 15 mm long cohesive interfaces, locally placed along the edges of the beam. Each configuration was solved using 2, 6 and 18 through-thickness thick-shell elements. The beam was modeled using an isotropic elastic material model (*MAT ELASTIC), using the properties listed in Table 6.3. A typical element size of 1 mm was used along the axial direction of the beam. The through-thickness element size was determined based on the configuration and element discretization described above.
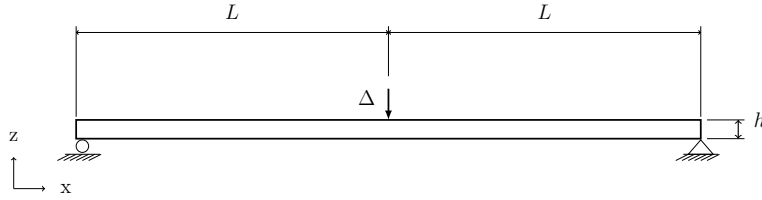
Figure 6.6: Simply supported beam of total length $2L = 99$ mm, thickness $h = 3$ mm, and width of 1 mm. A displacement Δ, in the global negative z direction, is applied at the center of the beam.

The predicted load at 1 mm displacement as a function of the cohesive topology and number of through-thickness discretization, is shown in Figure 6.8. The dashed line represents the analytical solution. It can be seen that the numerical models containing two through-thickness elements (thus a single cohesive interface), yielded results which are close to the analyti-

cal solution, for all cohesive configurations tested. Increasing the number of through-thickness elements from 2 to 6 (thus increasing the number of through-thickness cohesive interfaces from 1 to 5), resulted in a decrease of the structural stiffness, for the case where the conventional CZM was used. Further reduction of stiffness occurred as the number of through-thickness elements increased from 6 to 18 (increasing the number of through-thickness cohesive interfaces from 5 to 17). Localizing the cohesive interface along the edge of the beam did not decrease the peak force, for any of the configurations tested.

Table 6.3: Isotropic material and interface properties for the simply-supported beam benchmark problem.

Property	Value	Unit
Density (ρ)	1.543×10^{-3}	g/mm^3
Elastic Properties		
Elastic modulus ($E_{xx} = E_{yy} = E_{zz}$)	150	GPa
Poisson ratios ($\nu_{xy} = \nu_{yz} = \nu_{xz}$)	0.32	(-)
Interlaminar properties		
Mode I critical energy release rate (G_{Ic})	0.8	kJ/m^2
Mode II critical energy release rate (G_{IIc})	2.0	kJ/m^2
Interlaminar normal strength (σ_{max})	80	MPa
Interlaminar shear strength (τ_{max})	150	MPa

6.3.2 Static Plate Loading

In order to investigate the effect of the LCZ method on the structural stiffness of a plate under a bending load, a finite element model, similar to the plate-impact model described and solved in Section 5.3, was quasi statically loaded by prescribing a 1 mm displacement to the spherical impactor. The value of all material and cohesive parameters, remained identical to the values used in the plate-impact simulations described in Section 5.3. The model was solved using the LCZ method, as well as the conventional CZM.

(a)

(b)

(c)
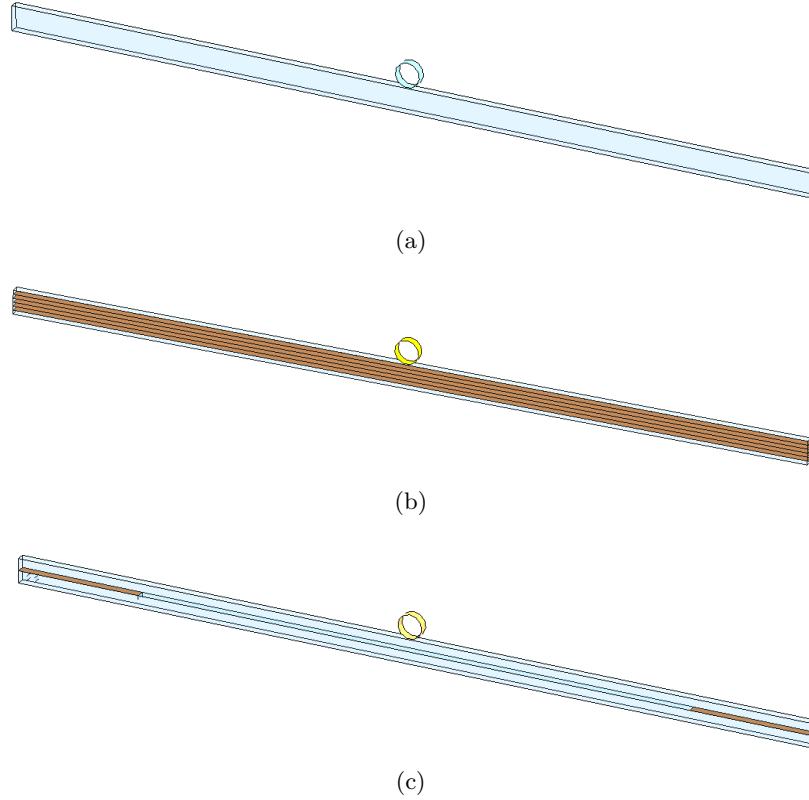
Figure 6.7: Isometric view of simply supported beam, modeled using three different configurations. Cohesive interfaces are shaded in brown color: **a).** No cohesive interface is present **b).** 5 through-thickness cohesive interfaces, distributed along all potential delamination crack-paths **c).** 4 cohesive interfaces **d).** Local cohesive interface model, concisting of two 15 mm long cohesive interfaces located at both ends of the beam.

Several models were tested, with increasing number of through-thickness cohesive interfaces. For comparative purposes, additional models containing no cohesive interfaces were solved as well. These models contained increasing number of through-thickness thick-shell elements, without any cohesive interfaces present.

The load at 1 mm displacement for each of the models, as a function of the number of through-thickness cohesive interfaces, as well as a function of the number of through-thickness thick-shell elements, is shown in Figure 6.9. It
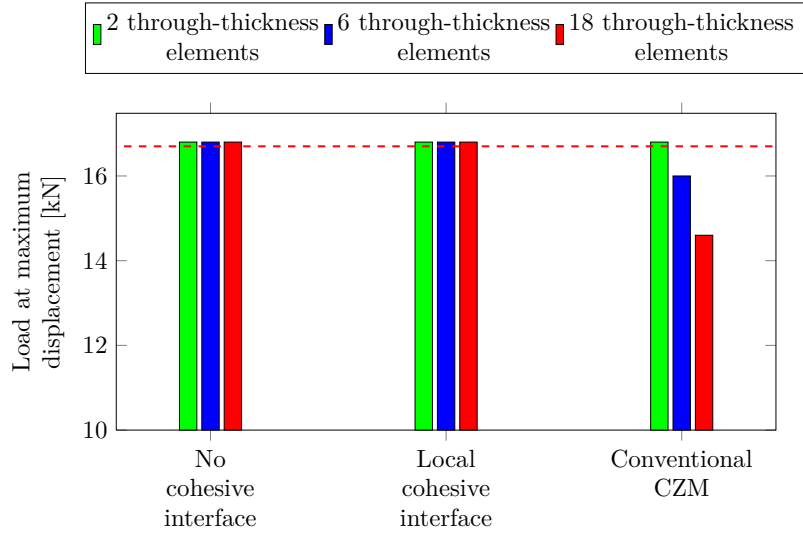
Figure 6.8: Load at maximum displacement for a simply-supported beam under central bending load, as a function of the cohesive topology and number of through-thickness elements. Dashed line represents the analytical solution.

can be seen that the stiffness reduction using the LCZ method is negligible, where an noticeable stiffness reduction is exhibited by the conventional CZ method's results for the range of models tested.
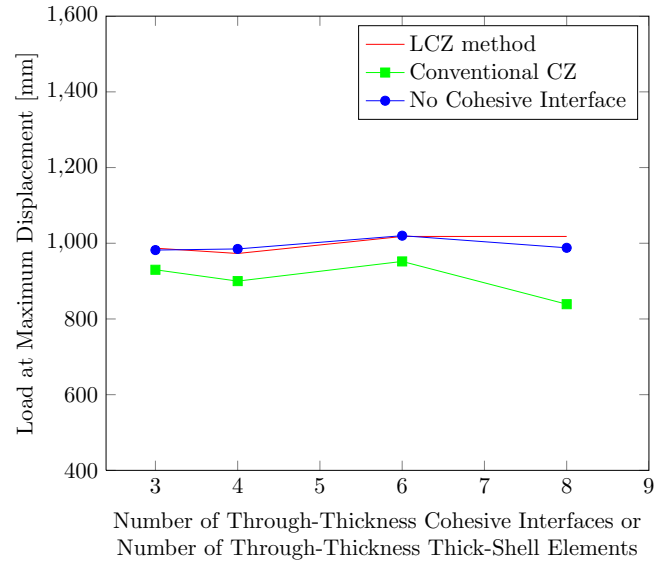
Figure 6.9: Load at maximum displacement for the plate bending example, as a function of through-thickness discretization and numerical solution method.

6.3.3   Dynamic Plate Impact

In order to compare the effect of the LCZ method to cohesive interfaces defined using a cohesive contact algorithm, the dynamic plate-impact simulations described in Section 5.3, for the case of a 6.33 kg impactor impacting the plate at 4.29 m/s, were repeated using LS-DYNA's TIEBREAK contact algorithm (*CONTACT AUTOMATIC ONE WAY SURFACE TO SURFACE TIEBREAK), where the contact interface was defined along all potential delamination crack paths (similar to the conventional CZM).

The cohesive parameters defined in the cohesive contact algorithm were similar to the values listed in Table 5.6. Several models were tested, with increasing number of through-thickness cohesive interfaces. All other model parameters, as well as boundary conditions, remained similar to the parameters described in Section 5.3.

Figure 6.10.a shows the impact force vs. displacement when the tiebreak cohesive interface is used to model the cohesive interface, and Figure 6.10.b shows the results obtained using the LCZ method. When a tiebreak contact is globally applied to all potential delamination crack propagation cracks, the structural stiffness of the plate decreases with increasing number of through-thickness cohesive interfaces. This effect is not noticeable when the LCZ method is used, and the cohesive interfaces are locally seeded within the model.

It can be concluded, that lower stiffness reduction was obtained when applying the LCZ method for the solution of the cases investigated, compared to the stiffness reduction caused by the application of the conventional CZM to the same problem. The lower effect of the LCZ method on the structural stiffness is in-line with the motivation for the development of the method, and it expected that this advantage will be more pronounced when the algorithm will be an integrated part of a finite-element solver, allowing the method to be applied to more complex structures.
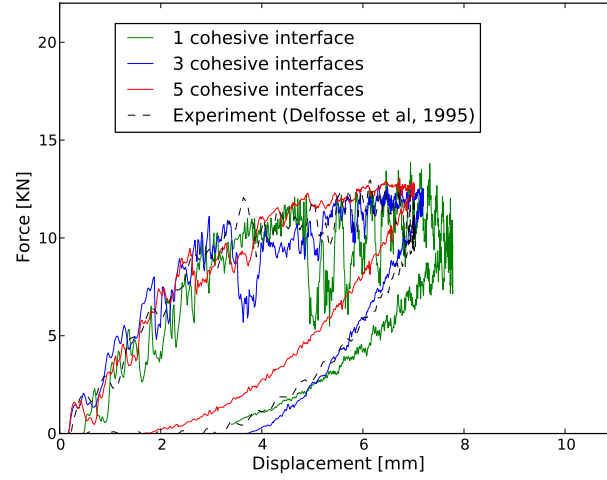
(a)
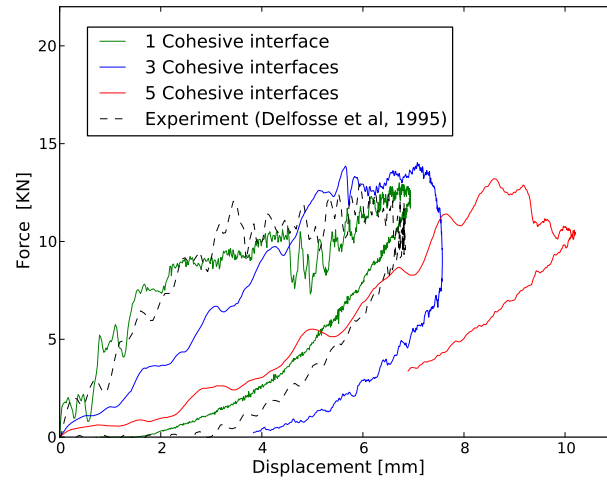
(b)

Figure 6.10: Predicted and experimental impact force vs. plate displacement, for a 6.33 kg impactor, impacting the plate at 4.29 m/s. **a.**) Results obtained using the LCZ method **b.**). Results obtained using the conventional CZ method. In both figures, results are shown for different number of through-thickness cohesive interfaces.

Chapter 7

Summary, Conclusions and Future Work

7.1 Summary

Computational modelling of delamination in laminated composite structures is challenging, due to the interaction of this damage mechanism with the other complex damage mechanisms in the material. Several numerical methods intended to simulate delamination in composites do exist, but they are still limited to the solution of relatively small-sized structures. Due to the relatively high numerical cost of the available methods, applying these methods to the solution of larger models is often not practical. Amongst the various numerical methods aimed at simulating delamination in composites, CZM is gaining increased popularity amongst scientists and engineers alike, due to its reliability and relatively simple numerical implementation in existing commercial finite element codes. Pioneering researchers around the world have suggested various approaches to allow using CZM in larger models, ranging from automatic scaling of the cohesive stiffness, in order to reduce the effect of the method on the stiffness of the structure, to adaptive approaches where cohesive interfaces are locally introduced into the finite element mesh, in order to reduce the computational cost. A novel approach, aimed at simulating delamination in composites using an adaptive manner, is presented here.

Chapter 2 presents a brief overview of the available numerical techniques, aimed at simulating delamination in composites, together with their benefits and limitations.

A novel technique aimed at simulating delamination in laminated composites in an adaptive manner, is presented in Chapter 3. The method allows modelling the structure without a priori knowledge or definition of the delamination location in the analysis, i.e. delaminations initiate and evolve as the simulation progresses. Using this method, no cohesive elements nor initial cracks need to be introduced in the finite element mesh

prior to the analysis. The continuum elements are split through their thickness and potential paths for delamination growth are seeded into the model adaptively.

In Chapter 4, the method is verified against the solution of pure delamination crack propagation, under mode-I, mode-II, and mixed-mode loading conditions. The method was shown capable of predicting the delamination crack in these cases with good to reasonable agreement with the analytical data, as well as with respect to results obtained using other numerical methods.

In Chapter 5, the method is validated against engineering applications, involving impact and dynamic loading scenarios. First, the method is applied for the static loading of a $[90/0]_s$ glass/epoxy double-notched tensile coupon (Chapter 5.1). The LCZ algorithm was able to predict the maximum load bearing capacity of the coupon, together with the deflection at complete rupture. Reasonable agreement was obtained when comparing the damage predicted in the coupon using the LCZ algorithm with the experimental results. In Section 5.2, the method is applied for a loading case involving dynamic tube crushing. Good agreement was obtained between the impact force profile predicted by the LCZ method, compared to an impact force profile obtained experimentally. When solving a dynamic plate-impact problem (Section 5.3), the LCZ method was successful in predicting the force vs. impactor's displacement profiles, as well as predicting the impactor's energy loss. The overall delamination patterns predicted using the LCZ method covered a larger area compared to the experimental observation, although the overall shape of the predicted delamination area agreed well with the experimental findings. Similar behavior was observed when the conventional CZM was applied to the problem, suggesting that the homogenization of the material and the lower number of cohesive interfaces in the finite element model had a negative effect on the predictive capability of this quantity.

In Chapter 6, the LCZ method was applied to larger numerical models. The LS-DYNA run-time when using the LCZ method, was shorter compared to the run-time when the conventional CZ method is applied to the problem. The efficiency of the LCZ method over conventional CZ method improves with increasing model size, which is an encouraging finding (A factor of 5.4 was measured in favour of the LCZ method, for the model size tested). In order to investigate the effect of the LCZ method on the structural stiffness of the structure, quasi-static bending loads were applied to a simple plate geometry, when the LCZ was applied to the problem. It was found that the results obtained using the LCZ method, were closer to the results obtained using a model containing no cohesive interface, compared to the results

147

obtained using the conventional CZM.

7.2 Conclusions

A new and robust computational method suited for efficient simulation of progression of delamination in laminated composite structures has been presented here. The following highlights the salient features and benefits of this newly developed local cohesive zone (LCZ) methodology:

- The method allows modelling the structure without a priori knowledge or definition of the delamination location in the analysis, i.e. delaminations initiate and evolve as the simulation progresses. Using this method, no cohesive elements nor initial cracks need to be introduced in the finite element mesh prior to the analysis. The continuum elements are split through their thickness and potential paths for delamination growth are seeded into the model adaptively.

- The method has only a minor effect on the overall structural stiffness before the onset of delamination, as the cohesive zone is locally embedded in the structure only where and when needed.

- The method uses a narrow band of cohesive elements that is sufficient to capture the mechanical behavior of the fracture process zone required for predicting delamination crack propagation.

- The method has the potential to be combined with other in-plane damage theories (e.g. continuum damage models developed at the UBC Composites Group ([89], [85], [37]), where intra-laminar damage is treated in a smeared manner, and the element stiffness is reduced gradually as a function of damage evolution within the finite element volume. Such methodology combines the numerical advantages of smeared modelling techniques with the need to model delamination in a discrete manner. The interaction of delamination damage with other damage mechanisms in composite materials is the subject of our ongoing research and further development of the algorithm.

In this paper, the LCZ method has been verified for Mode-I, Mode-II, and Mixed-Mode loading conditions. The obtained force-displacement results, as well as the overall energy balance, are shown to be in good agreement with the results predicted using other numerical and analytical methods available in the literature. Owing to the fact that the algorithm is currently

not an internal part of the finite element solver (LS-DYNA) used in this study, the various numerical operations performed by the algorithm on the finite element mesh lead to some numerical noise. The limited element formulations that are currently available in LS-DYNA pose some challenges in achieving full compatibility between the offset-shell elements (in the split region) and the thick-shell elements (in the unsplit region) of the mesh. In the current LCZ method this difficulty is overcome by introducing narrow regions of overlapping shell elements in the transition region. Nevertheless, the algorithm is able to capture the delamination crack propagation correctly. It is expected that further improvements in speed and accuracy of the computations will be attained once the algorithm is embedded within the finite element solver, and a layered thick-shell formulation with rotational nodal degrees of freedom is implemented in LS-DYNA. This would allow a smoother connectivity between the split and neighbouring unsplit regions of the mesh.

The initial results obtained from the application of the LCZ method to the various loading cases are encouraging, and prove that the local and adaptive insertion of cohesive zones into a finite element mesh can effectively capture the delamination crack propagation in laminated composite structures. Ongoing research is being carried out to verify the implementation and application of the method to more complex loading cases, involving a combination of in-plane damage together with delamination crack propagation, as well as simultaneous, multiple through-thickness delamination crack growth. Numerical issues such as the scalability of the current methodology and its computational efficiency relative to the conventional CZM is the subject of ongoing investigation.

7.3 Future Work

In order to allow the method to be applied to larger industrial applications and to improve its predictive capability, the following procedures should be taken:

- **Compatibility with higher DOF multilayered elements:** The current version of LS-DYNA does not support multilayered thick-shell elements with rotational degrees of freedom. This requires an artificial, non-physical solution to be enforced on the finite element model in the form of overlapping elements, in order to perform the element splitting operation. This overlapping, described in Section 3.3.5, is required in

order to transfer moment between the thick-shell elements and the offset shell elements created during the element splitting process.

- **Integrating the LCZ algorithm within LS-DYNA:** In its current form, the LCZ algorithm is an external Python code, written in Python, not embedded into LS-DYNA. Its execution is based on reading large volume of numerical results from the LS-DYNA simulations, a process which slows its execution and will be eliminated while the algorithm will be embedded into LS-DYNA.

- Introducing strain-rate dependencies to the cohesive model and the LCZ method in order to take account of the possible variation of the cohesive properties as a function of the interface loading rate.

Bibliography

[1] Benchmark assessment of automated delamination propagation capabilities in finite element codes for static loading. *Finite Elements in Analysis and Design*, 54:28 – 36, 2012.

[2] LS-DYNA Aerospace Working Group Modeling Guidelines Document. Technical report, 08 2014.

[3] E. Abisset, F. Daghia, X.C. Sun, M.R. Wisnom, and S.R. Hallett. Interaction of inter- and intralaminar damage in scaled quasi-static indentation tests: Part 1 - experiments. *Composite Structures*, 136: 712 – 726, 2016. ISSN 02638223.

[4] S. Abrate, J.F. Ferrero, and P. Navarro. Cohesive zone models and impact damage predictions for composite structures. *Meccanica*, 50 (10):2587 – 2620, 2015. ISSN 00256455.

[5] G. Alfano and M.A. Crisfield. Finite element interface models for the delamination analysis of laminated composites: Mechanical and computational issues. *International Journal for Numerical Methods in Engineering*, 50(7):1701 – 1736, 2001. ISSN 00295981.

[6] M. Anvari, I. Scheider, and C. Thaulow. Simulation of dynamic ductile crack growth using strain-rate and triaxiality-dependent cohesive elements. *Engineering Fracture Mechanics*, 73(15):2210 – 2228, 2006. ISSN 00137944.

[7] Luciana Arronche, Israel Martinez, Valeria La Saponara, and Elias Ledesma. Finite element modeling and experimental characterization of enhanced hybrid composite structures for improved crashworthiness. *Journal of Applied Mechanics, Transactions ASME*, 80(5), 2013. ISSN 00218936.

[8] G.I Barenblatt. The formation of equilibrium cracks during brittle fracture. general ideas and hypotheses. axially-symmetric cracks. *Journal of Applied Mathematics and Mechanics*.

[9] G.I. Barenblatt. The mathematical theory of equilibrium cracks in brittle fracture. *Advances in Applied Mechanics*, 7(C):55 – 129, 1962. ISSN 00652156. URL http://dx.doi.org/10.1016/S0065-2156(08)70121-2.

[10] Z. P. Bazant and J Planas. *Fracture and Size Effect in Concrete and Other Quasibrittle Materials*. CRC, 1st edition, 1998.

[11] Vladimir V. Bolotin. Delaminations in composite structures: its origin, buckling, growth and stability. *Composites Part B: Engineering*, 27(2):129 – 145, 1996. ISSN 13598368.

[12] Rikard Borg, Larsgunnar Nilsson, and Kjell Simonsson. Modeling of delamination using a discretized cohesive zone and damage formulation. *Composites Science and Technology*, 62(10-11):1299 – 1314, 2002. ISSN 02663538.

[13] Rikard Borg, Larsgunnar Nilsson, and Kjell Simonsson. Simulation of low velocity impact on fiber laminates using a cohesive zone based delamination model. *Composites Science and Technology*, 64(2):279 – 288, 2004. ISSN 02663538.

[14] G.T. Camacho and M. Ortiz. Computational modelling of impact damage in brittle materials. *International Journal of Solids and Structures*, 33(20-22):2899 – 2938, 1996. ISSN 00207683.

[15] Pedro P. Camanho. Mixed-mode decohesion finite elements for the simulation of delamination in composite materials. Technical report, University of Porto, Porto, Portugal, 06 2002.

[16] N.V. De Carvalho, B.Y. Chen, S.T. Pinho, J.G. Ratcliffe, P.M. Baiz, and T.E. Tay. Modeling delamination migration in cross-ply tape laminates. *Composites Part A: Applied Science and Manufacturing*, 71(0):192 – 203, 2015.

[17] C.C. Chang, R.S. Sandhu, R.L. Sierakowski, and W.E. Wolfe. Continuous stress finite element analysis of a free-edge delamination specimen. *Computers and Structures*, 29(5):783 – 793, 1988. ISSN 00457949.

[18] Livermore Software Technology Corporation. *LS-DYNA Keyword user's manual, 2013*.

[19] I.M. Daniel, R.E. Rowlands, and J.B. Whiteside. Effects of material and stacking sequence on behavior of composite plates with holes. *Experimental Mechanics*, 14(1):1 − 9, 1974. ISSN 00144851.

[20] Isaac M. Daniel and Ori Ishai. *Engineering Mechanics of Composite Materials*. Oxford University Press, Inc., second edition, 2006.

[21] G.A.O. Davies and X. Zhang. Impact damage prediction in carbon composite structures. *International Journal of Impact Engineering*, 16(1):149 − 170, 1995. ISSN 0734743X.

[22] Rene de Borst, Miguel A. Gutierrez, Garth N. Wells, Joris J.C. Remmers, and Harm Askes. Cohesive-zone models, higher-order continuum theories and reliability methods for computational failure analysis. *International Journal for Numerical Methods in Engineering*, 60(1):289 − 315, 2004. ISSN 00295981.

[23] A.B. De Morais. Simplified cohesive zone analysis of mixed-mode i-ii delamination in composite beams. *Polymer Composites*, 34(11):1901 − 1911, 2013. ISSN 02728397.

[24] Daniel Delfosse, Anoush Poursartip, Brian R. Coxon, and Ernest F. Dost. Non-penetrating impact behavior of cfrp at low and intermediate velocities. Number 1230, pages 333 − 350, Atlanta, GA, USA, 1995.

[25] S. J. DeTeresa, L. M. Allison, B. J. Cunningham, D. C. Freeman, M. D. Saculla, R. J. Sanchez, and S. W. Winchester. Experimental Results in Support of Simulating Progressive Crush in Carbon-Fiber Textile Composites. Technical Report UCRL-ID-143287, Lawrence Livermore National Laboratory, 04 2001.

[26] Paul Du Bois, Feucht Markus, Haufe Andre, and Kolling Steffan. A generalized damage and failure formulation for SAMP. *5th German LS-DYNA forum*, 2006.

[27] Dugdale. Yielding of steel sheets containing slits. *Journal of the Mechanics and Physics of Solids*, 8(2), 1960.

[28] M. Elices, G.V. Guinea, J. Gomez, and J. Planas. The cohesive zone model: Advantages, limitations and challenges. *Engineering Fracture Mechanics*, 69(2):137 − 163, 2002. ISSN 00137944.

[29] A.M. Elmarakbi, N. Hu, and H. Fukunaga. Finite element simulation of delamination growth in composite materials using ls-dyna. *Composites Science and Technology*, 69(14):2383 – 2391, 2009. ISSN 02663538.

[30] M.L. Falk, A. Needleman, and J.R. Rice. A critical evaluation of cohesive zone models of dynamic fracture. volume 11, pages Pr543 – Pr550, Delft, Netherlands, 2001.

[31] Gary L. Farley. Effect of specimen geometry on the energy absorption capability of composite materials. *Journal of Composite Materials*, 20 (4):390 – 400, 1986. ISSN 00219983.

[32] Jones Robert M. Farley, Gary L. Crushing characteristics of continuous fiber-reinforced composite tubes. *Journal of Composite Materials*, 26(1):37 – 50, 1992. ISSN 00219983.

[33] D. Feng and F. Aymerich. Finite element modelling of damage induced by low-velocity impact on composite laminates. *Composite Structures*, 108(1):161 – 171, 2013. ISSN 02638223.

[34] Hermes F.H. Process zone and cohesive element size in delamination in bi-layers. *Eindhoven University of Technology*, 9 2010.

[35] Alireza Forghani. *A Non-Local Approach to Simulation of Damage in Composite Structures*. PhD thesis, The University of British Columbia, 2011.

[36] Alireza Forghani and Reza Vaziri. Computational modeling of damage development in composite laminates subjected to transverse dynamic loading. *Journal of Applied Mechanics, Transactions ASME*, 76(5):1 – 11, 2009. ISSN 00218936.

[37] Alireza Forghani, Navid Zobeiry, Anoush Poursartip, and Reza Vaziri. A structural modelling framework for prediction of damage development and failure of composite laminates. *Journal of Composite Materials*, 47(20-21):2553 – 2573, 2013. ISSN 00219983.

[38] Gordon Geicler and Michael Kaliske. Time-dependent cohesive zone modelling for discrete fracture simulation. *Engineering Fracture Mechanics*, 77(1):153 – 169, 2010. ISSN 00137944.

[39] B. Gershon and G. Marom. Fracture toughness and mechanical properties of glass fibre - epoxy composites. *Journal of Materials Science*, 10(9):1549 – 1556, 1975. ISSN 00222461.

[40] Philippe H. Geubelle and Jeffrey S. Baylor. Impact-induced delamination of composites: A 2d simulation. *Composites Part B: Engineering*, 29(5):589 – 602, 1998. ISSN 13598368.

[41] H. Ghasemnejad, H. Hadavinia, and A. Aboutorabi. Effect of delamination failure in crashworthiness analysis of hybrid composite box structures. *Materials and Design*, 31(3):1105 – 1116, 2010. ISSN 02613069.

[42] E.V. Gonzalez, P. Maimi, P.P. Camanho, A. Turon, and J.A. Mayugo. Simulation of drop-weight impact and compression after impact tests on composite laminates. *Composite Structures*, 94(11):3364 – 3378, 2012. ISSN 02638223.

[43] Burak Gozluklu, Imren Uyar, and Demirkan Coker. Intersonic delamination in curved thick composite laminates under quasi-static loading. *Mechanics of Materials*, 80(PB):163 – 182, 2015. ISSN 01676636.

[44] B.G. Green, M.R. Wisnom, and S.R. Hallett. An experimental investigation into the tensile strength scaling of notched composites. *Composites Part A: Applied Science and Manufacturing*, 38(3):867 – 878, 2007. ISSN 1359835X.

[45] S.R. Hallett, B.G. Green, W.G. Jiang, and M.R. Wisnom. An experimental and numerical investigation into the damage mechanisms in notched composites. *Composites Part A: Applied Science and Manufacturing*, 40(5):613 – 624, 2009. ISSN 1359835X.

[46] Stephen R. Hallett and Michael R. Wisnom. Numerical investigation of progressive damage and the effect of layup in notched tensile tests. *Journal of Composite Materials*, 40(14):1229 – 1245, 2006. ISSN 00219983.

[47] Stephen R. Hallett and Michael R. Wisnom. Experimental investigation of progressive damage and the effect of layup in notched tensile tests. *Journal of Composite Materials*, 40(2):119 – 141, 2006. ISSN 00219983.

[48] Stephen R. Hallett and Michael R. Wisnom. Experimental investigation of progressive damage and the effect of layup in notched tensile tests. *Journal of Composite Materials*, 40(2):119 – 141, 2006. ISSN 00219983.

[49] Stephen R. Hallett and Michael R. Wisnom. Experimental investigation of progressive damage and the effect of layup in notched tensile tests. *Journal of Composite Materials*, 40(2):119 – 141, 2006. ISSN 00219983.

[50] Haipeng Han, Farid Taheri, Neil Pegg, and You Lu. A numerical study on the axial crushing response of hybrid pultruded and 45 braided tubes. *Composite Structures*, 80(2):253 – 264, 2007. ISSN 02638223.

[51] Haipeng Han, Farid Taheri, and Neil Pegg. Crushing behaviors and energy absorption efficiency of hybrid pultruded and 45 braided tubes. *Mechanics of Advanced Materials and Structures*, 18(4):287 – 300, 2011. ISSN 15376494.

[52] Paul W. Harper, Lu Sun, and Stephen R. Hallett. A study on the influence of cohesive zone interface element strength parameters on mixed mode behavior. *Composites Part A: Applied Science and Manufacturing*, 43(4):722 – 734, 2012. ISSN 1359835X.

[53] S. Heimbs, T. Bergmann, D. Schueler, and N. Toso-PentecOte. High velocity impact on preloaded composite plates. *Composite Structures*, 111(1):158 – 168, 2014. ISSN 02638223.

[54] A. Hillerborg, M. ModÃĺer, and P.-E. Petersson. Analysis of crack formation and crack growth in concrete by means of fracture mechanics and finite elements. *Cement and Concrete Research*, 6(6):773 – 781, 1976. ISSN 0008-8846.

[55] J.P. Hou, N. Petrinic, and C. Ruiz. A delamination criterion for laminated composites under low-velocity impact. *Composites Science and Technology*, 61(14):2069 – 2074, 2001. ISSN 02663538.

[56] N. Hu, Y. Zemba, H. Fukunaga, H.H. Wang, and A.M. Elmarakbi. Stable numerical simulations of propagations of complex damages in composite structures under transverse loads. *Composites Science and Technology*, 67(3-4):752 – 765, 2007. ISSN 02663538.

[57] Jagota A. Bennison S.J. Londono J.D. Hui, C.Y. Crack blunting and the strength of soft elastic solids. volume 459, pages 1489–1516, Ottawa, ON, Canada, 2003.

[58] D. Hull. Unified approach to progressive crushing of fibre-reinforced composite tubes. *Composites Science and Technology*, 40(4):377 – 421, 1991. ISSN 02663538.

[59] G.R Irwin. Plastic zone near a crack and fracture toughness. In *Proceedings of the Seventh Sagamore Ordnance Materials Conference*, pages 63–78. New York: Syracuse University, 1960.

[60] Yang Jiao and Jacob Fish. On the equivalence between the s-method, the xfem and the ply-by-ply discretization for delamination analyses of laminated composites. *International Journal of Fracture*, 2015. ISSN 03769429.

[61] Paul A. Lagace John C. Brewer. Quadratic stress criterion for initiation of delamination. *Journal of Composite Materials*, 22(12):1141 – 1155, 1988.

[62] M. Kaliske, G. Geiler, and C. Morgner. Discrete crack path prediction by an adaptive cohesive crack model. volume 4, pages 2769 – 2778, Ottawa, ON, Canada, 2009.

[63] M. Kashtalyan and C. Soutis. Stiffness degradation in cross-ply laminates damaged by transverse cracking and splitting. *Composites Part A: Applied Science and Manufacturing*, 31(4):335 – 351, 2000. ISSN 1359835X.

[64] Luiz F. Kawashita, Alexandre Bedos, and Stephen R. Hallett. Modelling mesh independent transverse cracks in laminated composites with a simplified cohesive segment method. *Computers, Materials and Continua*, 32(2):133 – 158, 2012. ISSN 15462218.

[65] Ingrid Kongshavn and Anoush Poursartip. Experimental investigation of a strain-softening approach to predicting failure in notched fibre-reinforced composite laminates. *Composites Science and Technology*, 59(1):29 – 40, 1999. ISSN 02663538.

[66] M.T. Kortschot and P.W.R. Beaumont. Damage mechanics of composite materials ii. a damaged-based notched strength model. *Cambridge University, Engineering Department (Technical Report) CUED/C-MATS*, (165), 1989. ISSN 03196505.

[67] M.T. Kortschot and P.W.R. Beaumont. Damage mechanics of composite materials. i. measurements of damage and strength. *Composites Science and Technology*, 39(4):289 – 301, 1990. ISSN 02663538.

[68] R. Krueger. Development of a benchmark example for delamination fatigue growth prediction. volume 2, pages 948 – 967, Dayton, OH, United states, 2010. Analysis softwares;Commercial codes;Commercial finite element codes;Cyclic loadings;Delamination growth;Double cantilever beam;Finite element models;Growth analysis;Growth increments;Input parameter;Mixed mode;Number of cycles;Prediction capability;.

[69] Ronald Krueger. Virtual crack closure technique: History, approach, and applications. *Applied Mechanics Reviews*, 57(1-6):109 – 143, 2004. ISSN 00036900.

[70] Andrzej Leski. Implementation of the virtual crack closure technique in engineering fe calculations. *Finite Elements in Analysis and Design*, 43(3):261 – 268, 2007. ISSN 0168874X.

[71] Larry B. Lessard, Andrew S. Schmidt, and Mahmood M. Shokrieh. Three-dimensional stress analysis of free-edge effects in a simple composite cross-ply laminate. *International Journal of Solids and Structures*, 33(15):2243 – 2259, 1996. ISSN 00207683.

[72] C.F. Li, N. Hu, J.G. Cheng, H. Fukunaga, and H. Sekine. Low-velocity impact-induced damage of continuous fiber-reinforced composite laminates. part ii. verification and numerical investigation. *Composites Part A: Applied Science and Manufacturing*, 33(8):1063 – 1072, 2002. ISSN 1359835X.

[73] C.F. Li, N. Hu, Y.J. Yin, H. Sekine, and H. Fukunaga. Low-velocity impact-induced damage of continuous fiber-reinforced composite laminates. part i. an fem numerical model. *Composites Part A: Applied Science and Manufacturing*, 33(8):1055 – 1062, 2002. ISSN 1359835X.

[74] Xiangqian Li, Stephen R. Hallett, Michael R. Wisnom, Navid Zobeiry, Reza Vaziri, and Anoush Poursartip. Experimental study of damage propagation in over-height compact tension tests. *Composites Part A: Applied Science and Manufacturing*, 40(12):1891 – 1899, 2009. ISSN 1359835X.

[75] Xiangqian Li, Stephen R. Hallett, and Michael R. Wisnom. Numerical investigation of progressive damage and the effect of layup in overheight compact tension tests. *Composites Part A: Applied Science and Manufacturing*, 43(11):2137 – 2150, 2012. ISSN 1359835X.

[76] P.F. Liu, S.J. Hou, J.K. Chu, X.Y. Hu, C.L. Zhou, Y.L. Liu, J.Y. Zheng, A. Zhao, and L. Yan. Finite element analysis of postbuckling and delamination of composite laminates using virtual crack closure technique. *Composite Structures*, 93(6):1549 – 1560, 2011. ISSN 02638223.

[77] Xia Liu, Ravindra Duddu, and Haim Waisman. Discrete damage zone model for fracture initiation and propagation. *Engineering Fracture Mechanics*, 92:1 – 18, 2012. ISSN 00137944.

[78] Shuchang Long, Xiaohu Yao, and Xiaoqing Zhang. Delamination prediction in composite laminates under low-velocity impact. *Composite Structures*, 132:290 – 298, 2015. ISSN 02638223.

[79] L. Maio, E. Monaco, F. Ricci, and L. Lecce. Simulation of low velocity impact on composite laminates with progressive failure analysis. *Composite Structures*, 103:75 – 85, 2013. ISSN 02638223.

[80] Dhaval P. Makhecha, Rakesh K. Kapania, Eric R. Johnson, David A. Dillard, George C. Jacob, and J. Mike Starbuck. Rate-dependent cohesive zone modeling of unstable crack growth in an epoxy adhesive. *Mechanics of Advanced Materials and Structures*, 16(1):12 – 19, 2009. ISSN 15376494.

[81] A.G. Mamalis, D.E. Manolakos, M.B. Ioannidis, D.G. Chronopoulos, and P.K. Kostazos. On the crashworthiness of composite rectangular thin-walled tubes internally reinforced with aluminium or polymeric foams: Experimental and numerical simulation. *Composite Structures*, 89(3):416 – 423, 2009. ISSN 02638223.

[82] Michael May. Numerical evaluation of cohesive zone models for modeling impact induced delamination in composite materials. *Composite Structures*, 133:16 – 21, 2015. ISSN 02638223.

[83] Scott Andrew McClennan. Crack growth and damage modeling of fibre reinforced polymer composites, 10 2004.

[84] Carla McGregor, Reza Vaziri, and Anoush Poursartip. Final Report: Numerical Simulation of the Axial Crushing of Braided Composite Tubes. Technical report, The University of British Columbia, February 2008.

[85] Carla McGregor, Reza Vaziri, and Xinran Xiao. Finite element modelling of the progressive crushing of braided composite tubes under axial impact. *International Journal of Impact Engineering*, 37(6):662 – 672, 2010. ISSN 0734743X.

[86] Carla McGregor, Reza Vaziri, Anoush Poursartip, and Xinran Xiao. Crushing of triaxially braided composite tubes at quasi-static and dynamic rates. *Submitted to Composite Structures*, 2016.

[87] Carla McGregor, Reza Vaziri, Anoush Poursartip, and Xinran Xiao. Calibration and validation of a continuum damage mechanics model in aid of axial crush simulation of braided composite tubes. *Submitted to Composites Structures, part A: applied Science and Manufacturing*, 2016.

[88] Carla J McGregor. Simulation of progressive damage development in braided composite tubes under axial compression. *MASc thesis, The University of British Columbia*.

[89] Carla J. McGregor, Reza Vaziri, Anoush Poursartip, and Xinran Xiao. Simulation of progressive damage development in braided composite tubes under axial compression. *Composites Part A: Applied Science and Manufacturing*, 38(11):2247 – 2259, 2007. ISSN 1359835X.

[90] Costantino Menna, Domenico Asprone, Giancarlo Caprino, Valentina Lopresto, and Andrea Prota. Numerical simulation of impact tests on gfrp composite laminates. *International Journal of Impact Engineering*, 38(8-9):677 – 685, 2011. ISSN 0734743X.

[91] Y. Mi, M.A. Crisfield, G.A.O. Davies, and H.-B. Hellweg. Progressive delamination using interface elements. *Journal of Composite Materials*, 32(14):1246 – 1272, 1998. ISSN 00219983.

[92] Nicolas Moes and Ted Belytschko. Extended finite element method for cohesive crack growth. *Engineering Fracture Mechanics*, 69(7):813 – 833, 2002.

[93] Marco Musto and Giulio Alfano. A fractional rate-dependent cohesive-zone model. *International Journal for Numerical Methods in Engineering*, 103(5):313 – 341, 2015. ISSN 00295981.

[94] A. Needleman. Numerical modeling of fast crack growth. volume 74, pages 37 –, Atlanta, GA, USA, 1996.

[95] A. Needleman. Some issues in cohesive surface modeling. volume 10, pages 221 – 246, Beijing, China, 2013. URL http://dx.doi.org/10.1016/j.piutam.2014.01.020. Cohesive surface;Cohesive tractions;Complex microstructures;Constitutive law;Constitutive relations;Displacement jump;Predictive capabilities;Stress and strain;.

[96] O.J. Nixon-Pearson, S.R. Hallett, P.W. Harper, and L.F. Kawashita. Damage development in open-hole composite specimens in fatigue. part 2: Numerical modelling. *Composite Structures*, 106:890 – 898, 2013. ISSN 02638223.

[97] Robin Olsson, Rickard Juntikka, and Leif E. Asp. High velocity hail impact on composite laminates - modelling and testing. *Solid Mechanics and its Applications*, 192:393 – 426, 2013. ISSN 09250042.

[98] Adrian C. Orifici and Ronald Krueger. Assessment of static delamination propagation capabilities in commercial finite element codes using benchmark analysis. *NASA Technical report*, NIA Report(2010-03):1 – 42, 2010.

[99] N.J. Pagano and R.Byron Pipes. Some observations on the interlaminar strength of composite laminates. *International Journal of Mechanical Sciences*, 15(8):679 – 692, 1973. ISSN 00207403.

[100] Sivakumar Palanivelu and Ajit Kumar Jindal. Numerical energy absorption assessment of composite materials. volume 8, Rosemont, IL, United states, 2012.

[101] A. Pandolfi and M. Ortiz. An efficient adaptive procedure for three-dimensional fragmentation simulations. *Engineering with Computers*, 18(2):148 – 159, 2002. ISSN 01770667.

[102] Katerina D. Papoulia, Chin-Hang Sam, and Stephen A. Vavasis. Time continuity in cohesive finite element modeling. *International Journal for Numerical Methods in Engineering*, 58(5):679 – 701, 2003. ISSN 00295981.

[103] Chung-Kyu Park, Cing-Dao Kan, Steven Reagan, and Balachandra R. Deshpande. Crashworthiness of composite inserts in vehicle structure. *International Journal of Crashworthiness*, 17(6):665 – 675, 2012. ISSN 13588265.

[104] Chung-Kyu Park, Cing-Dao Steve Kan, and William Thomas Hollowell. Evaluation of crashworthiness of a carbon-fibre-reinforced polymer (cfrp) ladder frame in a body-on-frame vehicle. *International Journal of Crashworthiness*, 2013. ISSN 13588265.

[105] Kyoungsoo Park, Glaucio H. Paulino, Waldemar Celes, and Rodrigo Espinha. Adaptive mesh refinement and coarsening for cohesive zone modeling of dynamic fracture. *International Journal for Numerical Methods in Engineering*, 92(1):1 – 35, 2012. ISSN 00295981.

[106] A. Poursartip, A. Gambone, S. Ferguson, and G. Fernlund. In-situ sem measurements of crack tip displacements in composite laminates to determine local g in mode i and ii. *Engineering Fracture Mechanics*, 60(2):173 – 185, 1998. ISSN 00137944.

[107] Michael R. Wisnom and Fu-Kuo Chang. Modelling of splitting and delamination in notched cross-ply laminates. *Composites Science and Technology*, 60(15):2849 – 2856, 2000. ISSN 02663538.

[108] I.S. Raju, J.H.Jr Crews, and M.A. Aminpour. Convergence of strain energy release rate components for edge-delaminated composite laminates. *Engineering Fracture Mechanics*, 30(3):383 – 396, 1988. ISSN 00137944.

[109] J. R. Rice. The mechanics of earthquake rupture. volume 78, pages 555 – 649, 1980. ISBN 0-444-85461-4.

[110] J. Rots. *Computational modeling of concrete fracture*. PhD thesis, Delft University of Technology, 1998.

[111] Gonzalo Ruiz, Anna Pandolfi, and Michael Ortiz. Three-dimensional cohesive modeling of dynamic mixed-mode fracture. *International Journal for Numerical Methods in Engineering*, 52(1-2):97 – 120, 2001. ISSN 00295981.

[112] E.F. Rybicki and M.F. Kanninen. Finite element calculation of stress intensity factors by a modified crack closure integral. *Engineering Fracture Mechanics*, 9(4):931 – 938, 1977. ISSN 00137944.

[113] E.F. Rybicki, D.W. Schmueser, and J. Fox. Energy release rate approach for stable crack growth in the free-edge delamination problem. *Journal of Composite Materials*, 11:470 − 487, 1977. ISSN 00219983.

[114] Chin-Hang Sam, Katerina D. Papoulia, and Stephen A. Vavasis. Obtaining initially rigid cohesive finite element models that are temporally convergent. *Engineering Fracture Mechanics*, 72(14):2247 − 2267, 2005. ISSN 00137944.

[115] J.C.J. Schellekens and R. De Borst. Numerical simulation of free edge delamination in graphite-epoxy laminates under uniaxial tension. pages 647 − 647, Paisly, Scotl, 1991.

[116] J.H.A. Schipperen and F.J. Lingen. Validation of two-dimensional calculations of free edge delamination in laminated composites. *Composite Structures*, 45(3):233 − 240, 1999. ISSN 02638223.

[117] Y.B. Shi, D. Hull, and J.N. Price. Mode ii fracture of +/- angled laminate interfaces. *Composites Science and Technology*, 47(2):173 − 184, 1993. ISSN 02663538.

[118] O. Shor and R. Vaziri. Adaptive insertion of cohesive elements for simulation of delamination in laminated composite materials. *Engineering Fracture Mechanics*, 35(1), 2015.

[119] Harpreet Singh, Kiran Kumar Namala, and Puneet Mahajan. A damage evolution study of e-glass/epoxy composite under low velocity impact. *Composites Part B: Engineering*, 76:235 − 248, 2015. ISSN 13598368.

[120] Vladimir S. Sokolinsky, Kyle C. Indermuehle, and Juan A. Hurtado. Numerical simulation of the crushing process of a corrugated composite plate. *Composites Part A: Applied Science and Manufacturing*, 42 (9):1119 − 1126, 2011. ISSN 1359835X.

[121] M.C. Song, B.V. Sankar, G. Subhash, and C.F. Yen. Finite element analysis of delamination in woven composites under quasi-static indentation. *Computers, Materials and Continua*, 35(1):67 − 85, 2013. ISSN 15462218.

[122] X.C. Sun, M.R. Wisnom, and S.R. Hallett. Interaction of inter- and intralaminar damage in scaled quasi-static indentation tests: Part 2 - numerical simulation. *Composite Structures*, 136:727 − 742, 2016. ISSN 02638223.

[123] I. Tawk, P. Navarro, J.-F. Ferrero, J.-J. Barrau, and E. Abdullah. Composite delamination modelling using a multi-layered solid element. *Composites Science and Technology*, 70(2):207 – 214, 2010. ISSN 02663538.

[124] Andrew A. O. Tay and K.Y. Goh. A study of delamination growth in the die-attach layer of plastic ic packages under hygrothermal loading during solder reflow. *IEEE Transactions on Device and Materials Reliability*, 3(4):144 – 151, 2003. ISSN 15304388.

[125] P.H. Thornton and P.J. Edwards. Energy absorption in composite tubes. *Journal of Composite Materials*, 16(6):521 – 545, 1982. ISSN 00219983.

[126] Albert Turon, Carlos G. DaÌ£vila, Pedro P. Camanho, and Josep Costa. An Engineering Solution for using Coarse Meshes in the Simulation of Delamination With Cohesive Zone Models. Technical Report NASA/TM-2005-213547, NASA, 03 2005.

[127] R.C. Vankuren and J.E. Scott. Energy absorption of high-strength steel tubes under impact crush conditions. 400 Commonwealth Drive, Warrendale, PA 15096-0001, United States, 1977.

[128] H.M. Westergaard. Bearing pressures and cracks. *American Society of Mechanical Engineers – Transactions – Journal of Applied Mechanics*, 6(2):–49—53 –, 1939.

[129] Kevin V. Williams, Reza Vaziri, and Anoush Poursartip. A physically based continuum damage mechanics model for thin laminated composite structures. *International Journal of Solids and Structures*, 40 (9):2267 – 2300, 2003. ISSN 00207683.

[130] De Xie and Anthony M. Waas. Discrete cohesive zone model for mixed-mode fracture using finite element analysis. *Engineering Fracture Mechanics*, 73(13):1783 – 1796, 2006. ISSN 00137944.

[131] Xiaodong Xu, Michael R. Wisnom, Yusuf Mahadik, and Stephen R. Hallett. An experimental investigation into size effects in quasi-isotropic carbon/epoxy laminates with sharp and blunt notches. *Composites Science and Technology*, 100:220 – 227, 2014. ISSN 02663538.

[132] Xiaodong Xu, Michael R. Wisnom, Yusuf Mahadik, and Stephen R. Hallett. Scaling of fracture response in over-height compact tension

tests. *Composites Part A: Applied Science and Manufacturing*, 69:40
– 48, 2014. ISSN 1359835X.

[133] Xiaodong Xu, Michael R. Wisnom, Xiangqian Li, and Stephen R. Hallett. A numerical investigation into size effects in centre-notched quasi-isotropic carbon/epoxy laminates. *Composites Science and Technology*, 111:32 – 39, 2015. ISSN 02663538.

[134] Qingda Yang and Brian Cox. Cohesive models for damage evolution in laminated composites. *International Journal of Fracture*, 133(2): 107 – 137, 2005. ISSN 03769429.

[135] Yan Zhang, Ping Zhu, and Xinmin Lai. Finite element analysis of low-velocity impact damage in composite laminated plates. *Materials and Design*, 27(6):513 – 519, 2006. ISSN 02641275.

[136] S. Zheng and C.T. Sun. Double-plate finite-element model for the impact-induced delamination problem. *Composites Science and Technology*, 53(1):111 – 118, 1995. ISSN 02663538.

[137] N. Zobeiry, R. Vaziri, and A. Poursartip. Characterization of strain-softening behavior and failure mechanisms of composites under tension and compression. *Composites Part A: Applied Science and Manufacturing*, 68(0):29 – 41, 2015. ISSN 1359-835X.

[138] Navid Zobeiry. *Extracting the strain-softening response of composites using full-field displacement measurement*. PhD thesis, The University of British Columbia, 2010.

Appendix A

Flowchart of the LCZ Algorithm

This Appendix presents a schematic flow-chart description of the LCZ algorithm, which is shown in Figure A.1, Figure A.2, Figure A.3 and Figure A.4.

Schematic flowchart of the LCZ algorithm

- Read LCZ algorithm-related parameters and control variables.
- Read finite-element input file, search for composite part definitions and material orientations.
- Read user-defined element splitting criterion

Step A

Initialize/ continue the finite-element transient analysis. Normal termination occurs if termination time is reached or element-splitting criterion is met (next step)

- Create an empty set of elements *A* which will include all of the element numbers flagged for splitting.
- Search for the first element in the mesh that satisfies the user-defined element splitting criterion.
- Add this element number to set *A* (Figure 1).

Figure 1: First element to satisfy the element splitting criterion

Figure 2: Identify elements close to satisfying the element splitting criterion by a user-defined threshold

- Search for more elements that were close to satisfying the user-defined element splitting criterion identified by a user-defined threshold (Figure 2)
- Add these element numbers to set *A*

Proceed to step B

Figure A.1: Schematic LCZ algorithm flowchart, image 1 out of 7

Step B

- Geometrical searches – for each element, i, in set A, find all elements that belong to the same source ply as element i, and have their centroids lie within a user-defined radius R from the centroid of element i.
- Add these element numbers to set A (Figures 3a, 3b and 3c)

Proceed to step C

Figure 3a: Perform ply-based geometrical search

Figure 3b: Identify elements that satisfy the geometrical search

Ply I
Ply II
Ply III

Elements which have their centroid lie within a distance R from the centroid of element i, but DO NOT share the same ply as element i.

An element whose centroid lies within a distance R from the centroid of element i and shares the same ply as element i.

R

Element I which belongs to set A

Figure 3c – A schematic cross section in a composite laminate consisting of 3 plies - only elements which satisfy the radial search and share the same ply as element i are included in set A.

Figure A.2: Schematic LCZ algorithm flowchart, image 2 out of 7

Step C

- Splitting operation – for each element i in set A, create two elements through the thickness of the parent element i, using the nodes originally used for the definition of element i.
- The thickness of each newly created element is obtained based on the through-thickness splitting location.

yes

Figure 4b: Cohesive elements/interfaces **are created** on the marked elements which belong to element set A, as they do not neighbor with composite elements **not belonging** to set A

Do the elements in set A have rotational DOF as well as translational DOF?

no

yes

Proceed to step D

Cohesive element/interface creation
- For each element i in set A, insert cohesive elements/interfaces connecting each pair of elements that were created during the splitting operation, **unless** the element lies on the edge of the split region, **and** is neighboring with other element(s) which are not to be split (are not in set A) (Figure 4a and Figure 4b)

Figure 4a: Cohesive elements/interfaces are **NOT** created on the marked elements belonging to set A, as they neighbor composite elements **not belonging** to set A

Proceed to step E

Figure A.3: Schematic LCZ algorithm flowchart, image 3 out of 7

step D

Cohesive element/interface creation
- For each element *i* in set A, insert cohesive elements/interfaces connecting each pair of elements that were created during the splitting operation.

Cohesive element/interface creation - continued

- The properties for each cohesive element/interface being created is derived from a list of user defined interface properties, which are defined at the beginning of the run. Multiple properties could be specified for multiple delamination crack propagation, such that the appropriate cohesive properties are assigned to specific delamination cracks.

step E

Proceed to step F

Figure A.4: Schematic LCZ algorithm flowchart, image 4 out of 7

Step F

Mapping
- For each parent element *i* in set *A*, map the stresses/strains and state variables onto the newly created elements.

- Mapping is performed by keeping consistency with the integration point orientation, such that the information from each integration point belonging to the parent element is mapped to the appropriate integration point in the newly created element.

Figure 5: A schematic cross sectional view demonstrating the mapping process. Mapping is performed from each integration point in the parent element to the appropriate integration point in the newly created elements. The virtual splitting location is marked with a dashed line.

Do the elements in set *A* have rotational DOF as well as translational DOF?

yes

no

Remove all elements in set *A* from the finite element mesh

Proceed to step G

Proceed to step J

Figure A.5: Schematic LCZ algorithm flowchart, image 5 out of 7

Step G

Figure 6a: Elements belonging to set *A* which lie on the edge of the region defined by set *A*, **BUT have all their** neighboring elements belonging to set *A.*

Figure 6b: Elements belonging to set *A* which lie on the edge of the region defined by set *A*, **AND have at least one** neighbor that does not belong to set *A*. These elements labeled with green circles are added to set *B.*

For each element *i* in set *A,* check if it lies on the edge of the region defined by set *A,* **AND** is also neighboring with elements not belonging to set *A* (Figure 6a and Figure 6b)

no

yes

- Continue performing this check for all elements in set *A.*

- Add these elements to element set *B*
- Continue performing this check for all elements in set *A*

Proceed to step H

Figure A.6: Schematic LCZ algorithm flowchart, image 6 out of 7

Figure 7: Remove all elements in set A which DO NOT belong to set B (marked here with blue circles) from the FE mesh

Figure A.7: Schematic LCZ algorithm flowchart, image 7 out of 7

Appendix B

Execution of the LCZ Algorithm

This appendix describes the procedure required in order to correctly set-up and perform a mechanical analysis using the LCZ algorithm. Currently, in its BETA version, the algorithm can be executed using a Linux operating system having a Python installation.

In order to execute the code, the following steps should be performed:

1. **Setting the working directories**: A working directory is to be created, in which the execution will take place. Within this directory, two subdirectories should be created: `build` directory, containing all of the binary files of the algorithm. The user must not alter the content of this directory as it contains all of the binary files required for the correct execution of the code. A second directory, titled `dist`, serves as the directory which the actual algorithm execution will be performed. The `dist` directory should include the following files: the LCZ algorithm executable, the `parameters.txt` text file described bellow, containing all of the required user-defined parameters controlling the execution of the LCZ algorithm, and the LS-DYNA keyword file/s of the mechanical problem to be solved during the analysis.

2. **The `parameters.txt` file:** This file which is placed right beside the LCZ executable, allows the user to control various aspects of the run. A typical file is brought in Program B.1. The file format should not change from the format brought here. The following is a description of the different fields within the file.

   - `runfile` : Name of LS-DYNA's keyword file describing the mechanical problem under investigation, which will be solved using the LCZ algorithm, in this example, FILENAME.

   - `instant_split` : A flag to perform an automatic split and insertion of cohesive elements through all of the interfaces defined in the
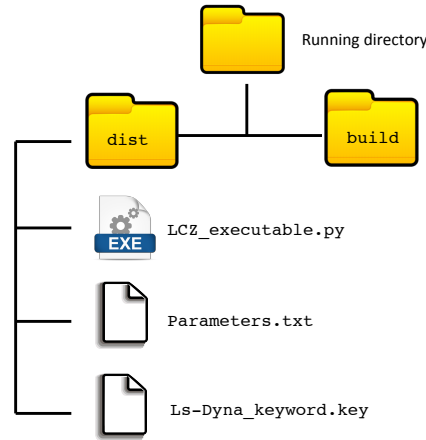
Figure B.1: Schematic directory architecture required for the correct execution of the LCZ algorithm.

model, without performing an initial LS-DYNA run. Options for this parameter are either "`true`" or "`false`", in this example, it is set to `false`. Setting this parameter to "`true`", will cause the LCZ algorithm to perform a single LS-DYNA run, in which all thick-shell elements will be split and converted into offset-shell elements with solid-cohesive elements embedded in between these offset-shells. Such a model is equivalent to solving the problem using the conventional CZ method. Thus, this parameter allows a useful mean of comparing the results obtained using the LCZ method to the conventional CZ method's results. Setting this parameter to "`false`" will perform a standard LCZ simulation in which solid cohesive elements will be adaptively seeded into the structure.

- `interface_springback_NSHV` : Number of history variables to be mapped during the mapping process, for each integration point, during the element splitting operation. In this example, this number is set equal to 5. This value is material-model dependent, as each of LS-DYNA's material model has a different number of his-

tory variables. More information can be found in LS-DYNA's keyword manual [18].

- `radial_split_distance` : Distance in length units used by the radials-search algorithm during the element splitting process. In this example, this number is set equal to 8.

- `exe` : Path to LS-DYNA's executable which will be used for the solution of the mechanical analysis. In this example, this path is defined as `/home/username/./lsdyna_exe`.

- `termination_factor` : Currently, the LCZ algorithm is not embedded into LS-DYNA, and is based on reading LS-DYNA's ELOUT ASCII files for obtaining the thick-shell elements outputs. Reading the ASCII files are performed only once the LS-DYNA simulation has terminated. In order to shorten the run-time, the simulation is performed in multiple time-segments, where each time-segment is a fraction of the final run-time specified in LS-DYNA's *CONTROL TERMINATION card. The number of time-segments is determined by the value of the `termination factor` parameter. If, for example, the termination time specified in LS-DYNA's *CONTROL TERMINATION card is 15, and the value of the `termination factor` is 10, the LCZ algorithm will execute the first LS-DYNA simulation from time 0 to a time of 1.5 (15/10). The code will then search for the first thick-shell element to satisfy the element splitting criteria during this run. If no element satisfied this criteria, the simulation will be resumed from a time of 1.5 to a time of 3, and so on, until the final termination time of 15 is reached.

- `parts_to_skip` : Part numbers which are not composite parts and are not taking part during the splitting operation, such as rigid parts, parts made of solid elements, etc. These parts will be ignored by the LCZ algorithm during its execution. In this examples, these are part numbers 2, 3 and 4.

- `direc` : Type of element-splitting criterion. The following options are available:

5 - τ_{zx} values only, either negative or positive.

$$S = \sqrt{\left(\frac{\tau_{zx}}{\tau_{max}}\right)^2} \qquad (B.1)$$

6 - mixed-mode, taking into account either positive or negative values of τ_{zx} and σ_z.

$$S = \sqrt{\left(\frac{\sigma_z}{\sigma_{max}}\right)^2 + \left(\frac{\tau_{zx}}{\tau_{max}}\right)^2} \qquad \text{(B.2)}$$

7 - mixed-mode, taking into account either positive or negative values of τ_{zx}, and positive values of σ_z. Negative values of σ_z (compressive normal stress) are neglected.

$$S = \begin{cases} \sqrt{\left(\frac{\sigma_z}{\sigma_{max}}\right)^2 + \left(\frac{\tau_{zx}}{\tau_{max}}\right)^2}, & \text{if } \sigma_z \geq 0 \\ \sqrt{\left(\frac{\tau_{zx}}{\tau_{max}}\right)^2}, & \text{otherwise} \end{cases} \qquad \text{(B.3)}$$

- `sig_zz_max` : Maximum normal stress values (σ_{max}) used in the element splitting criterion, in this example, 80.

- `tau_zx_max` : Maximum shear stress values (τ_{max}) used in the element splitting criterion, in this example, 80.

- `threshhold_initial` : Critical value for the element splitting criteria, S_c. Once an LS-DYNA analysis is performed, the LCZ algorithm searches for the first thick-shell element to have a value of S which is equal or greater than S_c. In this example, this threshold is set equal to 0.4.

- `neighbour_trheshhold_scaling_factor` : A neighbour threshold value for the element splitting criteria. Once the first thick-shell element reaches S_c, the code will search for more thick shell elements which satisfy:

$$S \geq threshold \times S_c \qquad \text{(B.4)}$$

where *threshold* is the `neighbour_trheshhold_scaling_factor` defined above, having a value which is higher than 0 and lower than 1, in this example, 0.95.

- `initial_shock_time` : An option to allow the code to "ignore" critical element splitting criterion values which are satisfied earlier than the time specified using this parameter. In many loading scenarios using an explicit time integration scheme, the initial loading of the structure causes an unrealistic stress wave to travel through the structure, which will cause the element splitting criterion to be satisfied, leading to premature splitting of

thick-shell elements. Such an example could be during an initialization phase where the structure is subjected to a gravitational load. This parameter supplies a mean to overcome this limitation by ignoring element-splitting criterion values at early stages of the analysis. In this example, this parameter is set to 0.04, thus element splitting values satisfied from time 0 to 0.04 will be ignored.

- `shock_time` : Similar to the above option, this parameter supplies a mean to ignore critical element-splitting criterion values which are satisfied right after a restart or an element-splitting step. In this example, assuming that an element splitting step occurs at a time of 3, the algorithm will search for element satisfying the element splitting criteria at a time of 3+0.04. This option allows to mitigate the numerical noise introduced into the analysis following a restart.

- `global_damping_value` : A global damping value which will be used in the analysis, using LS-DYNA's `*DAMPING_GLOBAL` card. The `*DAMPING_GLOBAL` card will be automatically created by the code and does not need to be added to the LS-DYNA keyword used in the analysis. In this example, the global damping factor is set equal to 0.

- `contact_type` : Contact type to be created between the offset-shell elements generated using the element splitting process. Available options are: '

  single : A single AUTOMATIC_SINGLE_SURFACE contact algorithm between all shell parts generated during the splitting process will be created.

  single_sep : A separate AUTOMATIC_SINGLE_SURFACE contact algorithm between each pair of offset-shell element parts generated during the splitting process will be created.

  s2s : A separate AUTOMATIC_SURFACE_TO_SURFACE contact between each pair of offset-shell element parts generated during the splitting process will be created.

- `extra_parts_to_single_contact` : This parameter allows specifying more parts that will be added to the single surface contact, in case a single surface contact is used between the new shells. This is useful, for example, in case non-composite parts may interact with the offset-shells generated during the execution of the

LCZ algorithm, such as the rigid sphere in a plate impact loading scenario. In the above example, the sphere part number is `200`. Any number of parts can be listed as needed in a list format, such as ['`121`','`123`',"`300`',...] if no parts are to be specified, an empty set should be used ['].

- `fs` : Static coefficient of friction between the offset-shell elements generated by the LCZ algorithm generated during the run, in this example, `0.2`.

- `fd` : Dynamic coefficient of friction between the offset-shell elements generated by the LCZ algorithm during the run, in this example, `0.2`.

- `sfs` : Scale factor on the default LS-DYNA slave penalty stiffness, in this example, `1`. More information can be found under the *CONTACT keyword description in LS-DYNA's user's manual [18].

- `sfm` : Scale factor on the default LS-DYNA master penalty stiffness, in this example, `1`. More information can be found under the *CONTACT keyword description in LS-DYNA's user's manual [18].

- `dc` : Exponential decay coefficient used in the contact between the offset-shell elements generated by the LCZ algorithm during the run, in this example, `3.0`. More information can be found under the *CONTACT keyword description in LS-DYNA's user's manual [18].

- `vc` : Coefficient of viscous friction used in the contact between the offset-shell elements generated by the LCZ algorithm during the run, in this example, `0.0`. More information can be found under the *CONTACT keyword description in LS-DYNA's user's manual [18].

- `vdc` : Viscous damping coefficient in percent of critical, used in the contact between the offset-shell elements generated by the LCZ algorithm during the run, in this example, `0.0`. More information can be found under the *CONTACT keyword description in LS-DYNA's user's manual [18].

- `soft` : Soft constraint option used in the contact between the offset-shell elements generated by the LCZ algorithm during the run, in this example, `2`. More information can be found under the

*CONTACT keyword description in LS-DYNA's user's manual [18].

- `add_Ö£control_shell_card` : This parameter can be set to either true or false. Setting this parameter to "true", will cause the LCZ algorithm to add an LS-DYNA's *CONTROL_SHELL card to the main keyword file, with the CNTCO parameter within this card set to 1, thus making LS-DYNA consider the shell offset and thickness in the contact algorithms. It was found, however, that in some cases, this can cause bugs during the restarts performed by the code, and was thus left as an option for the user to either set it on or off.

- `mapping_flag` : This parameter allows performing the LCZ analysis without mapping, by setting its value to false. A value of true for this variable will cause the LCZ algorithm to perform the mapping process during the element splitting operation.

- `ply_list` : A list containing all thick-shell parts numbers to be split during the execution of the LCZ algorithm. The parts should be listed in their through thickness order. In this example, part 1 is followed by part 5, then part 6 and finally part 7.

- `cohesive_mat_deff` : A list of cohesive material definitions for the cohesive interfaces generated by the LCZ algorithm. By using a list structure for this parameter, different cohesive properties can be defined for each cohesive interface in the model. The number of cohesive materials defined should be equal to the number of parts in the `ply_list` parameter defined above. This list consists of several sub-lists, where each sub-list is a definition of a single cohesive material. In this example, the first material definition is given using the list ['MID=21','G1c=0.8','G2c=2','T_normal=80', 'S_shear=150','intfall=4'], the second cohesive material is defined using the list ['MID=22','G1c=0.8','G2c=2','T_normal=80', 'S_shear=150','intfall=4'], and so on. Each sub list contains the cohesive material number (`MID`), the critical energy release rate under mode-I loading condition (`G1c`), the critical energy release rate under mode-II loading condition (`G2c`), the maximum normal stress in the cohesive interface (`T_normal`), and the maximum shear stress in the cohesive interface (`T_shear`). The order of the material input should be equal to the order of thick-shell parts defined in the `ply_list` parameter above, such that the first cohesive material defined in the list will relate to

the interface of the first thick-shell part defined in the `ply_list` parameter, and so on. The cohesive material definitions should be enclosed in square brackets, and separated by commas, as in the following format: `cohesive_mat_deff=[[first_material]`, `[second_material],[third_material]`, ...].

- `split_location_list` : A list containing the relative through-thickness splitting location, for each thick-shell part defined in the `ply_list` parameter. In this example, each thick-shell part will be split in its mid-plane location, as the values are set to 0.5. Valid values should be grater than 0 and lower than 1.

- `ply_thickness_list`: A list containing the thickness of each thick-shell part defined in the `ply_list` parameter. In this example, each thick-shell part has a thickness of 1.1625.

3. General guidelines for setting the LCZ analysis:

  (a) It is advised to run the LS-DYNA keyword file for several time steps prior to the execution of the LCZ algorithm, in order to verify that the keyword is set up correctly and does not contain any errors.

  (b) The composite thick-shell parts should be defined using LS-DYNA's ***PART_COMPOSITE** card, and the number of through-thickness integration points in the ***PART_COMPOSITE** keyword describing the composite thick-shell parts should be sufficient to allow correct splitting using the LCZ algorithm, and should be equal in all composite components taking part in the analysis.

  (c) All nodes and thick-shell elements defined within the initial LS-DYNA keyword file have to be numbered such that the lowest ID of the first node and thick-shell element will be 1. The numbering of the nodes and thick-shell elements should be continuous in an increasing order, and should not contain any number-jumps.

  (d) Composite part should e defined prior to the non-composite and rigid parts in the LS-DYNA keyword file.

  (e) No thick-shell history output should be requested in the LS-DYNA keyword file, as this will cause errors during the execution of the LCZ algorithm. The required history database files will be automatically created by the code during the run.

  (f) In order to allow a correct mapping process, an LS-DYNA

Computer Program B.1 Typical content of a `parameters.txt` file, used to control the execution of the LCZ algorithm.

---

runfile=1_plate_impact_4_layers.k
instant_split=false
interface_springback_NSHV=5
radial_split_distance=8
exe=/home/lsdyna/executables/./lsdyna_smp_971
termination_factor=24
parts_to_skip=2,3,4
direc=7
sig_zz_max=80
sig_zx_max=150
threshhold_initial=0.4
neighbour_trheshhold_scaling_factor=0.95
initial_shock_time=0.04
shock_time=0.125
global_damping_value=0
contact_type=single_sep
extra_parts_to_single_contact=['']
fs=0.2
fd=0.2
sfs=1
sfm=1
dc=3.0
vc=3.0
vdc=80
soft=2
add_control_shell_card=true
mapping_flag=true
ply_list=[['1'],['5'],['6'],['7']]
cohesive_mat_deff=[['MID=21','G1c=0.8','G2c=2',
'T_normal=80','S_shear=150','intfall=4'],

['MID=22','G1c=0.8','G2c=2','T_normal=80','S_shear=150','intfall=4'],

['MID=23','G1c=0.8','G2c=2','T_normal=80','S_shear=150','intfall=4'],

['MID=24','G1c=0.8','G2c=2','T_normal=80','S_shear=150','intfall=4']]
split_location_list=['0.5','0.5','0.5','0.5']
ply_thickness_list=['1.1625','1.1625','1.1625','1.1625']

---

*DATABASE_EXTENT_BINARY card should be specified within the original LS-DYNA keyword, with the INTOUT parameter set to ALL. This will cause LS-DYNA to write both stress and strain data into the the eloutdet file, which is necessary for the mapping process to be performed correctly.

Ö£

(g) An LS-DYNA *SECTION_TSHELL card is to be defined in the original keyword, even if only *PART_COMPOSITE_TSHELL cards are used and no *SECTION_TSHELL card is required for the analysis. The card does not need to be referred by any of the other parts in the model.

4. Performing the numerical simulation using the LCZ algorithm

Once the parameters.txt file was modified and placed in the **dist** running directory next to the LS-DYNA keyword and LCZ executable, the following command should be executed in order to initialize the LCZ analysis:

» `python LCZ_executable.py`

Once initialized, the LCZ algorithm will read the **parameters** text file, and a log file (**logfile.txt**) will be created, in which important operations performed by the code will be documented during the execution of the LCZ code. A subdirectory titled Ö£o will be created, in which the first LS-DYNA simulation will be performed. The subsequent LS-DYNA simulations will be performed in adjacent directories numbered increasingly, as can be seen in Figure B.2.

In addition to executing the LCZ algorithm locally on a Linux shell, the job can be batch processed across a high performance computing cluster, by submitting the job to the queuing system. A typical procedure to batch process the LCZ analysis would be to create a script which will be submitted to the queuing system. In this exmaple, the script name would be **1_dynascr**, and its content is brought in Program B.2.

In order to send the job to be executed across the cluset, one should change to the working directory using the command:

» `cd PATH_TO_WORKING_DIRECTORY`

and then send the job to the queuing system using the following command:

Computer Program B.2 Content of the `1_dynascr` text file used to batch-process the LCZ execution.

```
#!/bin/sh
#PBS -N my_run_name
#PBS -l select=1:ncpus=12

cd PATH_TO_WORKING_DIRECTORY/dist
./LCZ_executable.py
```

```
» qsub 1_dynascr
```

5. Reading the results following the execution of the LCZ algorithm

   Each subdirectory created by the LCZ algorithm (shown in Figure B.2), contains the LS-DYNA result files from the simulation performed within this directory. These results include the binary three dimensional result files (`d3plot`), as well as results in ASCII format, such as LS-DYNA's `rcforc` and `nodout` files, which contain time histories of the contact forces and nodal information requested during the run. It is important to note that these files will be created only if this was specifically requested during the LS-DYNA simulation by the user, using the appropriate commands in the original LS-DYNA keyword file.

   Generating continuous time history plots, such as the ones presented in these thesis, from the results obtained following the execution of the LCZ algorithm, is a tedious task, as it requires manually "stitching" all of the results from all running directories under the main running directory. This task can be much simplified using automated scripts, which are able to find the required results in each working directory and stitch all of the results together, generating meaningful and continuous plots. Such scripts are problem dependent and are thus not presented here, but were used to generate the various plots presented in this theses.
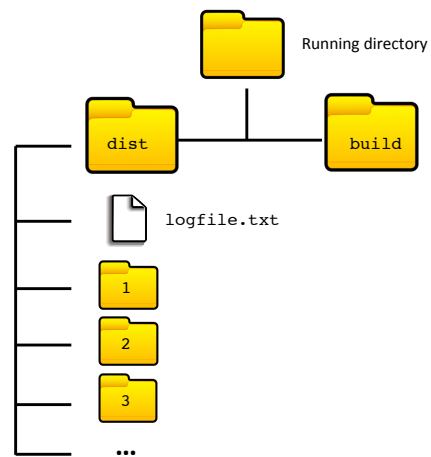
Figure B.2: Schematic directory architecture following execution of the LCZ algorithm.

Appendix C

General Description of Composite Tube Crushing Process

The composite tubes analyzed in Chapter 5.2 intended to be used as energy absorbing structures, more specifically, to help reduce the deceleration loads transmitted to the passengers during a car accident, and thus lower the risk or severity of an injury.

Initial design of these energy-absorbing members consisted of metallic tubes of either a circular or a rectangular cross sections, which were undergoing plastic deformation and progressive plastic folding during an impact event [127]. In recent years, however, environmental regulations are forcing car manufacturers to design cars with improved fuel efficiency, constructed of lighter materials. Composites pose a great potential as a constructive material due to their excellent specific strength properties. Thus, an effort is made to design energy absorbing components using light-weight composite materials.

While there is a considerable amount of published data on the response of metallic tubes to dynamic, axial crushing, and the response can be predicted with reasonable accuracy, predicting the crushing response of composite tubes is far more difficult, for a number of reasons. Most composites are made from brittle fibres embedded in a polymer matrix, which may be brittle or ductile depending on the choice of polymer. This means that extensive plastic deformation cannot occur, and collapse by progressive plastic folding of the type observed in metal and plastic tubes is impossible. In addition, the properties of composite materials are strongly dependent on the fibre arrangement, the fibre volume fraction and the properties of the fibre-matrix interface. Thus, simulating the behavior of these structures requires the ability to correctly describe the damage growth mechanisms in the composite material, which is driven by the microstructure of the material.

The global response of composite-tubes undergoing dynamic crushing

can be categorized as belonging to one of three categories: Stable progressive folding (Fig C.1.a), Stable progressive crushing (Fig C.1.b), or an unstable folding / crushing (Fig C.1.c). The stable progressive folding mode, resembles the progressive folding mode observed in ductile metal and plastic tubes, and occurs mainly in crushing of thin walled tubes made of relatively ductile composite materials, and is less common in tubes made of brittle fibers or having a thicker wall thickness ([125] , [31]). Stable, progressive crushing mode, involves the formation of a zone of micro-fracture at one end of the tube which then propagates along the tube at the same speed as the crushing front.

In most engineering applications, stable behavior is desired, as this leads to smoother deceleration profiles, as well as relatively confined crushed geometry. The stability of the crushing process is governed by the tube's geometrical dimensions, as well as ply layup, the loading symmetry, and the type of boundary conditions which are present at the end of the tube. In order to ensure a stable crushing process, it is usually desired for the crushing to be initialized at a specific location rather than at a random location along the tube. This location is most often chosen to be at the tube end, and in this case fracture initialization can be achieved by chamfering the tube end, thus weakening and reducing the cross-section, or by using external surfaces that initiates fracture and allow the tube material to flow in a stable manner [58],[32].

(a)   (b)   (c)
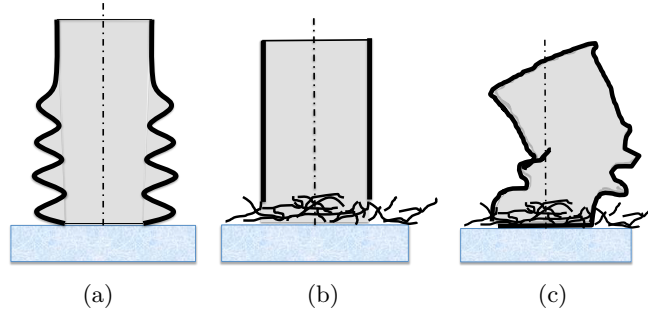
Figure C.1: Schematic crushing morphologies obtained during a composite tube-crushing event, with an initial tube axis of symmetry shown in a dashed line. **a).** Progressive folding **b).** Progressive crushing. (c) Unstable folding and crushing.

A schematic load vs. displacement of a stable crushing process is shown in Figure C.2. Here, the crushing load P is shown as a function of the

tube-end displacement, S. The load profile can be characterized by three distinct regions: I - the initial loading state, II - progressive stable crushing state, and III - post progressive crushing state. As the tube is loaded, the loading force increases until crushing of the tube is initialized, which results in a sharp load drop. The maximum load, just before the initialization of the crushing process, is denoted by P_{max}. This load is usually limited by the maximum compressive strength of the composite reinforcing material. Following the load-drop, is a plateau of an oscillating, but stable, force profile, with an average load value $\bar{P}$. The region of stable crushing is denoted by II. S_I denotes the displacement at which the stable crushing process begins. As the displacement increases, more energy is absorbed by the tube, until one of two conditions are met - if the load is removed before reaching the tube's possible maximum crushing displacement, the load will eventually drop to zero, with a final displacement S_B. On the other hand, if loading continues to be applied, at some displacement S_B the tube will reach a solid state which will result in a sudden increase of the loading force. If the tube is to be used as an energy absorber, it is usually preferable to design the tube such that this region (denoted by III) will be outside the performance envelope of the tube, as reaching this state will lead to large deceleration values. S_B is therefore considered to be the maximum displacement of the tube, that is still within the stable crushing phase, wether the stable crushing phase was terminated due to the reduction of the load, or reaching a solid-state of the tube.
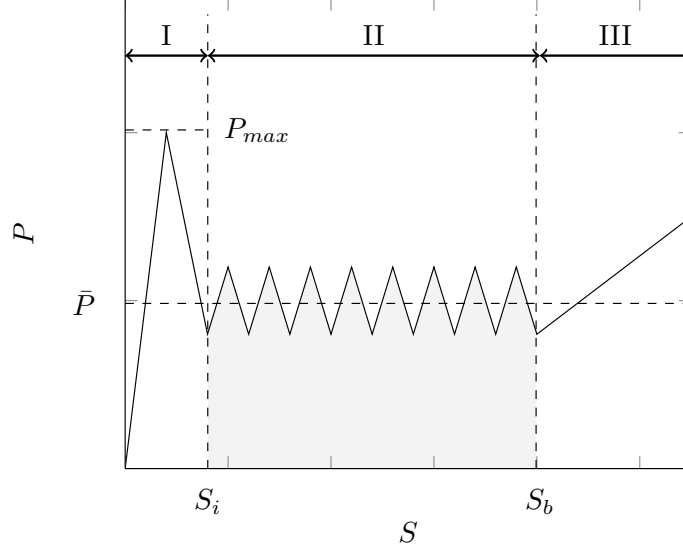
Figure C.2: A schematic load vs. displacement profile obtained during a stable composite tube crushing process. The crushing load P is shown as a function of the tube-end displacement, S. Three distinct regions are visible: I - the initial loading state, II - progressive stable crushing phase, and III - post progressive crushing phase. P_{max} is the maximum load, $\bar{P}$ denotes the average load value during the stable crushing state, and S_i denotes the displacement at which the stable behavior begins. At displacement S_b, the tube reaches a solid state which will result in a sudden increase of the loading force.

The global response of the tube is influenced by failure mechanisms which evolve at tube's tip within the ply level, and have a direct effect on the global failure topology. Hull [58] and Farley [32] studied the failure morphologies of composite-tube walls undergoing progressive, axial crushing. They categorized the ply-level failure modes as to be belonging to one of the following three groups: Transverse Shear (Figure C.3.**a**), which involves transverse matrix-crack growth and extensive failure of the plies with fibers in the transverse directions, lamina bending, or splaying (Figure C.3.**b**) or ply buckling (Figure C.3.**c**). In most crushing scenarios, however, multiple failure modes are present, as can be seen in Figure C.4. Here, a schematic cross-section of

a tube with a $[0°/90°/\bar{0}°]_s$ ply layup undergoes progressive crushing. Transverse shearing cracks develop in the 90° plies, where delamination develops between the 0° and 90° plies as bending and splaying develop at the 0° plies. In some cases, a debris wedge, a wedge-shaped volume of confined, crushed material is formed between the tube and the crushing surface. Simulating the behavior of composite tubes undergoing crushing requires the ability to correctly describe the various damage growth mechanisms and their interaction.

(a)   (b)   (c)
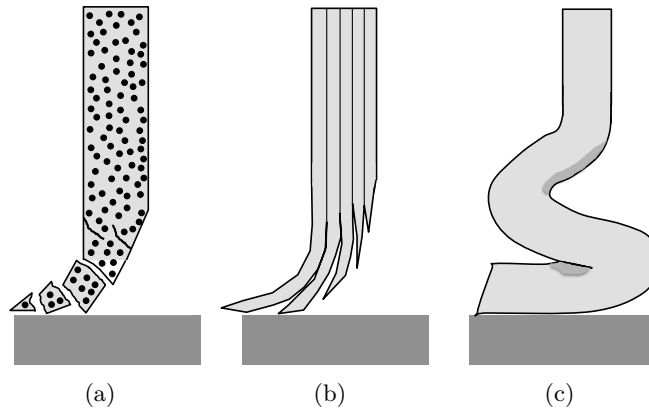
Figure C.3: Failure morphologies of composite-tube walls undergoing progressive, axial crushing. **a).** Transverse Shear , **b).** Lamina bending, or splaying, **c).** Ply buckling
.
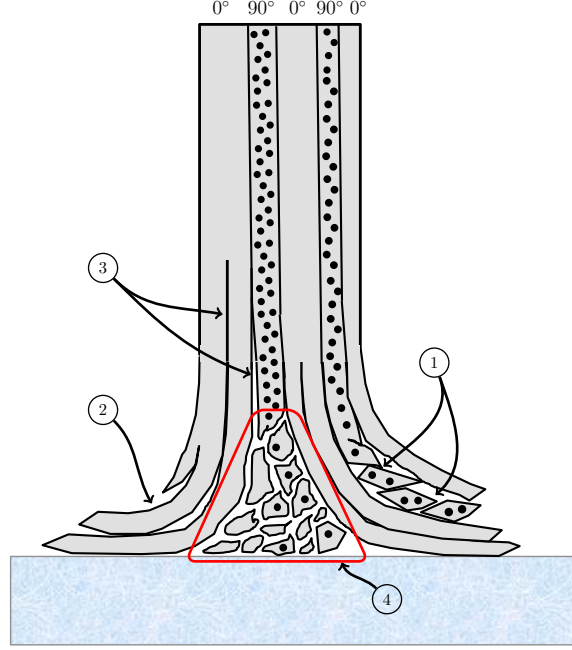
Figure C.4: Typical failure morphology obtained in a composite tube during a dynamic crushing process, shown here for a $[0°/90°/\bar{0}°]_s$ ply layup. A cross section through the wall of the tube demonstrates the following failure modes: **1).** Transverse Shear in the 90° plies. **2).** Lamina bending in the 0° plies. **3).** Splitting within the 0° ply and delamination between the 0° and the 90° plies. **4).** Debris Wedge, consisting of crushed fibres and resin, which is formed at the between the tube and the impacted plane.

Work and Specific Energy during a tube-crushing process

The work performed during the crushing process (neglecting the post progressive crushing phase) is [85]:

$$W_f = \int_0^{S_b} P dS \tag{C.1}$$

Where P is the crushing load, S is the crushing displacement, and S_b is the displacement at which the tube reaches a solid state.

The specific energy absorption, SEA, is defined as the energy absorbed or work done in forming a unit mass of crushed material [85]:

$$SEA = \frac{\text{energy absorbed}}{\text{mass of damaged material}} = \frac{W_f}{AS_b\rho} \qquad \text{(C.2)}$$

where A is the cross-sectional area of the tube, and ρ is the tube's density.

Appendix D

LS-DYNA Material Cards

This appendix brings the LS-DYNA material cards used during the validation process described in Chapter 5.

Computer Program D.1 LS-DYNA MAT_54 card used in the double-notched $[90/0]_s$ test coupon (Chapter 5.1), for the 0° ply

```
*MAT_ENHANCED_COMPOSITE_DAMAGE
$#    mid       ro       ea       eb      (ec)     prba    (prca)    (prcb)
       6 1.9700E-3 43900.000 15400.000 15400.000  0.105239  0.105239  0.300000
$#    gab      gbc      gca      (kf)     aopt
 4340.0000 4340.0000 4340.0000    0.000       -3
$#     xp       yp       zp       a1       a2       a3    mangle
   0.000    0.000    0.000    0.000    0.000    0.000    0.000
$#     v1       v2       v3       d1       d2       d3    dfailm    dfails
   0.000    0.000    0.000    0.000    0.000    0.000     0.14     0.50
$#   tfail     alph     soft     fbrt    ycfac   dfailt   dfailc      efs
   0.000    0.000 1.000000    0.000 2.000000    0.100    -1E24     0.50
$#     xc       xt       yc       yt       sc     crit     beta
  620.0000 1140.0000 128.00000  39.00000 80.000000 54.000000    0.000
$#    pel     epsf     epsr     tsmd    soft2
   0.000     1E24     2E24    0.000 1.000000
$#  slimt1   slimc1   slimt2   slimc2    slims   ncyred    softg
   0.000    0.000    0.000    0.000    0.000    0.000 1.000000
```

Computer Program D.2 Material definitions used in the double-notch $[90/0]_s$ for the 90° ply

```
*MAT_ENHANCED_COMPOSITE_DAMAGE
$#     mid        ro        ea        eb      (ec)      prba    (prca)    (prcb)
       69  1.9700E-3 43900.000 7700.0000 7700.0000 5.2620E-2 5.2620E-2  0.300000
$#     gab       gbc       gca      (kf)      aopt
 4340.0000 4340.0000 4340.0000     0.000       -33
$#      xp        yp        zp        a1        a2        a3    mangle
     0.000     0.000     0.000     0.000     0.000     0.000     0.000
$#      v1        v2        v3        d1        d2        d3    dfailm    dfails
     0.000     0.000     0.000     0.000     0.000     0.000      0.14      0.50
$#    tfail      alph      soft      fbrt     ycfac    dfailt    dfailc       efs
     0.000     0.000  1.000000     0.000  2.000000     0.100     -1E24      0.50
$#      xc        xt        yc        yt        sc      crit      beta
 620.00000 1140.0000 128.00000 39.000000    80.000 54.000000    0.0000
$#     pel      epsf      epsr      tsmd     soft2
     0.000      1E24      2E24     0.000  1.000000
$#  slimt1    slimc1    slimt2    slimc2     slims    ncyred     softg
     0.000     0.000     0.000     0.000     0.000     0.000  1.000000
```

Computer Program D.3 Material definitions (CODAM1) used in the tube crush analysis (Defined using an LS-DYNA user-defined material card

```
*MAT_USER_DEFINED_MATERIAL_MODELS
$    MID      RO      MT      LMC     NHV    IORTHO    IBULK      IG
      2    1.3E-3     45      32      32       1        29        30
$   IVECT    IFAIL
      1        1
$   AOPT     MAXC     XP      YP      ZP      A1       A2       A3
     3.0
$    V1       V2      V3      D1      D2      D3      BETA
     0.0      0.0     1.0                            90
$    EX      VXY     GXY    NOZCF   SRFLAG   E1TMAX   E2TMAX   E3TMAX
  60000.0    0.0    9000.0    1
$    EY      VYZ     GYZ    EWSF            E1CMAX   E2CMAX   E3CMAX
  12500.0    0.0    9000.0
$    EZ      VXZ     GZX    EWSN            E4CMAX   E5CMAX   E6CMAX
   8000.0    0.0    9000.0
$  ERODE    EPSMAX    DAMT   BSFLAG   BMOD    GMOD    DAMDT    DEBUG
    2.0      2.0              1     20000.0  30000.0
```

Computer Program D.4 Strain-softening parameters used in the tube crush analysis (This is the first part of the ssparam.dat file, which is called by the CODAM1 material model

```
c Strain Softening Parameters
c
c X Parameters
c
c F-w-RE  t
    3
 0.000 0.000 1.000
 0.015 0.000 1.000
 0.030 1.000 0.000
c F-w-RE c x normal
    4
 0.000 0.000 1.000
 0.005 0.000 1.000
 0.008 0.500 0.001
 0.750 1.000 0.000
c Y Parameters Normal
c
c F-w-RE  t
    3
 0.000 0.000 1.000
 0.009 0.000 1.000
 0.020 1.000 0.000
c F-w-RE c
    3
 0.000 0.000 1.000
 0.020 0.000 1.000
 0.040 1.000 0.000
```

Computer Program D.5 Strain-softening parameters used in the tube crush analysis (This is the first part of the ssparam.dat file, which is called by the CODAM1 material model

```
c Z Parameters
c
c F-w-RE  t
    3
 0.000 0.000 1.000
 0.009 0.000 1.000
 0.020 1.000 0.000

c F-w-RE c
    3
 0.000 0.000 1.000
 0.500 0.000 1.000
 1.000 1.000 0.000
c XY Parameters
c
c w-RE
    3
 0.000 1.000
 0.500 0.500
 1.000 0.000
c YZ Parameters
c
c w-RE
    3
 0.000 1.000
 0.500 0.500
 1.000 0.000

c ZX Parameters
c
c w-RE
    3
 0.000 1.000
 0.500 0.500
 1.000 0.000
```

Computer Program D.6 Strain-softening parameters used in the tube crush analysis (This is the first part of the ssparam.dat file, which is called by the CODAM1 material model

```
c
c Plateau
c sigx  fxci  fxcs
 -250. 0.005 0.008
c sigy  fyci  fycs
   0.0
c sigz  fzci fzcs
   0.0
c
c damage potential function constants
c    kxt      kxc      lxt      lxc      mxt      mxc
 1.000E+00 1.000E+00 1.000E+10 1.000E+10 1.000E+10 1.000E+10
c    kyt      kyc      lyt      lyc      myt      myc
 1.000E+10 1.000E+10 1.000E+00 1.000E+00 1.000E+10 1.000E+10
c    kzt      kzc      lzt      lzc      mzt      mzc
 1.000E+10 1.000E+10 1.000E+10 1.000E+10 1.000E+00 1.000E+00
c    fxs      fxt      fxu
 1.000E+10 1.000E+10 1.000E+10
c    fys      fyt      fyu
 1.000E+10 1.000E+10 1.000E+10
c    fzs      fzt      fzu
 1.000E+10 1.000E+10 1.000E+10
c
c bazant scaling factors
c    KXT      KXC      KYT      KYC      KZT      KZC
    10.50     1.00    25.00    10.00    25.00     1.00
```

Computer Program D.7 CODAM2 card used in tube-crush analysis

```
*MAT_CODAM2_TITLE
MAT219
$#    mid       ro       ea       eb        -      prba        -      prcb
      2 1.3000E-3 60000.000 12500.000 8000.0000  0.062499  0.062499  0.062499
$#    gab        -        -    nlayer       r1       r2     nfreq
 9000.0000 9000.0000 9000.0000        1    0.000    0.000         0
$#    xp       yp       zp       a1       a2       a3     aopt
   0.000    0.000    0.000    0.000    0.000    0.000 3.000000
$#    v1       v2       v3       d1       d2       d3     beta     macf
   0.000    0.000 1.000000    0.000    0.000    0.000 90.000000        1
$# angle1   angle2   angle3   angle4   angle5   angle6   angle7   angle8
   0.000    0.000    0.000    0.000    0.000    0.000    0.000    0.000
$#  imatt    ifibt    iloct    idelt    smatt    sfibt    sloct    sdelt
 9.0000E-3 1.5000E-2 1.000000 1.000000 0.347000 0.224000    0.000    0.000
$#  imatc    ifibc    ilocc    idelc    smatc    sfibc    slocc    sdelc
 2.0000E-2 5.0000E-3 1.000000 1.000000 0.285000 1.290000    0.000    0.000
$#  erode   erpar1   erpar2   resids
      2    0.000 1.000000    0.000
```

Computer Program D.8 Cohesive material card used in tube-crush analysis

```
*MAT_COHESIVE_GENERAL
$#    mid      ro    roflg   intfall      tes     tslc      gic     giic
21,1.34e-6,0,2,0.000,8713,1.75,1.75
$#    xmu       t        s     stfsf
1.000000,50,50,0.000
```

Appendix E

Brief Description of the CODAM2 Material Model

CODAM2, which is the second generation of the composite damage material models developed at the UBC Composites Group, and is described in detail in Forghani [35]. CODAM2 is a sub-laminate based model, that is designed to simulate the behavior of laminated composites at the macro (structural) scale.

Using the CODAM2 material formulation, the in-plane stiffness matrix of the damaged laminate, A_d, is written as the summation of the effective contributions of the layers in the laminate as shown in Equation E.1 [35]:

$$\mathbf{A}_d = \sum_{k=1}^{n} \mathbf{T}_k^T \mathbf{Q}_k^d \mathbf{T}_k t_k \tag{E.1}$$

where $\mathbf{T}_k$ is the transformation matrix for the strain vector of the kth layer, t_k is the thickness of the kth layer, n is the number of layers in the sub-laminate, and $\mathbf{Q}_k^d$ is the in-plane stiffness matrix of the kth layer in the principal orthotropic plane, which is written as:

$$\mathbf{Q}_k^d = \begin{bmatrix} \frac{R_f E_1}{1-R_f R_m \nu_{12}\nu_{21}} & \frac{R_f R_m \nu_{12} E_2}{1-R_f R_m \nu_{12}\nu_{21}} & 0 \\ & \frac{R_f E_2}{1-R_f R_m \nu_{12}\nu_{21}} & 0 \\ SYM & & R_m G_{12} \end{bmatrix} \tag{E.2}$$

where E_1 is the Young's modulus in the fiber direction, E_2 is the Young's modulus in the matrix direction, R_f and R_m are two reduction coefficients, that represent the reduction of stiffness in the longitudinal (fibre) and transverse (matrix) directions, respectively. The reduction coefficients are equal to 1 in the undamaged condition, and gradually decrease to 0 for a saturated damage condition. Thus, for a fully damaged material (i.e $R_f = R_m = 0$,

for all n material layers), all members of the in-plane stiffness matrix are set to 0.

The stiffness reduction parameters (R_f and R_m) are defined as linear functions of damage parameter ω, as shown in Figure E.1.**a**, which by itself is assumed to grow as a hyperbolic function of the equivalent averaged (non-local) strains, $\bar{\varepsilon}^{eq}$ (Figure E.1.**b**), and Equation E.3:

$$\omega_\alpha = \frac{(|\bar{\varepsilon}_\alpha^{eq}|) - \varepsilon_\alpha^i}{(\varepsilon_\alpha^s - \varepsilon_\alpha^i)} \frac{\varepsilon_\alpha^s}{|\bar{\varepsilon}_\alpha^{eq}|} \quad ; \ \text{for} \ \left(|\bar{\varepsilon}_\alpha^{eq}| - \varepsilon_\alpha^i\right) > 0 \tag{E.3}$$

where superscripts i and s denote the damage initiation and saturation values, respectively. The initiation and saturation parameters are defined in material cards #6 and #7 of the LS-DYNA *MAT_CODAM2 material input. Damage is considered to be monotonically increasing as a function of time.

The averaged, non-local strains ($\bar{\varepsilon}_\alpha^{eq}$) are evaluated using the following geometrical averaging equation [35]:

$$\bar{\varepsilon}_\alpha^{eq} = \int_{\Omega_x} \varepsilon_\alpha^{eq}(x) w_\alpha (X - x) d\Omega \tag{E.4}$$

where α denotes damage for fiber ($\alpha = f$) or matrix ($\alpha = m$), within the kth layer of the sub-laminate. X represents the position vector of the original point of interest, and x denotes the position vector of all other points (Gauss points) in a spherical averaging zone denoted by Ω. The radius of the spherical averaging zone Ω is defined as r_d, and is linked directly to the predicted size of the damage-zone in the material. r_d is defined using a user-defined variable R1 in the LS-DYNA material card. w_a is a bell-shaped weight function, which is evaluated by:

$$w_a = \left[1 - \left(\frac{d}{r_d}\right)^2\right]^2 \tag{E.5}$$

where d is the distance from the integration point of interest to another integration point within the averaging zone.

The initiation and saturation strains, which appear in Equation E.3 and govern the behavior of ω, are defined by the user for both the longitudinal (fibre) and transverse (matrix) directions, and are used to control the strains at which damage initiates and saturates at the material.

For further details regarding the CODAM2 material model formulation, the reader is referred to [35].
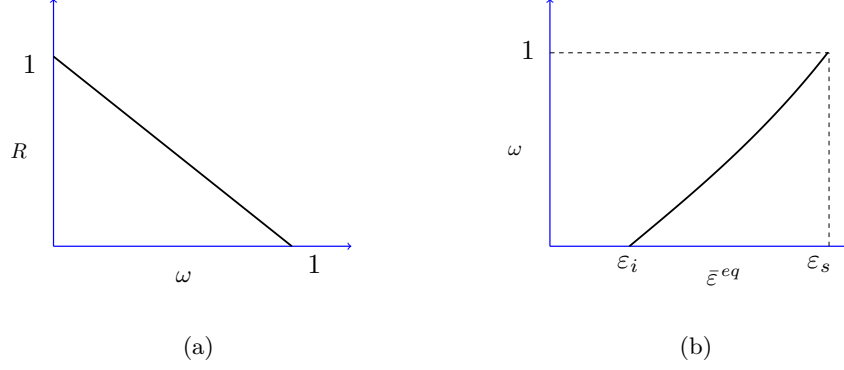
(a)

(b)

Figure E.1: **a).** Stiffness reduction coefficients R , as a function of the damage parameter ω. R is equal to 1 in an undamaged material, and 0 in a fully damaged material. **b).** Value of damage parameter ω as a function of the averaged (non-local) equivalent strain, $\bar{\varepsilon}^{eq}$. ε_i and ε_s are the averaged (non-local) damage initiation and saturations strains, respectively, defined by the user for both the longitudinal (fibre) and transverse (matrix) directions, using the LS-DYNA CODAM2 material card.

Appendix F

Calibrating the CODAM2 Material Model for the Tube-Crushing Simulation

The CODAM2 parameters required to identify the in-plane orthotropic response of the braided material were calibrated based on previous numerical work performed by McGregor et al. [84], where the first generation of the Composite Damage Models (CODAM1) developed at the University of British Columbia, was successfully applied to the tube-crushing problem studied here, and thus served as a datum baseline for the calibration process described bellow.

A single element model, which is schematically shown in Figure F.1, served for the purpose of the calibration process. Here, a single LS-DYNA shell element (*ELEMENT_SHELL, ELFORM=16) was loaded in the positive y direction. All x translational degrees of freedom were constrained, and the degrees of freedom of the unloaded nodes were constrained in the global y direction as well. The model was first simulated using the original CODAM1 material card used by McGregor et al. [84]. In this case, the material axial direction was defined to be along the global y direction, thus resembling a pure tensile test along the fiber direction, with 0 strain in the matrix (transverse) direction. The strain energy per unit volume of material prior to complete fracture, γ, was then calculated using:

$$\gamma = \int_0^{\varepsilon_f} \sigma d\varepsilon \tag{F.1}$$

where ε_f is the strain to complete fracture, and σ is the stress in the element in the loading (global y) direction.

The fracture energy of the material, G_f, for the loading direction tested, was then obtained using:
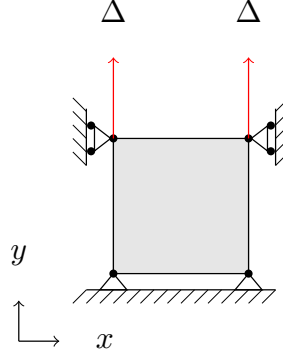
$$G_f = \gamma \times h_e \tag{F.2}$$

Figure F.1: A simple single-element model used for the CODAM2 calibration process. LS-DYNA shell element is used (*ELEMENT_SHELL, ELFORM=16). All x translational degrees of freedom were constrained, and the degrees of freedom of the unloaded nodes were constrained in the global y direction as well. Prescribed displacement is applied for the top nodes (Δ) in the global y direction.

where h_e is the element size used in the analysis (2.5 mm).

Once G_f was obtained, the simulation was repeated using CODAM2 as the in-plane damage model. The value of the initiation and saturation strains, which are required as a user input for the CODAM2 material model, were obtained as follows: The *initiation* strain was set equal to the value of the *initiation* strain used in the CODAM1 material model. The value of the damage *saturation* strain in CODAM2 was then adjusted, until the fracture energy obtained from the analysis using Equation F.1 and Equation F.2, was close to the value of the fracture energy obtained when the simulation was performed using CODAM1. The resulting stress vs. strain plot obtained from the calibration process, is brought in Figure F.2. Once loading initiates, there is a linear dependency between the stress and strain for both models, up to the point of damage initiation. Once damage initiates, while CODAM1 material model exhibits a parabolic reduction of stress until complete failure

of the material, CODAM2 exhibits a linear softening behavior. The resulting fracture energy obtained following the calibration process, is 253.12 kJ/m² and 253.47 kJ/m² for CODAM1 and CODAM2, respectively.

The same calibration process was now repeated for the following loading scenarios: compression in the fiber direction (Figure F.3), tension in the transverse direction (Figure F.4), and compression in the transverse direction (Figure F.5). The prescribed displacement was applied in the positive y direction in case of tensile loading, and along the negative y direction in case of compression, and the material direction was adjusted in accordance of the material direction tested.

Following the calibration process, the calibrated material card was then used in tandem with the LCZ method to simulate the tube-crushing experiment. The CODAM2 material parameters obtained from the calibration process, are listed in Table 5.5.
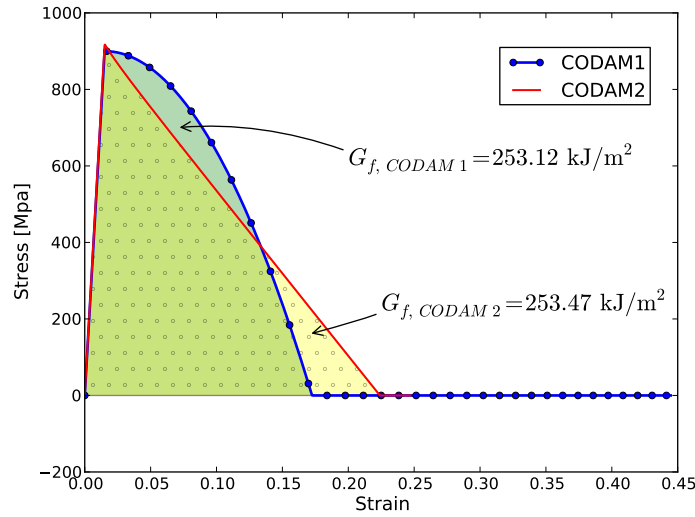

Figure F.2: Stress vs. strain plot obtained from a single shell-element simulation, under axial tensile loading, using the CODAM1 and CODAM2 material models. The fibres are aligned in the global y direction. The fracture energies obtained are 253.12 kJ/m² and 253.47 kJ/m², for CODAM1 and CODAM2, respectively.
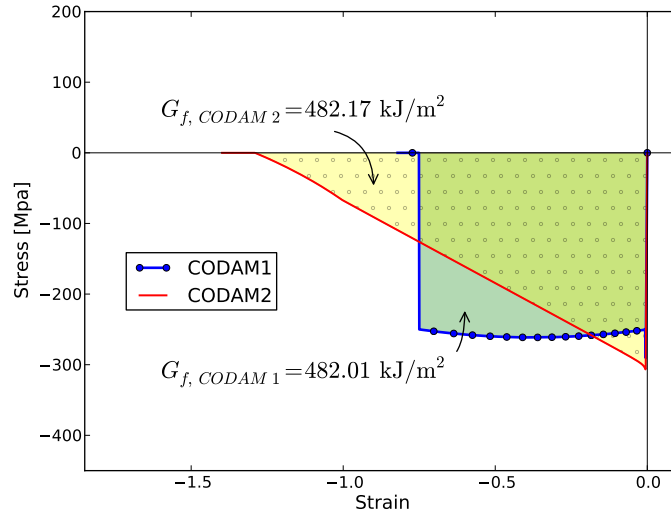
Figure F.3: Stress vs. strain plot obtained from s a single shell-element simulation, under axial compressive loading, using the CODAM1 and CODAM2 material models. The fibres are aligned in the global y direction. The fracture energies obtained are 482.01 kJ/m² and 482.17 kJ/m², for CODAM1 and CODAM2, respectively.
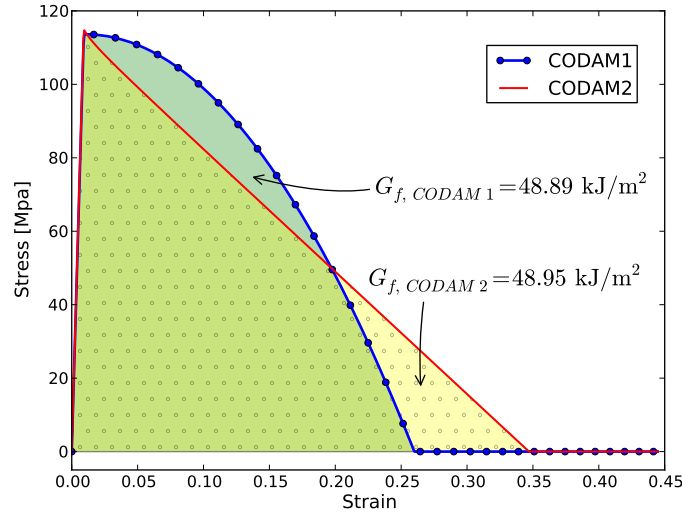
Figure F.4: Stress vs. strain plot obtained from a single shell-element under tensile loading in the transverse material direction, using the CODAM1 and CODAM2 material models. The main axis of the material is parallel to the global x direction. The fracture energies obtained are 48.89 kJ/m² and 48.95 kJ/m², for CODAM1 and CODAM2, respectively.
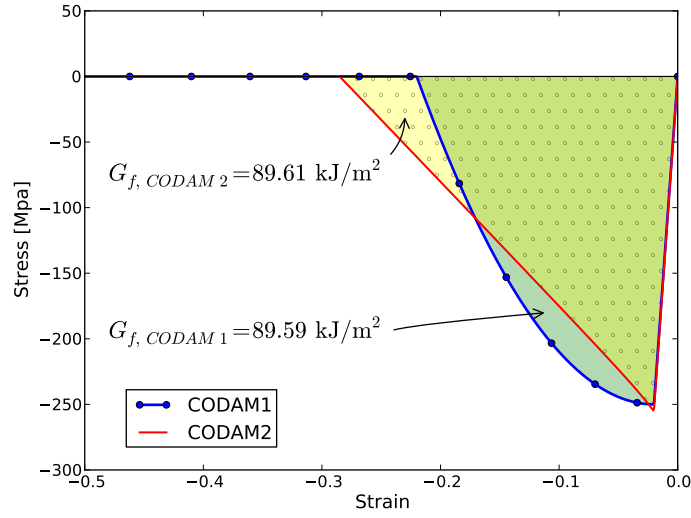
Figure F.5: Stress vs. strain plot obtained from a single shell-element under compressive loading in the transverse material direction, using the CODAM1 and CODAM2 material models. The main axis of the material is parallel to the global x direction. The fracture energies obtained are 89.59 kJ/m² and 89.61 kJ/m², for CODAM1 and CODAM2, respectively.